Quantum Optics at its best:

from quantum interferometry to quantum metrology

Jessica Oliveira de Almeida

Quantum Optics at its best: from quantum interferometry to quantum metrology

PhD Thesis

A Dissertation Submitted to the Institute of Photonic Sciences (ICFO), Spain
in Partial Fulfillment of the Requirements
for the Degree of Doctor of Philosophy
Universitat Politécnica de Catalunya (UPC)

by

Jessica Oliveira de Almeida

This thesis has been supervised by:

Prof. Dr. Maciej Lewenstein
and
Dr. Michail Skoteiniotis

To mamy and shanti

Abstract

Quantum optics experiments are currently the most advanced techniques to understand, verify and simulate quantum phenomena. However, to access all the performance available in quantum states of light, one needs to address fundamental operational limits. In quantum mechanics, the measurement strategy affects the quantum state; therefore, to access all the degrees of freedom available in the quantum states, one must implement the optimal feasible measurement. In this thesis, I investigate how to perform more precise measurements in optics, namely slit-interference and image resolution, by exploiting the quantum mechanical nature of light.

A complete description of multi-slit interference must include nonclassical paths, Feynman paths that goes through two or more slits. Prior work with atomic interference in the double-slit experiment with cavities as which-way detectors, has shown these paths to be experimentally inaccessible. In this thesis I show how such a setup can detect nonclassical paths with 1% probability, if different nonclassical paths are included. I also show how this setup can be used to erase and restore the coherence of the nonclassical paths. In the same chapter I demonstrate how the same setup could implement an exact measure of Born-rule violation. And in the last part I debate about the figures of merit in the literature to test the Born-rule.

During more than one century, there was a fundamental limit on image resolution; due to diffraction effects in finite detectors apertures, one cannot resolve two incoherent sources very close to each other, e.g. stars. In the last decade, the formalism of quantum information allowed new proposals for sub-diffraction limited resolution or super-resolving measurements. Nevertheless, these measurements are susceptible to misalignment. In this thesis, I suggest alternative measurement strategies to incorporate misalignment in super-resolution imaging, showing that sub-diffraction limited resolution is still possible. The proposed measurements can be implemented using linear optical transformations and offer an advantage in the case of estimation and discrimination of two incoherent point sources allowing one to quantify the mitigating effects of misalignment. Moreover, I propose a collective measurement strategy, on two or more photons, that estimates the separation between two incoherent point sources and is oblivious to misalignment.

In an optics experiment, the quantum state verification relies on tomography measurements on copies of the prepared state. The error in tomography experiments is called confidence region, and it defines the region in which the quantum state is found with the desired probability. There are different methods to compute confidence regions; in this thesis, I analyze the capability of the known methods by resolving two nearby quantum states using a finite amount of measurement data.

Contents

List of Figures

Chapter 1

Introduction

The rapid growth of interest in Quantum Optics and Quantum Metrology in the latest years shows the impact of this field on the current technologies. The observation of quantum effects in different scenarios gave room to interesting fields in physics. Moreover, in order to understand, verify and simulate quantum effects, optics setups are the most advanced within the current technology. However, there are still fundamental challenges in optics which require thorough analysis. In this thesis, I will tackle the limitations in slit-interference and image resolution, proposing novel measurements exploiting the quantum mechanical nature of light.

In 1879, Lord Rayleigh defined a fundamental limit in resolving incoherent sources [4], due to diffraction effects two sources very close to each other cannot be resolved. In 1901, Planck postulated the energy quantization based on the black-body radiation [5]. This phenomena demonstrated the need for developing a mathematical formalism suitable to describe the quantum phenomena. For this quantum theory was solidified including results from statistics [6] and generalization of classical effects [7, 8].

In 1973, Helstrom reformulated the problem of two sources resolution from the point of view of parameter estimation [9], incorporating the laws of quantum theory. However, this derivation resulted in unfeasible measurement strategies, and the Rayleigh's criteria or *Rayleigh's curse* resulted in being a limitation in optics resolution for over a century. Nevertheless, the pursue for a more complete theory for parameter estimation in quantum states remained [10, 11].

Later with the advances in the fields of quantum information [12] and quantum metrology [13] it was possible to revisit the limits in the field of quantum optics, in the attempt to overcome fundamental limits. In 2016, Tsang *et.al.* [2] used quantum theory to propose feasible experimental methods to resolve two

incoherent point sources bellow the Rayleigh limit. The results of Tsang, solve the multi-parameter estimation issue for the separation and centroid of two point sources. This work resulted in a plethora of theoretical [14–25] as well experimental [26–33] results.

However, the measurement strategy derived to estimate the separation estimation depends on placing the measurement device on the exact centroid of the distribution. In Chap. 4 of this thesis, I quantify the effects of misalignment of the measurement device in estimating the two sources separation, and propose a linear optical implementation capable of mitigating the misalignment effects [34]. In addition, I propose an alternative measurement strategy which does not require knowledge of the centroid of the distribution.

On a different topic, after the success of experimentally implementing quantum entangled states [35–37], the task of estimating a quantum state using tomography measurements became fundamental [38, 39]. The error in tomography measurements depends not only on the experimental uncertainty, but also on the state estimation methods. The error in the estimation methods is called confidence region, and it defines a region in the state's space where the quantum state can be found with the desired confidence. There are different methods to compute confidence regions in the literature [3, 40–44]. These methods depend on the number of experimental repetitions (prepare-and-measure settings) and on the chosen measurement strategies. After analyzing all the methods in the literature for computing confidence regions, I choose two of the most relevant to do a comparative study for fixed (non-adaptive) measurement strategies in Chap. 5.

Regarding fundamentals of quantum mechanics, Yabuki questioned the agreement between the solution to optical slits experiments, as for example, the double -slit experiment [45] with the quantum theory in 1986 [46]. In this work, the author argues that a consistent theory should include nonclassical paths[1], which would affect the intensity in slits interference. It was not until 2010 an attempt to include the nonclassical paths in optical slits experiments [47], leading to more precise interference measurements [48, 49]. In Chap. 3 I discuss a experimental setup with atoms and cavities, capable of detecting the nonclassical paths with 1% probability; I also show how this setup can be used to erase and restore the coherence of the nonclassical paths, discussing how the same setup can measure the Born-rule violation [50].

[1] Feynman paths going through more than one slit.

1.1 Publications

Below is a list of journal articles that have been either published or submitted during this doctorate research.

- Significant nonclassical paths with atoms and cavities in the double-slit experiment
  J.O. de Almeida, M. Lewenstein and J.Q. Quach, *Physical Review A* **102**, 042225 (2020) [50] - Published

- Discrimination and estimation of incoherent sources under misalignment
  J. O. de Almeida, J. Kołodyński, C. Hirche, M. Lewenstein, and M. Skotiniotis, *Physical Review A* **103**, 022406 (2021) [34] - Published

- Collective super-resolving measurements for mixed bosonic states
  J. O. de Almeida, M. Lewenstein, and M. Skotiniotis, *arXiv*, **2110.00986** (2021) v1 [51] - results currently under revision.

Chapter 2

Preliminaries

The light-matter interaction has been vastly studied in the last 400 years. To detect the oscillatory behavior of light or matter in space requires monitoring the incoming radiation using photodetectors with shaped apertures or observing interference patterns after the interaction with objects or slits.

The most general phenomena to describe the interaction between waves and obstacles is diffraction. It can be interpreted qualitatively using the Huygens principle, in which each point in the light source emits a spherical wave, and each point in this wave emits a secondary spherical wave. There is a general solution that quantifies the Huygens principle and the diffraction effects [52], which captures how waves transform in the presence of obstacles of any shape, for example, around apertures or slits.

In diffraction effects, it is common to come across fundamental limits due to destructive interference or approximations that do not include the full description of the physical systems. With the advances in quantum mechanics and quantum information theory, these limits must be reconsidered including a complete description of the phenomena.

In this thesis I will explore these limitations and discuss methods to perform more precise measurements, either in image resolution or in interference experiments.

In this chapter I will present the basic principles to understand the topics of this thesis. In the first section I introduce the diffraction limits on resolution and in double-slit interference, in the second section I discuss the basic principles of quantum mechanics and quantum state tomography and in the last I present the basic concepts of statistical inference.

2.1 Diffraction limited optical resolution and double-slit interference

This section will discuss two fundamental issues in optics, for the topics of interest in this thesis. In the first one, I discuss the limits in spatial resolution of sources in the far-field regime, and in the second, I discuss the limitations in the double-slit experiment.

To resolve the image of one or more light sources[1] far away from the detection apparatus has a fundamental limit that was quantified by Rayleigh in 1879 [4]. This limitation is due to destructive interference of the source's diffracted image through the detector's aperture. This limit, know as Rayleigh criteria or diffraction limit depends on the source-detector distance, on the shape of the detection aperture and on the source's wavelength.

In the double-slit experiment, the effects of the slits alter the spherical wavefront from the source, causing interference between each slit wavefront. Intuitively, the intensity pattern after the double-slit is the sum of the field in each slit, squared. Even though this is a very good approximation [46], a complete description requires to include paths crossing both slits as I discuss in 2.1.2 [53].

The limits on spatial resolution and double-slit interference are due to different technical limitations; in the next section, I will explain the diffraction limit in optical imaging.

2.1.1 Diffraction limit in optical imaging

To image light sources far away from the detection setup requires a set of lenses and apertures that allow for processing the spatial profile of the emitters. In this regime, the paraxial approximation holds, and the light from the sources is diffracted through the detection aperture, changing the transverse intensity profile.

To model the general problem of a point source emitter diffracted through an aperture and observed in an apparatus, one can calculate the electric field solving the Fresnel-Kirchhoff integral in the paraxial regime. In this regime, the source is far from the detector, and the Fraunhofer approximation holds; therefore, the wavefront can be considered as a plane wave, and the field is [52]

$$U = \frac{1}{2\pi} \int \int e^{i\boldsymbol{k}.\boldsymbol{r}} d\mathcal{A}, \tag{2.1}$$

where $\boldsymbol{k}$ is the wavenumber vector, $\boldsymbol{r}$ is the propagation length vector and $d\mathcal{A}$ is the aperture's area element. The intensity of the distribution as a function of

[1] a better image resolution means more image detail.

the position of an apparatus distant from the aperture is $I = |U|^2$.

Under these conditions, the minimal spatial resolution of an emitter in the image plane is fundamentally limited due to diffraction effects. Here I analyze the diffraction limit on the angular resolution, the angle between the propagation direction, and point of observation ϕ, for different apertures shapes, represented in Fig. 2.1.

Using Eq. 2.1 one can find the general expression for the electric field, including the presence of the slits and objects; in calculating the field transmitted through an aperture, we can obtain the detected intensity.

In case of a uni-dimensional aperture the field as a function of the angle ϕ is

$$U(\phi) = \frac{1}{\sqrt{2\pi}} \int_{-\infty}^{\infty} e^{iky \sin\phi} f(y) dy \tag{2.2}$$

where $k = 2\pi/\lambda$, λ is the source wavelength and $f(y)$ is the aperture's spatial distribution.

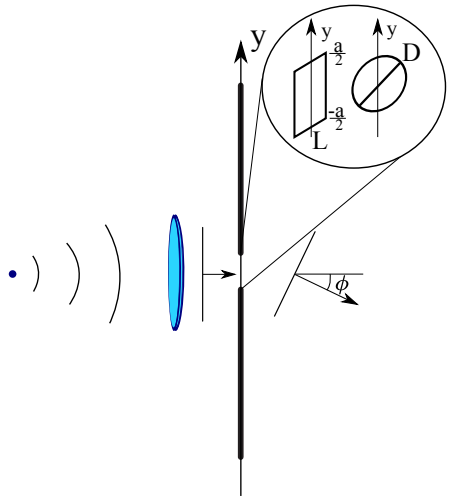

Figure 2.1: *Scheme for diffraction through apertures, rectangular of size L.a and circular of diameter D.*

In the simplest example of a single-slit square aperture of length a and width L, the area element is $f(y)\, dy = L\, dy$ to be integrated in the interval $[-a/2, a/2]$, therefore Eq. (2.2) reads

$$U(\phi) = \frac{1}{\sqrt{2\pi}} \left(\frac{2L \sin\left(\frac{1}{2} ka \sin\phi\right)}{k \sin\phi} \right) \propto \operatorname{sinc}\left(\frac{1}{2} ka \sin\phi\right), \tag{2.3}$$

with the respective intensity

$$I(\phi) \approx I_0 \operatorname{sinc}\left(\frac{1}{2} ka \sin\phi\right)^2. \tag{2.4}$$

In this case the first diffraction minimum occurs for $\frac{1}{2} ka \sin\phi = \pi$. Assuming ϕ small, the first minima of intensity occurs for $\phi \approx \frac{\lambda}{D}$. This is the minimal resolution for the square aperture.

Alternatively, a circular aperture with diameter D, has the area element $f(y)\,dy = \sqrt{D^2 - 4y^2}\,dy$ integrated in the interval ϕ $[-D/2, D/2]$. The electric field as a function of the angular resolution is

$$U(\phi) = \left(\frac{\pi D J_1\left(\frac{kD}{2}\sin\phi\right)}{k\sin\phi}\right), \tag{2.5}$$

where $J_1(x)$ is the Bessel function. The intensity is

$$I(\phi) \approx I_0 \left(\frac{J_1\left(\frac{kD}{2}\sin\phi\right)}{\frac{kD}{2}\sin\phi}\right)^2. \tag{2.6}$$

The first zero for the Bessel function, occurs at $J_1(3.8317)$, which means the minimal angular resolution for circular aperture is $\phi \approx 1.22\frac{\lambda}{D}$, this result sets the Rayleigh limit to optical resolution of telescopes, microscopes and human eye.

2.1.2 Young's experiment

The double-slit experiment is the foundational experiment first realized by Young in 1801 (scheme presented in Fig. 2.2a), that showed the wave nature of light. In the original experiment, sunlight was used, but any bright source would work. Light passes through a pinhole, illuminates a double-slit, and is observed in a detection screen.

The intensity pattern observed in the detection screen is typically calculated based on the superposition of the field in each slit as

$$\Psi(\boldsymbol{r}) = \Psi_A(\boldsymbol{r}) + \Psi_B(\boldsymbol{r}), \tag{2.7}$$

where each $\Psi_i(\boldsymbol{r}) = \frac{e^{i(\boldsymbol{k}.\boldsymbol{r}_i - \omega t)}}{\boldsymbol{r}_i}$, where $\boldsymbol{k}$ is the wavenumber vector and $\boldsymbol{r}$ is the vector from the slit to the point of observation. The relative phase between $\Psi_A(\boldsymbol{r})$ and $\Psi_B(\boldsymbol{r})$ is proportional to the path difference from the slits to the detection screen

$$k(r_A - r_B) = \pm 2n\pi. \tag{2.8}$$

Even though this result roughly reproduces the interference pattern detected, it is only an approximation as $\Psi_A(\boldsymbol{r})$ is the solution to Maxwell's equations without the presence of slit B, and vice-versa, as represented in Fig. 2.2b and c.

A more thorough solution to this problem takes into account the Feynman path integral formulation, where all possible paths from the source to the detection screen are relevant [54]; it includes not only of the direct paths from the source to the detection screen, but also of other possible paths crossing both slits [46]. This topic is discussed in detail in Chap. 3

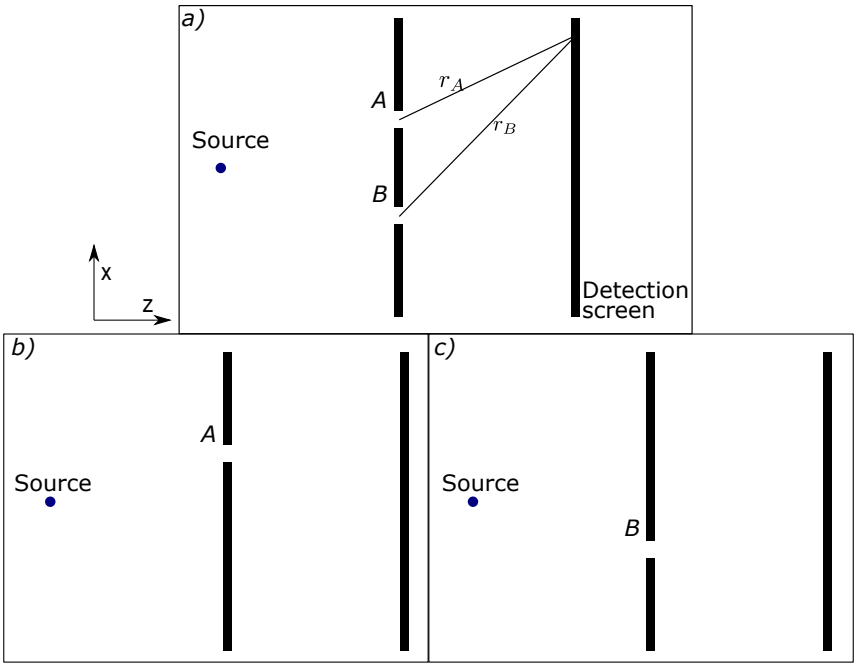

Figure 2.2: *a) Double-slit set up with two slits open. b) Single-slit set up, with slit A open. c) Single-slit set up, with slit B open.*

The double-slit experiment was also repeated in 1928 by Davisson and Germer [55] with a source of electron-beam, demonstrating electrons have the same wave behaviour, this was later extended to atoms and molecules [56–58], confirming De Broglie's hypothesis [59] of wave-particle duality a key prediction of the quantum theory which I now outline.

2.2 Introduction to quantum formalism

In this section, I plan to define the basic concepts of quantum mechanics necessary to understand the results in this thesis. I first define the basic axioms of quantum mechanics, then I introduce basic operations with quantum states as well as quantum state tomography.

In quantum mechanics, the mathematical objects contain all the information on the physical system; these objects are called quantum states, and a projective measurement can extract a physical quantity from such a state. The basic postulates for quantum mechanics are [6]

- At each instant, the state of the system can be represented as a vector in the Hilbert space[2], which in the Dirac notation is $|\Psi\rangle \in \mathcal{H}$. As a consequence a superposition of two states is again a state of the system, i.e. if $|\Psi\rangle, |\phi\rangle \in \mathcal{H}$ then $\alpha|\Psi\rangle + \beta|\phi\rangle \in \mathcal{H}$ for $\alpha, \beta \in \mathbb{C}$ and $|\alpha|^2 + |\beta|^2 = 1$.

- Every observable attribute of a physical system is described by an operator that acts on the states describing the system. $\hat{\mathcal{A}} : |\Psi\rangle \to |\Psi'\rangle = \hat{\mathcal{A}}|\Psi\rangle$, every operator has eigenstates $\hat{\mathcal{A}}|a\rangle = a|a\rangle$.

- The only possible measurement outcome of an observable $\mathcal{A}$ is one of the eigenvalues of the corresponding operator $\hat{\mathcal{A}}$; this implies the operators are Hermitian with orthogonal eigenstates forming a basis.

- When a measurement of an observable $\mathcal{A}$ is made on state $|\Psi\rangle$, the probability of obtaining an eigenvalue a_n is given by the square of the inner product of $|\Psi\rangle$ with the eigenstate $|a_n\rangle$, $|\langle a_n|\Psi\rangle|^2$, a direct consequence of this is the Born rule.

- Immediately after the measurement of an observable $\mathcal{A}$ has yielded a value a_n, the state of the system is the normalized eigenstate $|a_n\rangle$.

- The time evolution of a quantum system preserves the normalization of the associated state. The time evolution of a state is described by $|\Psi(t)\rangle = \hat{U}(t - t_0)|\Psi(t_0)\rangle$; this requires the state to obey the Schrödinger's equation $i\hbar\frac{\partial|\Psi(t)\rangle}{\partial t} = \hat{H}|\Psi(t)\rangle$, for $\hat{H}$ the Hamiltonian operator.

The probability density associated with a quantum state is called the density matrix, and it's the product of the state with its conjugate transpose $\rho = |\Psi\rangle\langle\Psi|$; this matrix must be positive semi-definite, hermitian, and of trace one. However, not all density matrices can be fully described with one state (pure states); it

[2] a complex vector space equipped with an inner product complete in its norm.

might be the case a linear combination of density matrices is required to fully describe a system (mixed states)

$$\rho = \sum_i q_i \rho_i. \tag{2.9}$$

2.2.1 Operations with quantum states

In this thesis, our analysis is restricted to a particular type of measurement strategies and quantum states, which I now review.

A particular type of measurement is the Positive Operator-Valued Measurement (POVM), an hermitian, positive semi-definite operator. The simplest POVM is a projective measurement a set of operators that sum to identity

$$\sum_{i=1}^{n} E_i = \mathbb{1}. \tag{2.10}$$

A key consequence of the postulates of quantum mechanics is the Born rule, which can be defined as the probability outcome of a projective measurement strategy

$$p_i := \mathrm{Tr}\left(E_i |\Psi\rangle\langle\Psi|\right) \tag{2.11}$$

An example of the Born rule is the projective measurement in the position representation $|x\rangle\langle x|$, yielding

$$p(x) := \mathrm{Tr}\left(|x\rangle\langle x||\Psi\rangle\langle\Psi|\right) = |\Psi(x)|^2 \tag{2.12}$$

In case the quantum state is a superposition of two other states $|\Psi\rangle = |\Psi_1\rangle + |\Psi_2\rangle$, the probability distribution is therefore $|\Psi_1(x) + \Psi_2(x)|^2$. This shows that regardless of the number of states $|\Psi\rangle$ is superposed in, the Born rule will guarantee pairwise interference only. In Chapter 3 we discuss different methods that attempted to test the Born rule questioning the pairwise interference in systems with two and more slits.

A important class of states relevant in this thesis are

$$|\Psi_0\rangle = \int_{-\infty}^{\infty} \Psi_0(x)|x\rangle \, \mathrm{d}x, \tag{2.13}$$

where $\Psi_0(x) = \frac{1}{\sqrt[4]{2\pi\,\sigma^2}} e^{-\frac{x^2}{4\sigma^2}}$ is the Gaussian distribution. This is the fundamental state solution of the harmonic oscillator.

2.2.2 Quantum state tomography

Quantum state tomography[3] is the task of fully characterizing a quantum state based on the result of projective measurements. Although, the result of a single measurement is often not enough to reconstruct a state and it perturbs the state being measured. Therefore, quantum state tomography is the task of reconstructing a quantum state by performing different projective measurements on copies of the unknown quantum state.

Formally it consists of preparing copies of the same d-dimensional state ρ (ρ is a element of the set $\mathcal{S}(\mathcal{H}_d)$ of density operators in a d-dimensional Hilbert space) and measuring with m different feasible POVM measurement strategies, E_i, with $i = 1, ..., m$. After N prepare-and-measurement rounds the frequency of each outcome is

$$f_i = \frac{n_i}{N} \qquad \text{for } i \in [m]\,, \tag{2.14}$$

where n_i is the number of times outcome i is observed. As a matter of fact, if the experiment is repeated many times the probabilities of each outcome can be empirically estimated based on the frequency $\lim_{N\to\infty} f_i = p_i$.

There are different methods to estimate a quantum state based on the data outcomes of an experiment [60–62]. Often the experimental results for state estimation are presented without error bars, or the error depends on the features of the designed setup. Although, the state estimation methods have intrinsic uncertainties due to statistical errors arising from the finiteness of the data size. There are different methods to compute this uncertainty or *confidence regions* [63].

The goal is to compare quantum state tomography procedures, based on the data set $\boldsymbol{n} = (n_1, ..., n_m)$, which gives a region $\Gamma(\boldsymbol{n})$ in which the unknown quantum state ρ can be found with a desired confidence $1 - \delta$

$$\Pr\left[\rho \in \Gamma(\boldsymbol{n})\right] \geq 1 - \delta, \tag{2.15}$$

where $\Pr[\cdot]$ the probability over all outcomes $\boldsymbol{n}$, δ is usually small and between $0 \leq \delta \leq 1$.

In the last part of this thesis, I will compare the different methods in the literature to calculate confidence regions and present the current work in progress; meanwhile, in the next subsection I present how to estimate latent parameter based on a data set.

[3] In analogy to the reconstruction of a three-dimensional image based on a series of two-dimensional projections.

2.3 Limits of latent parameters

The main question that statisticians have addressed is how to efficiently infer a latent parameter from a probabilistic data set. More specifically, to investigate if one or more global parameters, change the probability distribution of a measurement outcome.

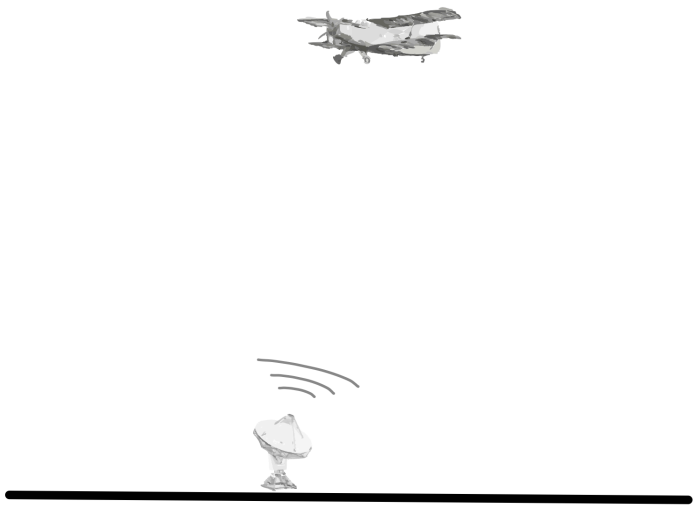

Figure 2.3: *Ilustration of a eletromagnetic sensor*

This theory applies to many systems; it has been the object of study to build sensors and estimate an object's position. For example, to estimate the position of an aircraft based on a transmitted electromagnetic pulse, reflected by the aircraft and absorbed by the antenna seconds later. We can use the probability of detecting the electromagnetic pulse after a given time interval to estimate the aircraft position based on the pulse velocity and intensity information [13].

In our problem, we have a data set, from which each output depends on the unknown parameter λ. Our goal is to determine λ based on the data set, or to build an estimate $\tilde{\lambda}$, function of this data set, which is as close as possible to the true value λ.

In this section, I build the mathematical formulation for estimating multiple parameters from a data set for classical and quantum probability distributions.

2.3.1 Parameter estimation

Suppose an experimental realization gives an N-point data set $\boldsymbol{y} = \{y_1, y_2, ..., y_N\}$, corresponding to the number of times the experiment is repeated. Each output y_i, $i = 1, ..., N$ is a random variable independently and identically distributed (i.i.d.) according to the same probability distribution, $p(y|\lambda)$, conditioned on the latent parameter λ. Here I explain how to build an estimate[4], $\tilde{\lambda}(\boldsymbol{y})$, of the latent parameter λ based on the data set.

There are two approaches to the parameter estimation problem, the Bayesian and the Frequentist. The Bayesian approach, assumes the estimated parameters to be a random variable, and it relies on optimizing the estimator over a range of values the parameter may take, taking into account any information on the parameter before obtaining the data set.

The Frequentist approach, assumes the estimator is a deterministic variable, and the relative frequency of an event measures the probability of that event to happen. In this thesis, I use only the Frequentist approach, which I now explain in detail.

In order to build a well representative estimate of the true parameter, we impose conditions on a function of the estimate, such as the limits in which it should yield the true value of the parameter. The estimator is unbiased if on average it yields the true value of the parameter [64]

$$\langle \tilde{\lambda}(\boldsymbol{y}) - \lambda \rangle = \int (\tilde{\lambda}(\boldsymbol{y}) - \lambda) p(\boldsymbol{y}|\lambda) d\boldsymbol{y} = 0 \tag{2.16}$$

Typically the data sample probability distribution is known, and the most common example is the Gaussian distribution centered around the latent parameter

$$p(y_i|\lambda) = \frac{1}{\sqrt{2\pi\sigma^2}} \exp\left(-\frac{1}{\sqrt{2\sigma^2}}(y_i - \lambda)^2\right). \tag{2.17}$$

The measurement strategy is efficient if the probability $p(\boldsymbol{y}|\lambda)$ of outcome $\boldsymbol{y}$ is strongly affected by the variable λ [65]. The estimator is accurate if the probability is centered around the true value of the parameter, and is precise if the probability has a small variance with around its mean value.

In order to ensure the measurement is efficient, the maximum Likelihood (mL) function selects those values of the parameter that maximize the probability distribution function, or more conveniently, the natural logarithm of the probability distribution, as the logarithm is a monotonic function, the maximum occurs for the same values of the parameter λ.

$$\tilde{\lambda}^{mL}(\boldsymbol{y}) = \arg\max_{\lambda} \ln p(\boldsymbol{y}|\lambda), \tag{2.18}$$

[4] "to guess or calculate the cost, size, value, etc. of something"-Cambridge dictionary

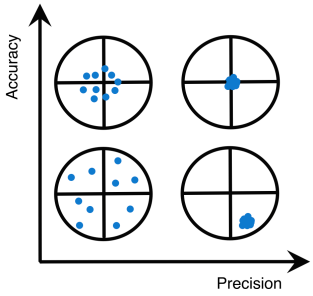

Figure 2.4: *Graph illustrating examples of accurate and precise distributions. The estimator is accurate if the distribution is centered around the true value of the parameter (center of the cross), the estimator is precise if the variance of the distribution is small.*

this is also called the Log-Likelihood function. Consequently, this ensures the estimator is precise, as we now see in detail.

Assuming the Log-Likelihood function is regular with the parameter, it will have zero first moment,

$$E\left[\frac{\partial \ln p(\boldsymbol{y}|\lambda)}{\partial \lambda}\right] = \int \left(\frac{\partial p(\boldsymbol{y}|\lambda)}{\partial \lambda}\right) d\boldsymbol{y} = \frac{\partial}{\partial \lambda}\int p(\boldsymbol{y}|\lambda) d\boldsymbol{y} = 0. \tag{2.19}$$

The second moment is a measure of the curvature or variance of the parameter

$$F[\lambda] = -E\left[\frac{\partial^2 \ln p(\boldsymbol{y}|\lambda)}{\partial \lambda^2}\right] = \int \frac{1}{p(\boldsymbol{y}|\lambda)}\left(\frac{\partial p(\boldsymbol{y}|\lambda)}{\partial \lambda}\right)^2 d\boldsymbol{y}. \tag{2.20}$$

The quantity in Eq. (2.20) is also called the Fisher information, and it quantifies the amount of information the probability carries on the parameter λ [66], it scales with the increase in the number of repetitions N, such that $F_N[\lambda] = N\,F[\lambda]$.

In order to find the bound on the variance of the estimator $\mathrm{Var}[\tilde{\lambda}(y)]$, we can derive the unbiasedness condition

$$\begin{aligned} &\frac{\partial}{\partial \lambda}\int (\tilde{\lambda}(y) - \lambda) p(y|\lambda) dy = 0, \\ &-\int p(y|\lambda) dy + \int (\tilde{\lambda}(y) - \lambda)\frac{\partial p(y|\lambda)}{\partial \lambda} dy = 0, \\ &\int (\tilde{\lambda}(y) - \lambda)\frac{\partial p(y|\lambda)}{\partial \lambda} dy = 1. \end{aligned} \tag{2.21}$$

Writing the derivative as the logarithmic function, $\frac{\partial \ln p(y|\lambda)}{\partial \lambda} = \frac{1}{p(y|\lambda)}\frac{\partial p(y|\lambda)}{\partial \lambda}$, Eq. (2.21)

becomes

$$\int (\tilde{\lambda}(y) - \lambda) p(y|\lambda) \frac{\partial \ln p(y|\lambda)}{\partial \lambda} dy = 1. \tag{2.22}$$

Squaring the integral, and using the Cauchy–Schwarz inequality one obtains

$$\begin{aligned} &\left(\int \left((\tilde{\lambda}(y) - \lambda) \sqrt{p(y|\lambda)} \right) \left(\sqrt{p(y|\lambda)} \frac{\partial \ln p(y|\lambda)}{\partial \lambda} dy \right) \right)^2 \leq \\ &\int (\tilde{\lambda}(y) - \lambda)^2 p(y|\lambda) dy \int p(y|\lambda) \left(\frac{\partial \ln p(y|\lambda)}{\partial \lambda} \right)^2 dy. \end{aligned} \tag{2.23}$$

Using the result in Eq. 2.22 we finally get

$$\begin{aligned} 1 &\leq \int (\tilde{\lambda}(y) - \lambda)^2 p(y|\lambda) dy \int p(y|\lambda) \left(\frac{\partial \ln p(y|\lambda)}{\partial \lambda} \right)^2 dy \\ 1 &\leq \mathrm{Var}(\tilde{\lambda}(y)) F[\lambda]. \end{aligned} \tag{2.24}$$

Thus, the bound on the variance of any unbiased estimator is

$$\mathrm{Var}(\tilde{\lambda}(y)) \geq F[\lambda]^{-1}, \tag{2.25}$$

Including the scaling of the Fisher information with the number of experimental repetitions, we arrive at the Cramér-Rao bound [67, 68]

$$\mathrm{Var}(\tilde{\lambda}_N(\boldsymbol{y})) \geq \frac{F[\lambda]^{-1}}{N}, \tag{2.26}$$

which is always achievable in the limit of infinite repetitions.

In order to estimate more than one latent parameter in the probability distribution $p(\boldsymbol{y}|\boldsymbol{\lambda})$, with $\boldsymbol{\lambda} = \lambda_1, \lambda_2, ..., \lambda_k$, the corresponding multivariate Cramér-Rao bound, follows analogously as $\tilde{\boldsymbol{\lambda}} = \tilde{\lambda}_1, \tilde{\lambda}_2, ..., \tilde{\lambda}_k$ as

$$\mathrm{Cov}(\tilde{\boldsymbol{\lambda}} - \langle \tilde{\boldsymbol{\lambda}} \rangle, \tilde{\boldsymbol{\lambda}} - \langle \tilde{\boldsymbol{\lambda}} \rangle) \geq \frac{\boldsymbol{F}[\boldsymbol{\lambda}]^{-1}}{N}. \tag{2.27}$$

where $F[\boldsymbol{\lambda}]$ is a kxk matrix defined as

$$F[\boldsymbol{\lambda}]_{ij} = \int \frac{1}{p(\boldsymbol{y}|\boldsymbol{\lambda})} \left(\frac{\partial p(\boldsymbol{y}|\boldsymbol{\lambda})}{\partial \lambda_i} \right) \left(\frac{\partial p(\boldsymbol{y}|\boldsymbol{\lambda})}{\partial \lambda_j} \right) d\boldsymbol{y} \tag{2.28}$$

The maximum Likelihood estimate always saturates the Cramér-Rao bound in the limit of large N, for both single or multi-parameter estimation scenarios.

All the theory to this point defines the bound on the precision estimation for a given measurement strategy. In quantum mechanics, we must maximize the Fisher information [69] over all possible measurement strategies, for this we define the Born rule in the operator form

$$p(\boldsymbol{y}|\boldsymbol{\lambda}) := \mathrm{Tr}\left(E_{\boldsymbol{y}} \rho(\boldsymbol{\lambda}) \right) \tag{2.29}$$

where $\{E_{\boldsymbol{y}}\}$ are any set of POVM measurements.

The Quantum Fisher information is thus

$$\boldsymbol{\mathcal{F}}(\rho(\boldsymbol{\lambda})) := \max_{E_{\boldsymbol{y}} \geq 0} \boldsymbol{F}\left(p(\boldsymbol{y}|\rho(\boldsymbol{\lambda}))\right), \tag{2.30}$$

where an optimal measurement strategy $\mathcal{L}_m$, also called Symmetric Logarithmic Derivative (SLD), can be obtained solving the following equation

$$\begin{aligned} \frac{\partial \rho(\boldsymbol{\lambda})}{\partial \lambda_m} &= \mathcal{L}_m \rho(\boldsymbol{\lambda}) + \rho(\boldsymbol{\lambda}) \mathcal{L}_m \\ \mathcal{L}_m &= 2 \sum_{\substack{\alpha,\beta \\ \rho_\alpha + \rho_\beta \neq 0}} \frac{\langle \Psi_\alpha | \partial_m \rho | \Psi_\beta \rangle}{\rho_\alpha + \rho_\beta} |\Psi_\alpha\rangle\langle\Psi_\beta| \end{aligned} \tag{2.31}$$

where $|\Psi_\gamma\rangle\langle\Psi_\gamma|$ is the eigenbasis of $\rho = \sum_\gamma \rho_\gamma |\Psi_\gamma\rangle\langle\Psi_\gamma|$. The Quantum Fisher information can then be written as

$$\mathcal{F}[\boldsymbol{\lambda}]_{ij} = \mathrm{Re}\left[\mathrm{Tr}\left[\mathcal{L}_i(\rho)\mathcal{L}_j(\rho)\rho\right]\right]. \tag{2.32}$$

Moreover, similarly to the Classical Fisher Information, the Quantum Fisher information can be interpreted as an information measure [70], it can be explicitly written in the eigenbasis of the density matrix as

$$\boldsymbol{\mathcal{F}}[\boldsymbol{\lambda}] = \sum_{\substack{\gamma \\ \rho_\gamma \neq 0}} \frac{\dot{\rho}_\gamma(\boldsymbol{\lambda})^2}{\rho_\gamma(\boldsymbol{\lambda})} + 2 \sum_{\substack{\alpha,\beta \\ \rho_\alpha + \rho_\beta \neq 0}} \frac{\left(\rho_\alpha(\boldsymbol{\lambda}) - \rho_\beta(\boldsymbol{\lambda})\right)^2}{\rho_\alpha(\boldsymbol{\lambda}) + \rho_\beta(\boldsymbol{\lambda})} |\langle \dot{\Psi}_\alpha | \Psi_\beta \rangle|^2 \tag{2.33}$$

where the $\dot{z} = \frac{\partial z}{\partial \lambda_i}$ represents the derivative with respect to each parameter $\boldsymbol{\lambda}$, this equation is demonstrated in details in [71]. As we can see, the Quantum Fisher information can be divided in two parts, the first sum or classical part, quantifies the information encoded in the eigenvalues of ρ, whereas the second sum or quantum part, quantifies how the eigenvectors change with the parameter.

The Quantum Cramér-Rao bound is

$$\mathrm{Var}(\tilde{\lambda}(\boldsymbol{y})) \geq \frac{F[\lambda]^{-1}}{N} \geq \frac{\mathcal{F}[\lambda]^{-1}}{N}. \tag{2.34}$$

For a single parameter, the Quantum Fisher information upper bounds the corresponding Classical Fisher information, i.e. $\mathcal{F}[\lambda] \geq F[\lambda]$ and there always exists a projective measurement defined in the basis of the SLD, for which the Quantum Cramér-Rao bound is saturated [69].

In multi parameter estimation, however the Fisher information bounds the covariance of every two parameters

$$\mathrm{Cov}(\tilde{\boldsymbol{\lambda}} - \langle\tilde{\boldsymbol{\lambda}}\rangle, \tilde{\boldsymbol{\lambda}} - \langle\tilde{\boldsymbol{\lambda}}\rangle) \geq \frac{\boldsymbol{F}[\boldsymbol{\lambda}]^{-1}}{N} \geq \frac{\boldsymbol{\mathcal{F}}[\boldsymbol{\lambda}]^{-1}}{N}, \tag{2.35}$$

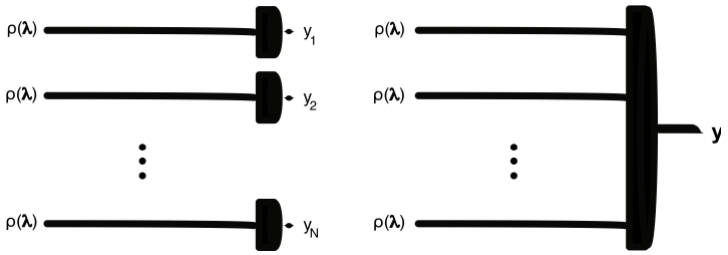

Figure 2.5: *Illustration of single measurement and collective measurement.Left scheme: each copy of the initial state is measured with a projective measurement yielding an outcome y_i. Right scheme: All copies of the initial state are measured globally yielding one outcome that can be a N dimensional vector.*

and is only saturable if the SLDs of all pairs of parameters commute or iff their trace with the initial state is zero, $\mathrm{Tr}\left(\rho(\boldsymbol{\lambda})[\mathcal{L}_{\lambda_i}, \mathcal{L}_{\lambda_j}]\right) = 0$ [72].

These results imply a difference in the single-vs-multi parameter scenarios. In the single parameter case, the optimal measurement operator, or the projector onto eigenvectors of the SLD that allows $\mathcal{F}[\lambda] \geq F[\lambda]$, is iid, i.e. identical on each of the N copies (represented in the left scheme of Fig. 2.5). In contrast to the multiparameter case, where the scheme can only be optimal if the initial states are pure [72]. In the case of initial mixed states, the optimal measurement strategy, requires a collective measurement on all N copies of the initial state (obtained the N experimental repetitions), this alternative is represented in the right scheme of Fig. 2.5.

2.3.2 Decision Theory - State discrimination

Decision theory is a post-processing method to analyze an experimental data set and decide among two or more distributions that best describe this data set. For example it can be used to compare detected signals and decide if it contains noise or not.The first models to this theory are in [73–77].

The hypothesis testing procedure relies on monitoring the system and assigning a hypotheses to each different probability distributions the data set may have. To decide the most suitable hypothesis I will follow the Neyman–Pearson approach, where the decision is based on the comparison between the probability distributions [78].

The simplest scenario is binary hypothesis testing, where there are only two possible hypotheses H_1 and H_2, and the goal is to determine with minimum error probability the truthful hypothesis based on the data set $\boldsymbol{y} = \{y_1, y_2, ..., y_n\}$.

The data set can be independent and identically distributed (i.i.d.) according to two probability distributions $p(\boldsymbol{y}|H_i \text{ is True})$, $i = 1, 2$, each representing a true hypothesis. The decision-making process is to choose one of the two hypothesis based on the data set, represented by the function $f(\boldsymbol{y}) = H_i$, $i = 1, 2$.

The total error probability is the sum of mistaking hypothesis two for one $p\left(f(\boldsymbol{y}) = H_2|H_1\right)$ (type-1), and mistaking hypothesis one for two $p\left(f(\boldsymbol{y}) = H_1|H_2\right)$ (type-2). Any prior knowledge on the hypothesis can be included in its respective weights, Π_i, $i = 1, 2$ [77, 79] so that the average probability of error is

$$P_{\text{err}} = \Pi_1\, p\left(f(\boldsymbol{y}) = H_2|H_1\right) + \Pi_2\, p\left(f(\boldsymbol{y}) = H_1|H_2\right), \tag{2.36}$$

for equally likely hypothesis $\Pi_1 = \Pi_2 = \frac{1}{2}$.

We can choose the most likely hypothesis by comparing the following probability distributions[5]

$$f(\boldsymbol{y}) = \begin{cases} H_1 & \text{if} \quad \Pi_1\, p\left(\boldsymbol{y}|H_1\right) > \Pi_2\, p\left(\boldsymbol{y}|H_2\right), \\ H_2 & \text{if} \quad \Pi_2\, p\left(\boldsymbol{y}|H_2\right) > \Pi_1\, p\left(\boldsymbol{y}|H_1\right), \\ \text{any} & \text{if} \quad \Pi_1\, p\left(\boldsymbol{y}|H_1\right) = \Pi_2\, p\left(\boldsymbol{y}|H_2\right), \end{cases} \tag{2.37}$$

with this strategy, the the average probability of error becomes

$$P_{\text{err}} = \sum_{\boldsymbol{y}} \min\left\{\Pi_1\, p\left(\boldsymbol{y}|H_1\right), \Pi_2\, p\left(\boldsymbol{y}|H_2\right)\right\}. \tag{2.38}$$

One way to obtain better statistics for the error probability, is repeating the experimental setting N times before making a guess. This will give a set of data sets $\boldsymbol{y}^{(N)} = \{\boldsymbol{y}_{(1)}, \boldsymbol{y}_{(2)}, ..., \boldsymbol{y}_{(N)}\}$, distributed according to $p\left(\boldsymbol{y}^{(N)}|H_i\right) = p\left(\boldsymbol{y}_{(1)}|H_i\right) p\left(\boldsymbol{y}_{(2)}|H_i\right) \ldots p\left(\boldsymbol{y}_{(N)}|H_i\right)$, where $i = 1, 2$.

With these tools in hand and the condition on the minimum between any two positive numbers a and b, $\min\{a, b\} \leq a^s b^{1-s}$, for $s \in [0, 1]$, Chernoff derived a bound on the error probability [80] for N experimental repetitions

$$\begin{aligned} P_{\text{err}} &= \sum_{\boldsymbol{y}^{(N)}} \min\left\{\Pi_1\, p\left(\boldsymbol{y}^{(N)}|H_1\right), \Pi_2\, p\left(\boldsymbol{y}^{(N)}|H_2\right)\right\} \\ &\leq \Pi_1^s \Pi_2^{1-s} \sum_{\boldsymbol{y}^{(N)}} \left(\prod_{k=1}^{N} p(\boldsymbol{y}_{(k)}|H_1)^s p(\boldsymbol{y}_{(k)}|H_2)^{1-s}\right) \\ &= \Pi_1^s \Pi_2^{1-s} \left(\sum_{\boldsymbol{y}=y_1}^{y_n} p(\boldsymbol{y}|H_1)^s p(\boldsymbol{y}|H_2)^{1-s}\right)^N \\ P_{\text{err}} &\leq \min_{0 \leq s \leq 1} \Pi_1^s \Pi_2^{1-s} \left(\sum_{\boldsymbol{y}=y_1}^{y_n} p(\boldsymbol{y}|H_1)^s p(\boldsymbol{y}|H_2)^{1-s}\right)^N. \end{aligned} \tag{2.39}$$

[5] this is called the maximum likelihood estimate

This bound is interesting because it is always attainable in the asymptotic limit of $N \to \infty$, and it decays exponentially with the number of repetitions as

$$\lim_{N\to\infty} P_{\text{err}} \sim e^{-N\xi}, \qquad \text{where}$$
$$\xi := -\log \min_{0\le s\le 1} \left(\sum_{\boldsymbol{y}=y_1}^{y_n} p(\boldsymbol{y}|H_1)^s p(\boldsymbol{y}|H_2)^{1-s} \right). \tag{2.40}$$

where ξ is the Chernof number.

The Chernoff bound sets the exponent that minimizes the error probability, and it allows to compare probability distributions based on their distinguishability[6].

In quantum hypothesis testing, the goal is to apply decision theory to decide which of the two quantum states $\rho^{(1)}$ or $\rho^{(2)}$, is the true state. The probability of testing a hypothesis in state $\rho^{(i)}$ is the trace of the corresponding POVM measurement $\{E_y\} = \{E_1, E_2\}$, $E_1 + E_2 = \mathbb{I}$, with the state to be tested, $p\left(y|H_i\right) = \text{Tr}\left(E_y\, \rho^{(i)}\right)$. The error probability is therefore

$$\begin{aligned} P_{\text{err}} =& \Pi_1 \text{Tr}\left[E_2\, \rho^{(1)}\right] + \Pi_2 \text{Tr}\left[E_1\, \rho^{(2)}\right] \\ =& \Pi_2 - \text{Tr}\left[E_2 \left(\Pi_2\, \rho^{(2)} - \Pi_1\, \rho^{(1)}\right)\right] = \Pi_1 - \text{Tr}\left[E_1 \left(\Pi_1\, \rho^{(1)} - \Pi_2\, \rho^{(2)}\right)\right] \end{aligned} \tag{2.41}$$

where a simpler form can be derived taking the average between the two forms of the error probability in Eq. 2.41, where the prior probabilities to sum to one, $\Pi_1 + \Pi_2 = 1$.

In contrast with the classical case, in quantum binary hypothesis testing we are free to choose among the measurement strategies the one that yields the smallest error probability. The optimal measurement was derived by Helstrom [77] and corresponds to a two outcome measurement on the positive and negative eigenspaces of the following operator

$$\Gamma := \Pi_2\, \rho^{(2)} - \Pi_1\, \rho^{(1)}. \tag{2.42}$$

The minimum error probability in discriminating two states $\rho^{(1)}$ and $\rho^{(2)}$ is thus

$$P_{\text{err}} = \frac{1}{2}\left(1 - \left\|\Pi_2\, \rho^{(2)} - \Pi_1\, \rho^{(1)}\right\|_1\right), \tag{2.43}$$

where $\|\Gamma\|_1 = \text{Tr}\,|\Gamma|$ is the trace norm of operator Γ.

[6]For example, to divide N PhD students into two groups balanced according to a given feature or parameter.

Similarly, given N copies of the initial state the optimal measurement strategy, or collective Helstrom measurement is $\Gamma^{\otimes N} = \frac{1}{2}\left(\rho^{(2)\otimes N} - \rho^{(1)\otimes N}\right)$, and the error probability scales with the number of copies as [81]

$$\begin{aligned} \lim_{N\to\infty} P_{\text{err}} &\sim e^{-N\xi^{(QM)}}, \qquad \text{where} \\ \xi \leq \xi^{(QM)} &:= -\log \min_{0\leq s\leq 1} \mathrm{Tr}\left\{ \left(\rho^{(1)}\right)^{s} \left(\rho^{(2)}\right)^{1-s} \right\}. \end{aligned} \tag{2.44}$$

Observe that the Quantum bound is independent of the measurement strategy and its attainability points out the optimal measurement strategy, which in general may be a collective measurement strategy.

Chapter 3

Measuring nonclassical paths with atoms and cavities in the double-slit experiment

In this chapter I discuss the double-slit experiment including the nonclassical paths, Feynman paths that go through both slits. Prior work with atomic interference in the double-slit experiment and cavities as which-way detectors, has shown these paths to be experimentally inaccessible. In this chapter, I show how such a setup can indeed detect nonclassical paths with 1% probability, if different nonclassical paths are included. I also show how this setup can be used to erase and restore the coherence of the nonclassical paths. Finally, I discuss how atom cavities may be used to implement exact measure of Born-rule violation using the Quach parameter [1], which up until now has only been a formal construct. In the last section of this chapter I discuss results which question the use of the Sorkin parameter to test the presence of nonclassical paths.

This chapter is based on:
Significant nonclassical paths with atoms and cavities in the double-slit experiment
J.O. de Almeida, M. Lewenstein and J.Q. Quach, *Physical Review A* **102**, 042225 (2020)

The double-slit experiment is the foundation of studies in interference effects [6, 8, 82] and reveals the wave nature of matter [56, 57, 83, 84]. Typically the nodes (or anti-nodes) are calculated as the result of the path difference arising out of the distance from the slits to the detection screen. This, however, is only an approximation, as first pointed out by Yabuki [46]. In the Feynman path integral formulation of quantum mechanics [53], all possible paths between points contribute to the wave function. The direct or classical paths from the slits to the detection screen are just one set of an infinite number of possible paths. *Higher-order, exoctic* or *nonclassical* paths include paths which enter both slits before reaching the detector, as shown in Fig. 3.1. Typically, these nonclassical paths are much less probable than the direct or *classical* paths; nevertheless, it has been shown that in regimes where the wavelength is large compared to the slit-spacing, these nonclassical paths can be significant [85].

The nonclassical path contributions to the interference pattern is not uniquely a quantum mechanical effect. There have been evidence of such contributions to the interference pattern arising also out of Maxwell's equations, as shown with finite-difference time-domain (FDTD) simulations [86]. The simulations using this method have shown to partially agree with the triple-slit experiment [87, 88].

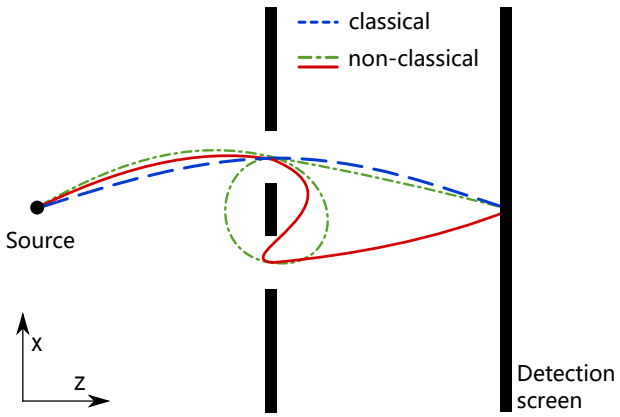

Figure 3.1: *A schematic of the double-slit experiment. The bluedashed line depicts one the many possible classical paths. The red-solid and green-dotted-dashed lines depicts two types of non-classical paths.*

In the double-slit experiment, the particle nature of matter is revealed if one knows which slit the particle went through [89]. In 1991, Scully *et al.* [90]

FDTD is a numerical method to solve Maxwell's equations in infinitesimal time and distance steps.

introduced cavities into the slits as a means to mark which slit the particle went through, thereby acting as which-way detectors. They showed how the setup could implement the delayed-choice quantum erasure experiment using the atomic transition due to atom-light interaction [91–96]. In this setup energy is necessarily exchanged to reveal which-way information. In 2017, de Oliveira *et al.* [97] showed how the setup proposed by Scully can be used to isolate nonclassical paths. Their work consisted of modeling looped trajectories of Rubidium Rydberg atoms in the double-slit experiment, with the result that the probability of detection of these nonclassical paths were too small to be feasible.

The Born rule states that if a quantum object is represented by a wave function $\psi(\mathbf{r}, t)$, then the probability density of detecting it at position $\mathbf{r}$ and time t is given by the absolute square of the wave function [98],

$$P(\mathbf{r}, t) = \psi^*(\mathbf{r}, t)\psi(\mathbf{r}, t) = |\psi(\mathbf{r}, t)|^2 \ . \tag{3.1}$$

Despite being a cornerstone of quantum mechanics, a direct test of the Born rule was not attempted until 2010 by Sinha *et al.* [47]. The test was a measure of the Sorkin parameter [99], which quantifies nonpairwise interference, in a triple-slit experiment [100]. Since the exponent of the Born rule only allows for pairwise interference, a nonzero Sorkin parameter would suggest violation of the Born rule. Shortly after this experiment, it was pointed out that a nonzero Sorkin parameter would not necessarily indicate Born-rule violation [101]; instead it could be a signature of nonclassical paths. Most recently, Quach [1] proposed an alternative parameter, using the double-slit experiment with which-way detectors, as a more accurate measure of Born-rule violation. However, the Quach's parameter up until now, has only been a formal construct.

In this chapter, I first describe the classical and nonclassical paths using Feynman path integral formulation, then I discuss an experimental setup that allows to measure the nonclassical paths with 1% probability. In the following section I analyze the subtleties of this setup and use it to test the Born-rule violation with the Quach parameter as a criteria [50], lastly I discuss why the Sorkin parameter is not a good measure of nonclassical paths an the issues with the results in the literature.

3.1 Classical and nonclassical paths

In the Feynman path integral formulation the probability amplitude is based on the state evolution according to Schrödinger's equation, one of the postulates of quantum mechanics; in this formulation the probability amplitude transition defines the state evolution, and is the sum over all possible trajectories between

the initial (x_0, t_0) and the endpoint (x', t'). In this section, I analyze the different trajectories from the source to the detection screen, specifically the ones defined in Fig. 3.1 using the Feynman propagator.

Using quantum mechanics, following the argument in Sec. 2.1.2, the wavefunction corresponding to the double-slit experiment, represented in Fig. 2.2a is typically calculated as the sum of each individual slit wavefunction $\Psi(x) = \Psi_A(x) + \Psi_B(x)$. However, Ψ_A and Ψ_B are solutions of the Shrödinger equation with different boundary conditions, therefore, correspond to different Hilbert spaces [46].

Assuming the slits are infinite in the y direction (perpendicular to the figure plane), and the slit plane extends infinitely in the x direction, allows us to reduce the system to a one-dimensional problem in the x direction. The source is an atom with wave packet

$$\psi_0\left(x, t=0\right) = \frac{1}{\sqrt{\sigma_0\sqrt{\pi}}} \exp\left[\frac{-x^2}{2{\sigma_0}^2}\right] , \tag{3.2}$$

and width σ_0. The atom wave function at a later time is the weighted sum of all possible paths,

$$\psi(x_f, t_f, t_i) = \int_{-\infty}^{\infty} K(x_f, t_f; x_i, t_i)\psi_0(x_i, t_i)dx_i \ , \tag{3.3}$$

where $K(x_f, t_f; x_i, t_i)$ is the free propagator for a particle with mass $m > 0$ from point (x_i, t_i) to (x_f, t_f):

$$K\left(x_f, t_f; x_i, t_i\right) = \sqrt{\frac{m}{2\pi i\hbar\left(t_f - t_i\right)}} \exp\left[\frac{im\left(x_f - x_i\right)^2}{2\hbar\left(t_f - t_i\right)}\right] . \tag{3.4}$$

The presence of the slit-plane reduces the number of possible paths between the source and the detection screen. I will use this propagator to derive the classical and non-classical paths in this Chapter.

Although this is the most general propagator, there are other propagators that satisfy the conditions to this problem. For example, assuming the detection screen integrates the probability over the complete duration of the experiment, the interference is a stationary process and the propagator [101] is the solution to the Helmholtz equation [102]

$$K\left(\vec{r}; \vec{r}\,'\right) = \frac{k}{2\pi i}\frac{1}{\left|\vec{r} - \vec{r}\,'\right|} e^{i\,k\left|\vec{r} - \vec{r}\,'\right|}, \tag{3.5}$$

for source with wavenumber k, as I will comment in the last Section of this Chapter.

First I derive the classical paths using the general free particle Feynman propagator (Eq. (3.3)), then I expand the analysis to the nonclassical paths, showing the contribution from the different trajectories looping around both slits before reaching the detection screen.

3.1.1 Classical paths

The classical paths incorporate all possible paths connecting the source and the detection screen, whenever a single slit, A or B, is open as depicted in Fig. 2.2b and c. The wave function resulting from the summation of all paths that go through slit A only is

$$\psi_A(x,t) = \iint_{-\infty}^{+\infty} K(x,t;x',t')T(x'+d/2)K(x',t';x_0,0)\psi_0(x_0)\,dx'\,dx_0 \ , \qquad (3.6)$$

where

$$T\,(x) = \exp\left[\frac{-\,(x)^2}{2\beta^2}\right] . \qquad (3.7)$$

In Eq. (3.6), $K(x',t';x_0,0)$ is the free propagator from the source to the slit plane, and $K(x,t;x',t')$ is the free propagator from the slit plane to the detection screen. $T(x')$ is the slit transmission function, which we take to be a Gaussian function of slit-width β [97, 103, 104]. Performing the integral, yields the following form,

$$\psi_A\,(x) = \Gamma_c \exp\left[\mathrm{c}_2 x^2 + \mathrm{c}_1 x + \mathrm{c}_0\right] , \qquad (3.8)$$

where the explicit expression for the constants (Γ_c, c_2, c_1, c_0) are given in Appendix A.1. The wave function resulting from the summation of classical paths that go through slit B is similarly calculated,

$$\begin{aligned}\psi_B(x,t) &= \iint_{-\infty}^{+\infty} K(x,t;x',t')T(x'-d/2)K(x',t';x_0,0)\psi_0(x_0)\,dx'\,dx_0 \\ &= \Gamma_c \exp\left[\mathrm{c}_2 x^2 - \mathrm{c}_1 x + \mathrm{c}_0\right] .\end{aligned}$$

In the next subsection, we will use this formalism to calculate the nonclassical path that goes through two slits before reaching the detection screen.

3.1.2 Nonclassical paths

There are an infinite number of nonclassical paths that enter both slits. Nonclassical paths that loop through both slits were considered in the literature [46, 97]. An example of such a path is depicted by the green dotted line in Fig. 3.1: the

particle enters slit A, then slit B, then slit A again, before traveling to the detection screen. We will focus on nonclassical paths entering each slit only once, first considered in [101]. An example of such path is depicted by the red solid line in Fig. 3.1: the particle enters slit A, then slit B, then travels to the detection screen. The wave function resulting from the summation of such nonclassical paths is

$$\begin{aligned}\psi_{AB}(x,t,\tau) = &\iiint_{-\infty}^{+\infty} K(x,\tilde{t}+\tau;x_2',\tilde{t})T(x_2'-\frac{d}{2})K(x_2',t+\epsilon;x_1',t) \\ &\qquad T(x_1'+\frac{d}{2})K(x_1',t;x_0,0)\psi_0(x_0)\,dx_1'\,dx_2'\,dx_0 \\ &= \Gamma_{nc}\exp\left[\mathrm{c}_2'\mathrm{x}^2+\mathrm{c}_1'x+\mathrm{c}_0'\right]\,,\end{aligned} \tag{3.9}$$

with constants given in Appendix A.1. Similarly, the wave function resulting from the summation of nonclassical paths that go through slit B then A is

$$\begin{aligned}\psi_{BA}(x,t,\tau) = &\iiint_{-\infty}^{+\infty} K(x,\tilde{t}+\tau;x_2',\tilde{t})T(x_2'+\frac{d}{2})K(x_2',t+\epsilon;x_1',t) \\ &\qquad T(x_1'-\frac{d}{2})K(x_1',t;x_0,0)\psi_0(x_0)\,dx_1'\,dx_2'\,dx_0 \\ &= \Gamma_{nc}\exp\left[\mathrm{c}_2'\mathrm{x}^2-\mathrm{c}_1'x+\mathrm{c}_0'\right]\,,\end{aligned} \tag{3.10}$$

The difference between $\psi_{AB}(x,t,\tau)$ and $\psi_{BA}(x,t,\tau)$ lies in the sign of $\pm c_1'$.

Using the same formalism, other nonclassical paths can also be calculated. For example, the looped trajectory (green dotted line in Fig. 3.1), requires an additional transmission through the slits, and therefore has the wave function

$$\begin{aligned}\psi_{BAB}(x,t,\tau) = \int_{x_1',x_2',x_3',x_0} &K(x,t'+\tau;x_3',t')T(x_3'-\frac{d}{2})K(x_3',\tilde{t}+\epsilon;x_2',\tilde{t})T(x_2'+\frac{d}{2}) \\ &K(x_2',t+\epsilon;x_1',t)T(x_1'-\frac{d}{2})K(x_1',t;x_0,0)\psi_0(x_0)\,.\end{aligned} \tag{3.11}$$

In general, each additional slit transmission attenuates the wave function. I computed the attenuation factor a, normalizing the wavefunction after each slit transmission for every path considered, and used the constants defined in appendix A.1. The wavefunction scales as $|\psi(x,t)|^2 \approx |a^m\psi_0(x,0)|^2$, where $a \approx 0.1$ is the attenuation factor and m is the number of times the atom traverses a slit. For classical paths $m=1$, minimal nonclassical paths $m=2$, and single looped paths $m=3$. The probability of detecting minimal nonclassical paths is 1% and loop paths is 0.01%, relative to the classical paths. In the next section, I will use these results to show how one may indeed detect minimal nonclassical paths.

3.2 Measuring nonclassical paths in the double-slit experiment

Our setup consists of placing a cavity into each of the slits as depicted in Fig. 3.2. The source is a two-level Rydberg atom with ground and excited states $|g\rangle$ or $|e\rangle$. The transition frequency between the two states is resonant with the cavity mode Ω. The initial configuration is such that the atom is in the excited state, and there is one photon in each of the cavities,

$$|\psi_0\rangle = |e\rangle|1\rangle_A|1\rangle_B \ . \tag{3.12}$$

The speed of the atom is tuned so that the interaction time with the cavity is

$$\tau = \frac{\pi}{\sqrt{n+1}\Omega} \ , \tag{3.13}$$

where $n+1$ is the number of excitation in the cavity. This interaction time affects a π pulse on the atom [105]. Here we are interested in the case where $n = 1$, to ensure that the transition between $|e\rangle|1\rangle_i$ and $|g\rangle|2\rangle_i$ $(i = A, B)$ occurs with unit probability. Therefore our interaction time is set to $\tau = \frac{\pi}{\sqrt{2}\Omega}$.

3.2.1 Atom-cavity interaction

Initially the atom is in the excited state and there is a single photon in each cavity. If the atom follows the classical path, it enters a single cavity once; in this case the transition $|e\rangle|1\rangle_i \rightarrow |g\rangle|2\rangle_i$ will occur. If the atom follows the nonclassical path it will enter both cavities. Upon leaving the first cavity the atom emits a photon $|e\rangle|1\rangle_i \rightarrow |g\rangle|2\rangle_i$, and on leaving the second cavity, the atom absorbs a photon $|g\rangle|1\rangle_{i'} \rightarrow |e\rangle|0\rangle_{i'}$ $(i \neq i')$. As such, the system state just before the detection screen is

$$\begin{aligned} |\psi\rangle = &\frac{1}{\sqrt{N_2}} \left[|g\rangle \left(|2\rangle_A|1\rangle_B|\psi_A\rangle + |1\rangle_A|2\rangle_B|\psi_B\rangle\right) + \right. \\ &\left. + |e\rangle \left(|2\rangle_A|0\rangle_B|\psi_{AB}\rangle + |0\rangle_A|2\rangle_B|\psi_{BA}\rangle\right)\right] , \end{aligned} \tag{3.14}$$

where N_i is the overall normalization factor, which in general will be dependent on the number of slits (i) present. The first term represents the state of the system when the atom's (classical) path traverses though slit-A only: here the atom emits a photon into cavity A. Similarly, the second term represents the state of the system when the atom's (classical) path traverses through slit-B only. The third term represents the state of the system when the atom's (nonclassical) path traverses first through slit-A then slit-B: here the atom emits a photon into cavity A and absorbs a photon in cavity B. Similarly, the fourth term represents the

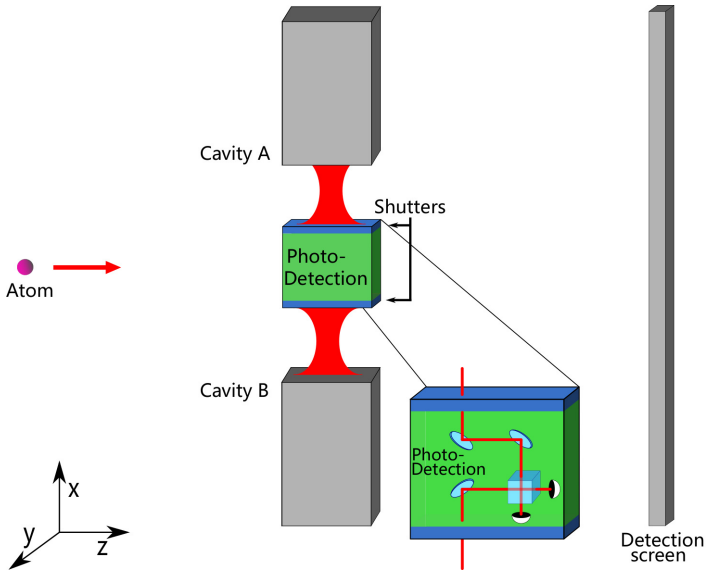

Figure 3.2: *Scheme of atom and double-slit with photonic cavities in each slit. The blue and green box in between the double slit contains the shutters and photodetection scheme. The inset (bottom right) shows a magnified view of the process of photodetection, it describes in detail one possible implementation to detect the cavity photons. In this example, with the opening of the shutters, the cavity photons go through a 50:50 beam splitter before its detection.*

state of the system when the atom's (nonclassical) path traverses first through slit-B then slit-A.

Defining the following symmetric and anti-symmetric basis states,

$$|\psi_c^{\pm}\rangle = \frac{1}{\sqrt{2}}\left(|\psi_A\rangle \pm |\psi_B\rangle\right) \ , \tag{3.15}$$

$$|\psi_{nc}^{\pm}\rangle = \frac{1}{\sqrt{2}}\left(|\psi_{AB}\rangle \pm |\psi_{BA}\rangle\right) \ , \tag{3.16}$$

$$|\mu^{\pm}\rangle = \frac{1}{\sqrt{2}}\left(|2\rangle_A|1\rangle_B \pm |1\rangle_A|2\rangle_B\right) \ , \tag{3.17}$$

$$|\nu^{\pm}\rangle = \frac{1}{\sqrt{2}}\left(|2\rangle_A|0\rangle_B \pm |0\rangle_A|2\rangle_B\right) \ , \tag{3.18}$$

we can rewrite the state of the system before the detection screen [Eq. (3.14)] as

$$\begin{aligned} |\psi_f'\rangle = &\frac{1}{\sqrt{N_2}}\left[|g\rangle\left(|\psi_c^+\rangle|\mu^+\rangle + |\psi_c^-\rangle|\mu^-\rangle\right) + \right. \\ &\left. + |e\rangle\left(|\psi_{nc}^+\rangle|\nu^+\rangle + |\psi_{nc}^-\rangle|\nu^-\rangle\right)\right] . \end{aligned} \tag{3.19}$$

Equation (3.19) shows that by measuring the state of the atom, we can isolate the classical and nonclassical paths. Keeping count only when an excited atom is detected gives the probability distribution of the nonclassical paths:

$$\begin{aligned} P_e(x) = &\frac{1}{N_2}\left(|\psi_{nc}^+(x)|^2 + |\psi_{nc}^-(x)|^2\right) \\ = &\frac{1}{N_2}\left(|\psi_{AB}(x)|^2 + |\psi_{BA}(x)|^2\right) \ . \end{aligned} \tag{3.20}$$

Conversely, keeping count only when a grounded atom is detected, gives the probability distribution of the classical paths,

$$\begin{aligned} P_g(x) = &\frac{1}{N_2}\left(|\psi_c^+(x)|^2 + |\psi_c^-(x)|^2\right) \\ = &\frac{1}{N_2}\left(|\psi_A(x)|^2 + |\psi_B(x)|^2\right) \ . \end{aligned} \tag{3.21}$$

From Eqs. (3.20) and (3.21) and the wave functions calculated in previous section, we plot in Fig. 3.3 the nonclassical path probability distribution, normalized to the central maximum of the double-slit classical probability distribution, i.e. $P_e(x)/P_g(0)$.

Figure 3.3 shows the spatial distribution of the atoms in the detection screen; the nonclassical paths account for about 1% of the classical paths detection events. The absence of an interference pattern is the result of the distinguishable

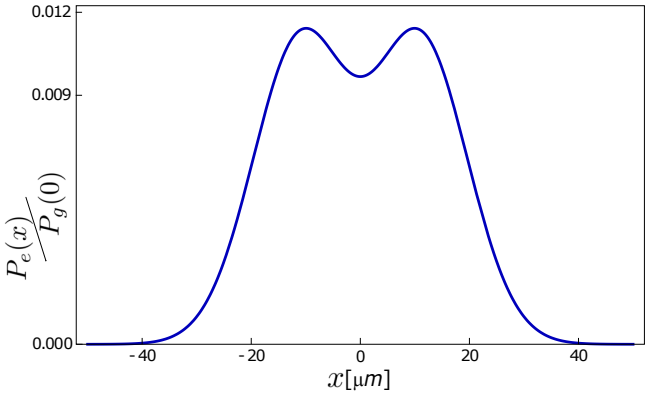

Figure 3.3: *Probability of detecting nonclassical paths normalized by the classical paths. The parameters are defined in Appendix A.1.*

cavity Fock states that mark the atoms paths. Specifically, from Eq. (3.14) we see that the presence of two photons in cavity A, reveals that the atom went through slit A then B; conversely, when two photons are in cavity B, the atom went through slit B then A. In the next subsection we will show how this which-way information can be erased by introducing shutters and intracavity photodetectors. We will show that erasing this information will retrieve the interference pattern between nonclassical paths.

3.2.2 Erasing which-way information with cavity photodetection

An interesting feature of the atom-cavity implementation of the which-way detectors is that one can partially erase the which-way information and restore coherent interference, even after the atom has been detected. To partially erase the which-way information, we add a beam splitter and photodetectors between the two cavities (Fig. 3.2). Shutters are positioned in each cavity. When the shutters are open, the photons are mixed in a beam splitter device and photodetectors are placed at each output port; the photodetectors act as a reservoir and in the limit of long detection time, all photons present in the cavities are absorbed. This procedure allows to mix the photons from both cavities loosing the which-slit information, retrieving interference.

The shutters opening and photon detection occurs after the passage of each single atom. The statistics is obtained in the limit of infinite repetitions of this procedure. The beam splitter action on the intracavity photons, corresponds to

the following transformation of the A, B input modes:

$$\hat{a}_{\pm}^{\dagger}|0\rangle = \frac{(a_A \pm a_B)^{\dagger}}{\sqrt{2}}|0\rangle, \tag{3.22}$$

for example in the new basis, the state $|\nu^{-}\rangle = |1\rangle_{+}|1\rangle_{-}$. At each output port $+, -$, there is a photodetector, we shall refer to their probability distributions as P^{+} and P^{-}, respectively.

I modeled the detection statistics, following the Markovian view of photon absorption [106]. This strategy predicts photon counts of one, two and three photons in a time interval. The density matrix time evolution contains the detection probabilities at each photon absorption. At time $t = 0$ the density matrix is:

$$\rho(0) := |\psi_f'\rangle\langle\psi_f'| \ , \tag{3.23}$$

$|\psi_f'\rangle$ was defined in Eq. (3.19), with photon number in the $+/-$ basis [Eq. (3.22)]. The procedure to calculate $\rho(t)$ and the probability distributions are described in Appendix A.2 [107]. Here we will discuss the most relevant results, and analyze the probabilities in the limits of zero and infinite detection time.

At zero interaction time, no photons are absorbed, the statistics recover the results of Sec. 3.2.1. Moreover, for infinite detection time, all photons are absorbed and the number of photons in the cavities is conditioned to the atomic state, as we can see in Eq. (3.19). If the atom is detected in the ground state, there are three photons in the cavities, whereas if detected in the excited state, only two photons are in the cavities.

The probability of measuring the atom in the excited state with two photon counts in the same output photodetector, $P_e^{(kk)}$, or one photon in each output, $P_e^{(kj)}$, $k = +/-, j = +/-$ with $k \neq j$. In the regime of long detection time one gets

$$P_e^{(kk/kj)}(x) = \frac{1}{2N_2}\left(|\psi_{nc}^{(+/-)}(x)|^2\right). \tag{3.24}$$

It represents the retrieval of interference, between nonclassical paths AB and BA, due to detection of the cavity photons. This is implemented keeping count of the excited atoms, *only* when two photons trigger the same ($P^{(kk)}$) or different ($P^{(kj)}$) detectors.

Similarly, the probability of measuring the atom in the ground state and detecting three photons in the same detector, $P^{(kkk)}$, and two photons in one detector and one in the other, $P^{(kjk)}$ (over all permutations of kjk), in the regime of long detection time is:

$$P_g^{(kkk)}(x) = \frac{1}{N_2}\left(\frac{3}{4}\right)\left(|\psi_c^{(k)}(x)|^2\right), \tag{3.25}$$

$$P_g^{(kjk)}(x) = \frac{1}{N_2}\left(\frac{1}{12}\right)\left(|\psi_c^{(j)}(x)|^2\right). \tag{3.26}$$

The total probability of atoms in the ground state is given by:

$$P_g(x) = \sum_{\substack{k,j=+,-\\ k\neq j}} P_g^{(kkk)}(x) + 3P_g^{(kjk)}(x). \tag{3.27}$$

This result recovers Eq. (3.20), as expected. This is implemented keeping count of the grounded atoms, *only* when three photons trigger the same or different detectors, respectively.

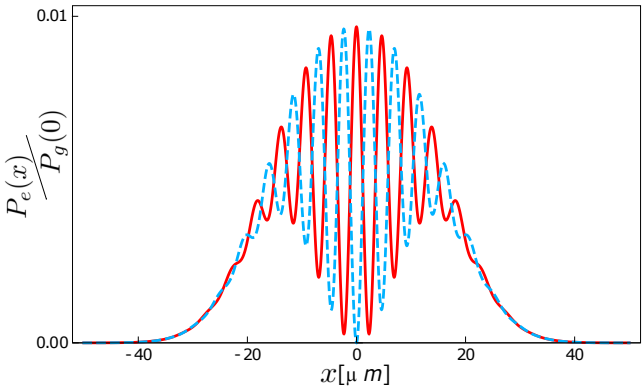

Figure 3.4: *Probability of detecting nonclassical paths in comparison with the classical paths. The red solid curve illustrates the nonclassical paths fringes pattern, it is the total probability of interfering and measuring in a single detector the intra-cavity photons after measuring the atom in the excited state,* $P_e^{(kk)}(x)$. *The blue dashed curve, shows the anti-fringes pattern, it indicates probability distribution of interfering and measuring the photons in both detectors,* $P_e^{(kj)}(x)$

The magnitude of the nonclassical paths is presented in Fig. 3.4, the interference pattern is recovered, due to the opening of the shutters, which allows for the photons interference and detection. The red solid curve illustrates the nonclassical paths fringes pattern, showing it contributes with up to 1% of the total probability distribution; it is the total probability of interfering and measuring in a single detector the intra-cavity photons, $P_e^{(kk)}(x)$. The blue dashed curve, shows the anti-fringes pattern, it indicates probability distribution of interfering and measuring one photon in each detector, $P_e^{(kj)}(x)$.

Intriguingly, at the time at which the atoms were detected, the decision to open or keep closed the photodetector shutter actually had not been made.

Whether the atom exhibited coherent interference or not, was determined the time after its detection; we therefore have a manifestation of the delayed-choice quantum erasure experiment. Only when the which-way information is erased by opening the shutters, the atomic inference pattern is retrieved.

In the next subsection, we will discuss how cavities which-way detectors can be used to implement the Quach's parameter and test the Born rule.

3.2.3 The Quach parameter as a Born rule test

The Quach parameter tests the Born rule in the double slit using which-way detectors [1]. By taking into account the non-classical paths, it allows to perform a more precise measurement of the Born rule. It involves comparing probability distributions with and without which-way detectors

$$I_{AB} \equiv \mathcal{P}_{AB} - \mathcal{P}_{D_A} - \mathcal{P}_{D_B} - \mathcal{P}_{D_{AB}} + 2\mathcal{P}_{D_A D_B} \ , \tag{3.28}$$

where,

$$\mathcal{P}_{D_A}(x) = |\psi_A(x) + \psi_{AB}(x) + \psi_{BA}(x)|^2 + |\psi_B(x)|^2 \ , \tag{3.29}$$

$$\mathcal{P}_{D_B}(x) = |\psi_A(x)|^2 + |\psi_{AB}(x) + \psi_{BA}(x) + \psi_B(x)|^2 \ , \tag{3.30}$$

$$\mathcal{P}_{D_A D_B}(x) = |\psi_A(x)|^2 + |\psi_B(x)|^2 + |\psi_{AB}(x) + \psi_{BA}(x)|^2 \ , \tag{3.31}$$

$$\mathcal{P}_{D_{AB}}(x) = |\psi_A(x) + \psi_B(x)|^2 + |\psi_{AB}(x) + \psi_{BA}(x)|^2 \ . \tag{3.32}$$

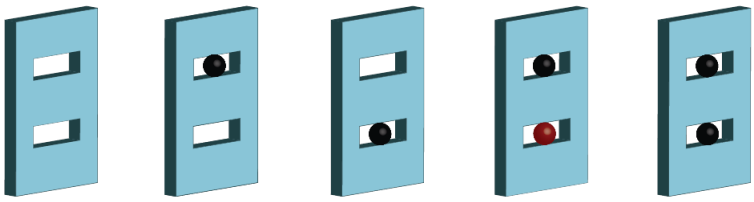

Figure 3.5: *A schematic of the different configurations of which-way detectors to test the Quach parameter in the double-slit. Figure from [1].*

$\mathcal{P}_{D_A}(x)$ corresponds to a which-way detector in slit A, it is represented in 3.5b (3.29). The which-way detector in slit A has no distinction between the non-classical paths

$\mathcal{P}_{D_A}(x)$ and $\mathcal{P}_{D_B}(x)$ are the probability distributions when there is a which-way detector in slit A or B, respectively. $\mathcal{P}_{D_A D_B}(x)$ and $\mathcal{P}_{D_{AB}}(x)$ are the probability distributions of distinguishable and indistinguishable which-way detectors

in both slits, respectively. Distinguishable which-way detectors identify whether a particle went through slit A or B, indistinguishable which-way detectors knows that a particle went through the slits, but does not know which one. $\psi_{AB}(x)$ consists of Feynman paths that go through slit A first then slit B, and vice versa for $\psi_{BA}(x)$.

Quach's parameter has the advantage that $I_{AB} = 0$ if the Born rule is not violated, even in the presence of high-order paths and it applies to the double-slit setup. However, up until now Quach's parameter has only been a formal construct. Here we propose how Quach's parameter could be implemented using atom-cavities.

To implement the Quach parameter we follow the reasoning of Sec. 3.2 using the cavity as which-way detectors. We also write the parameter in terms of the normalized probability distributions (P_i), as this is what is actually measured:

$$I_{AB} = N_0 P_{AB} - N_1 \left(P_{D_A} + P_{D_B}\right) - N_2 \left(P_{D_{AB}} - 2P_{D_A D_B}\right) \ , \tag{3.33}$$

where N_i are normalization factors that satisfy $\int_{-\infty}^{\infty} \frac{1}{N_0} \mathcal{P}_{AB}(x)dx = \frac{1}{N_1} \int_{-\infty}^{\infty} \mathcal{P}_{D_A}(x)dx = \frac{1}{N_2} \int_{-\infty}^{\infty} \mathcal{P}_{D_{AB}}(x) = 1$.

To calculate each of these probabilities a different initial setup is required, as it is summarized in Table 3.1.

Probability distribution	Setup: Atom	Slit A	Slit B
P_{AB}	$\|g\rangle$	-	-
P_{D_A}		$\|1\rangle$	-
P_{D_B}		-	$\|1\rangle$
$P_{D_{AB}}$	$\|e\rangle$	$\|1\rangle$	$\|1\rangle$
$P_{D_A D_B}$			

Table 3.1: *Initial setup of the system, to obtain the respective probability distributions. The atom is either intialized in the ground $|g\rangle$ or excited $|e\rangle$ state. $|1\rangle$ represent a slit-cavity initialized with a single photon. The sign - represents a empty slit, i.e. without cavity.*

To implement the single-slit which-way detector, a cavity is placed in one slit only, leaving the remaining slit empty. To obtain, for example, $P_{D_A}(x)$ the setup has a cavity in slit A only, and the atom is initially in the ground state

$|g\rangle|1\rangle_A|0\rangle_B$. The evolved state of the system before the detection screen is

$$\begin{aligned}|\psi_{D_A}\rangle =&\frac{1}{\sqrt{N_1}}\left[|g\rangle|1\rangle_A|0\rangle_B|\psi_B\rangle+\right.\\&\left.+|e\rangle|0\rangle_A|0\rangle_B(|\psi_A\rangle+|\psi_{AB}\rangle+|\psi_{BA}\rangle)\right].\end{aligned}\tag{3.34}$$

The first term represents the state of the system when the atom traverses slit B *only*. The second term represents the state of the system whenever the atom traversed slit A. In all three cases, the atom absorbed the intracavity photon and transitioned to the excited atomic state $|e\rangle$.

Tracing out the cavity states ($\mathrm{Tr_c}$) and projecting on to the position basis, one can retrieve $P_{D_A}(x)$:

$$\begin{aligned}P_{D_A}(x) =&\langle x|\mathrm{Tr_c}\left[(|e\rangle\langle e|+|g\rangle\langle g|)\,|\psi_{D_A}\rangle\langle\psi_{D_A}|\right]|x\rangle\\=&\frac{1}{N_1}\left(|\psi_A(x)+\psi_{AB}(x)+\psi_{BA}(x)|^2+|\psi_B(x)|^2\right).\end{aligned}\tag{3.35}$$

In other words, selecting the atoms in the ground and excited state at the detection screen, allows one to obtain the probability of adding a which-way detector in a single slit $P_{D_A}(x)$. $P_{D_B}(x)$ is similarly obtained with the initial state $|g\rangle|0\rangle_A|1\rangle_B$. We plot $P_{D_A}(x)$ in Fig. 3.6(c) using the wave functions analytically calculated in Sec. 3.1. $P_{D_B}(x)$ has a similar pattern.

To obtain $P_{D_{AB}}(x)$ and $P_{D_AD_B}(x)$ we use the analysis developed in Sec. 3.2, i.e. the system is initially $|e\rangle|1\rangle_A|1\rangle_B$, with the cavity photodetector shutters open. The probability distribution of distinguishable which-way detectors, $P_{D_AD_B}(x)$ is

$$\begin{aligned}P_{D_AD_B}(x) =&P_g+2P_e^{(kk)}\\=&\frac{1}{N_2}\left(|\psi_A(x)|^2+|\psi_B(x)|^2+\right.\\&\left.+|\psi_{AB}(x)+\psi_{BA}(x)|^2\right)\ .\end{aligned}\tag{3.36}$$

where $P_e^{(kk)}$ is defined in Eq. (3.24); the factor of 2 accounts for $k=+$, and $k=-$. P_g is the sum defined in Eq. (3.27).

By counting all atoms in the ground state, while the ones in the excited state are kept only when two photons trigger the same cavity photodetector, the grounded atoms at each x-position give the first term, and the excited atoms give the second term of the probability distribution. I plot $P_{D_AD_B}(x)$ in Fig. 3.6(b).

To calculate the probability distribution of indistinguishable which-way detectors, $P_{D_{AB}}(x)$, described in detail in Appendix A.2, based on which one can define the required detection strategy. The implementation requires us to keep count of the atoms in the ground state whenever three photons arrive in detector

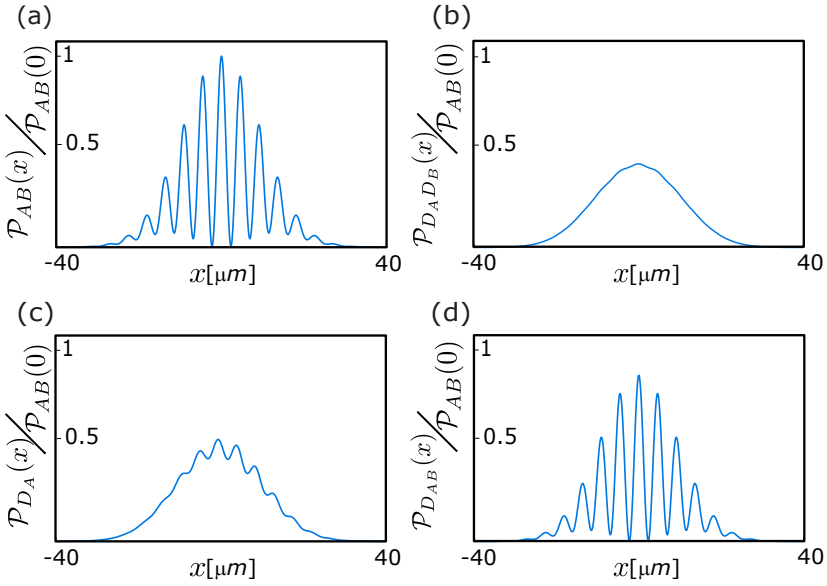

Figure 3.6: *Probability distributions for the different configurations of which-way detectors: a) absence of which-way detectors. b) distinguishable which-way detectors in both slits. c) which-way detector in slit A. d) indistinguishable which-way detectors in both slits. Summing the probabilities according to Quach's parameter, one obtains exactly zero.*

"P^+", and when one photon arrives in "P^+" and two in "P^-". It also requires one to keep count of atoms in the excited state only when two photons reach the same detector,

$$\begin{aligned} P_{D_{AB}}(x) =& P_g^{+++} + P_g^{+--} + P_g^{-+-} + P_g^{--+} + P_e^{++} + P_e^{--} \\ =& \frac{1}{N_2}\left(\frac{3}{4}|\psi_c^+(x)|^2 + 3\left(\frac{1}{12}|\psi_c^+(x)|^2\right) + |\psi_{nc}^+(x)|^2\right) \\ =& \frac{1}{N_2}\left(|\psi_A(x) + \psi_B(x)|^2 + |\psi_{AB}(x) + \psi_{BA}(x)|^2\right). \end{aligned} \tag{3.37}$$

I plot $P_{D_{AB}}(x)$ in Fig. 3.6(d).

With all these probabilities in hand, I calculate $I_{AB}(x) = 0$. Obviously, as our theoretical description assumed the Born rule, this result is expected. However, I propose a detailed practical description to test Quach's parameter. In an experiment, $I_{AB}(x) \neq 0$, would implicate a Born-rule violation.

3.3 Disconecting the Sorkin parameter from the nonclassical paths

The Sorkin parameter is a mathematical construct to quantify non-pairwise interference using the triple-slit setup [99], this result was later applied to experimental settings [47, 85, 108]. It involves associating $\mathcal{I}_j$ in Eq. 3.38 with the number of slits open, claiming a non-zero $\mathcal{I}_3$ would indicate a violation of the Born rule.

$$\mathcal{S}_3 = \mathcal{I}_{ABC} - \mathcal{I}_{AB} - \mathcal{I}_{AC} - \mathcal{I}_{BC} + \mathcal{I}_A + \mathcal{I}_B + \mathcal{I}_C \tag{3.38}$$

where $\mathcal{I}_{ABC}$ is the outcome for 3 slits open, $\mathcal{I}_{AB}$ is the outcome for two slits A and B open, and so on.

In an experimental setting each slit configuration is associated with a respective sum of wavefunctions, for example, $\mathcal{I}_{ABC} = |\Psi_A + \Psi_B + \Psi_C|^2$ and $\mathcal{I}_{AB} = |\Psi_A + \Psi_B|^2$, results in $\mathcal{S}_3 = 0$.

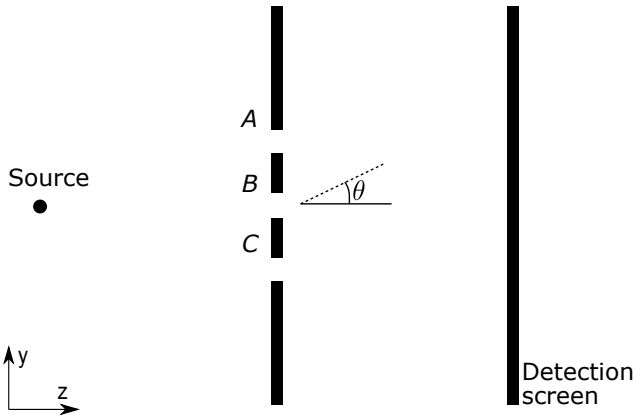

Figure 3.7: *A schematic of the triple-slit experiment.*

Despite the extensive use of the Sorkin parameter in the last decade experimentally and theoretically, it still lacks a consistent explanation of its non-zero value. There has been attempts on associating it with the Born rule violation and to the difference in boundary conditions (for the settings of slits open and closed) using FDTD simulation considerations [87, 88], although, it only showed there is more than just on reason for its non-zero value [109]. There have also been attempts to connect the Sorking parameter to the nonclassical paths using Feynman path integral formulation [101]. In this Section I show the Sorkin

parameter is not a good measure of the nonclassical paths because it can yield non-zero value even in the absence of nonclassical paths.

In the work of Sawant *et al.* [101] the authors describe a triple-slit experiment to measure the Sorking parameter. The values of $\mathcal{I}_j$ in Eq. 3.38 are then associated with probability distributions in the detection screen when $1, 2$ and 3 slits are open. In their work the probability distributions are equal to the Feynman path integral propagator defined in Eq. (3.5) squared as

$$\epsilon = |K_{ABC}|^2 - |K_{AB}|^2 - |K_{AC}|^2 - |K_{BC}|^2 + |K_A|^2 + |K_B|^2 + |K_C|^2 \quad (3.39)$$

As each propagator correspond to different experimental settings, a fair comparison should include adequate normalization factors. Therefore, I proposed the following

$$\begin{aligned}\epsilon' = N_{ABC}|K_{ABC}|^2 - N_{AB}|K_{AB}|^2 - N_{AC}|K_{AC}|^2 - N_{BC}|K_{BC}|^2 \\ + N_A|K_A|^2 + N_B|K_B|^2 + N_C|K_C|^2 \ ,\end{aligned} \quad (3.40)$$

where N_i are the normalisation constants that need to satisfy the physical constraints of probability conservation,

$$N_\beta \int_{-\infty}^{\infty} |K_\beta(y)|^2 dy = 2N_\alpha \int_{-\infty}^{\infty} |K_\alpha(y)|^2 dy \ . \quad (3.41)$$

$$N_\gamma \int_{-\infty}^{\infty} |K_\gamma(y)|^2 dy = 3N_\alpha \int_{-\infty}^{\infty} |K_\alpha(y)|^2 dy \quad (3.42)$$

where $\alpha = \{A, B, C\}$, $\beta = \{AB, AC, BC\}$, and $\gamma = ABC$. In other words, the probability of a photon passing through a plane with n slits, should be n/m times the probability of a photon passing through a plane with m slits.

For example, consider the scenario without non-classical paths i.e. $K_{nc} = 0$. Substituting the definitions in Ref. [101], into Eq. (3.42) and (3.41), shows that $N_\alpha = N_\beta = N_\gamma$ when different single-slit wavefunctions K_α satisfy the orthogonality condition,

$$\int_{-\infty}^{\infty} K_{\alpha *} K_{\alpha'} dy = 0 \ . \quad (3.43)$$

In this case $\epsilon = \epsilon' = 0$ when there are no non-classical paths. However, K_α's are only orthogonal in the regime $kd \sin\theta = 0$, for wavenumber k and slit separation d. This makes $\epsilon' \neq 0$ for $kd \sin\theta \neq 0$, therefore a non-zero ϵ can be a sign of the non-orthogonality of the single-slit wavefunction instead of the nonclassical paths.

Chapter 4

Discrimination and estimation of incoherent sources

In this chapter I analyse methods to improve the spatial resolution of two incoherent point sources whose separation is well below the diffraction limit dictated by classical optics. I discuss the issues of estimation of the sources position as well as discriminating if there is one source or two with half the power, very close to each other. The results in the literature show these tasks can be achieved decomposing the incoming radiation into orthogonal and transverse modes. Such a demultiplexing procedure, however, must be perfectly calibrated to the transverse profile of the incoming light as any misalignment in the mode decomposition effectively restores the diffraction limit for small source separations.
Here I show by how much can one mitigate such misalignment effect in the measurement which, after being imperfectly demultiplexed due to inevitable misalignment, may still be partially corrected by linearly transforming the relevant dominating transverse modes. I consider two complementary tasks: the estimation of the separation between the two sources and the discrimination between one and two incoherent point sources. I show that, although one cannot fully restore superresolution even for perfectly known misalignment, its negative impact on the ultimate sensitivity can be significantly reduced. In the case of estimation I determine analytically the exact relation between the minimal resolvable separation as a function of misalignment. Whereas for discrimination, I determine analytically the relation between misalignment and the probability of error, as well as numerically determine how the latter scales in the limit of long interrogation times.

Even further, I study alternative collective measurement strategies capable of superresolving two sources separation, without previous knowledge of their transverse profile exact centroid. This measurement exploits the symmetry under exchange of N bosonic systems and is equivalent to determining the spectrum of their density operator.

This chapter is based on:
Discrimination and estimation of incoherent sources under misalignment
J. O. de Almeida, J. Kołodyński, C. Hirche, M. Lewenstein, and M. Skotiniotis, *Physical Review A* **103**, 022406 (2021) and Collective super-resolving measurements for mixed bosonic states
J. O. de Almeida, M. Lewenstein, and M. Skotiniotis, *arXiv*, **2110.00986** (2021)

In 1879, Lord Rayleigh proposed a criterion for resolving incoherent sources [4]: two sources very close to each other cannot be resolved, as their image gets blurred due to diffraction effects. Whereas Rayleigh's criteria is a rough idea on resolution limits, and more precise measurements could in principle give a better resolution [110], it resulted in being a limitation in optics for over a century, even called sometimes Rayleigh's curse.

More precise measurements in optics require a thorough analysis of the signal-to-noise ratio, which can be incorporated using statistical inference methods [111]. These methods allow defining resolution as parameter estimation [112] or hypothesis testing [113]. A complete estimate requires knowledge of the source's separation, centroid, and relative intensity, whereas, the discrimination requires distinction between two hypothesis, two-vs-one source.

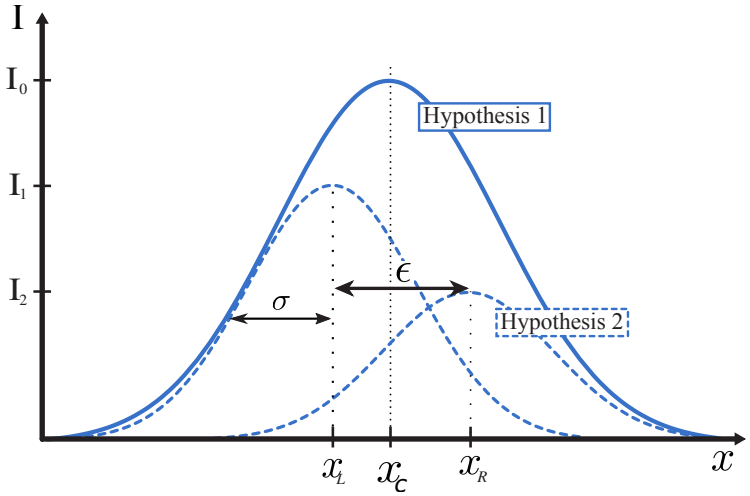

Figure 4.1: *Illustration of the problems in question; the one-vs-two hypothesis testing, one source (I_0) with the power of two sources (I_1 and I_2), where $I_0 = I_1+I_2$ and the two sources multi-parameter estimation, of intensity q and position of maxima (x_R and x_L), or centroid (x_C) and separation (ϵ).*

All these issues have been posed by Helstrom since 1969 [9, 114] with Rayleigh's criteria as a limitation. It was not until 1994, the advances in quantum optics [115] allowed breakthroughs of resolution measurements in microscopy. By using stimulated emission and fluorescence of typical fluorophores, it was possible to perform superresolution, i.e. to resolve two light sources with a separation smaller than dictated by Rayleigh's criterion.

These techniques allowed significant new advances in microscopy, as a bet-

ter resolution of single molecules and proteins [116–118]. However, despite the immense utility of these methods for superresolution in microscopy, there is no analogous technique in astronomy and remote sensing.

In the attempt to find an optimal measurement strategy to perform superresolution of any two incoherent sources with equal brightness, M. Tsang *et. al.* [2] formulated this problem using methods for estimating the centroid and separation parameters. In this work, they derive a fundamental limit to the precision in estimating the two sources separation, in the form of the quantum Cramér-Rao bound [69, 77].

The measurement strategy proposed in [2] involves performing spatial mode demultiplexing (SPADE), and it can always yield a measure of the separation even bellow the diffraction limit, under the assumption the measurement device is placed exactly at the centroid position, x_c. Although, the exact two source localization is a multiparameter estimation problem, it requires perfect knowledge of the distribution centroid.

The only way to perform simultaneous estimation of the centroid and separation is making use of collective measurements [72]. This requires a quantum memory with long enough coherence time and ability to manipulate and interfere the photons stored. A proof-of-principle of this collective measurement was demonstrated in [30]. In this experiment, the spatial distribution of two incoherent sources was simulated in a single photon; interfering two copies of this photon in a Hong-Ou-Mandel experiment [119], which corresponds to perform a two copies ($N = 2$) collective measurement, allows for simultaneous estimation of both the centroid and the separation. Moreover, an estimate of the separation between two incoherent point sources was obtained from the bunching and coincidence counts—due to Hong-Ou-Mandel interference—of two such bosons incident on a 50-50 beamsplitter; this measurement is equivalent to the so-called SWAP test [120].

In this chapter I follow this approach and generalize the experimental realization [30] to propose an alternative, collective measurement strategy for estimating the separation between two incoherent point sources, it provides provide more precise estimates of the overlap as compared to the SWAP test [121, 122]. Here I will discuss its super-resolving power. However, its implementation requires the storage of the collective state of N bosons in a quantum memory [123–127].

When Helstrom [9] first addressed the problem of discriminating one-vs-two incoherent point sources using tools from hypothesis testing, not only the measurement strategy derived lacked a physical realisation, but also required knowledge of the two sources separation.

It was not until 2016, Krovi *et al.* [128] derived the optimal quantum mechanical measurement that achieves the quantum Chernoff bound for the case where

the separation of the two point sources is known and discussed possible implementations. Shortly after, [19] showed the measurement strategies derived for parameter estimation [2], achieves the quantum Chernoff bound for one-vs-two sources of *arbitrary* separation. However, just like in the estimation case, the centre of the single source, as well as the centroid of the two source hypothesis, must be perfectly aligned with the demultiplexing measurements.

In this chapter I will address both problems of estimation and discrimination of incoherent light sources. In the first part I define the assumptions and parameters used, in the second part I discuss discrimination and estimation of light sources for a measurement device misaligned with the centroid of the distribution and in the last part I discuss collective measurements for estimating the separation between two incoherent sources.

4.1 Quantum description of light sources

In the ideal case, one can assume the sources are quasimonochromatic and are in the paraxial wave approximation, in one dimension. For a thermal source, it is standard to assume [129, 130] within a coherence time interval the average number of photons $\chi \ll 1$. Therefore, the density operator for the light fields in the image plane can be written as:

$$\sigma^{(i)} = (1-\chi)\sigma_0 + \chi\rho_1^{(i)} + \mathcal{O}(\chi^2). \tag{4.1}$$

where $\sigma_0 = |\text{vac}\rangle\langle\text{vac}|$ is the zero-photon state, ρ_1 is a one-photon state (the superscript index $i = 1, 2$ is labeling the case where the photon is due to one or two point sources) and $\mathcal{O}(\chi^2)$ denotes the order of χ^2.

The state of a single photon emanating from a single source in the far-field regime cetered around x_0 is

$$\rho_1^{(1)} \approx |\Psi_0\rangle\langle\Psi_0|, \tag{4.2}$$

the subscript denotes the position around which the wavefunction is centered

$$|\Psi_0\rangle = \int_{-\infty}^{\infty} dx \Psi(x - x_0)|x\rangle, \tag{4.3}$$

where the spatial distribution $\Psi(x - x_i)$ is the Fourier transform of the detection aperture, derived in Sec. 2.1.1[1] .

[1] $\Psi(x - x_i)$ is equivalent to $U(\phi)$ in Eq. (2.2), as in the far field regime, ϕ is small and $\sin(\phi) \approx \phi$.

Whereas a photon coming from two incoherent point sources with relative intensities q and $1-q$, centered around x_L and x_R can be approximated as [2]

$$\rho_1^{(2)} \approx q|\Psi_L\rangle\langle\Psi_L| + (1-q)|\Psi_R\rangle\langle\Psi_R|, \tag{4.4}$$

with $|\Psi_{L(R)}\rangle = \int_{-\infty}^{\infty} dx \Psi(x - x_{L(R)})|x\rangle$. The creation of a photon in a position in the image plane is $|x\rangle = a^\dagger(x)|0\rangle$, where $a^\dagger(x)$, $a(x)$ are the creation and annihilation operators satisfying the commutation relation $[a(x), a^\dagger(y)] = \delta(x - y)$ [131]. Which in the special case of sources with equal intensities is

$$\rho_1^{(2)}\Big|_{q=\frac{1}{2}} \approx \frac{1}{2}|\Psi_L\rangle\langle\Psi_L| + \frac{1}{2}|\Psi_R\rangle\langle\Psi_R|, \tag{4.5}$$

Parametrizing the problem as a function of the separation and centroid of the distribution. The intensity centroid is

$$x_c = q\, x_L + (1-q)x_R, \tag{4.6}$$

which reduces to $x_c = \frac{x_R + x_L}{2}$ for sources with equal intensity, and separation

$$d = \frac{|x_R - x_L|}{2} = \frac{\epsilon}{2} \tag{4.7}$$

If the two sources separation is larger than the standard deviation of the Gaussian distribution ($d \gg \sigma$), all the parameters can be effectively estimated, and the distinction between two-vs-one hypothesis is easily done with direct imaging [132]. However, I will focus in the regime where their separation is very small ($d \ll \sigma$)–Fig.4.1– and the two sources cannot be resolved due to Rayleigh's diffraction limit [4].

4.2 Discrimination and estimation of incoherent sources under misalignment

The advances in quantum information and quantum metrology [69, 72] allowed [2] to look for applications in astronomy. The new techniques proposed [22], and the rapid theoretical and experimental advances show possible enhancement in the resolution beyond the limits of direct imaging. In [2], the sources were assumed to have equal brightness, and the centroid and separation are the two parameters to be estimated.

To demonstrate superresolution is possible, Tsang [2] used the quantum statistical inference, and specifically the quantum Cramer-Rao bound, to derive a lower bound on the error in estimating the two sources separation. This result

shows the ultimate bound in estimating the separation is inversely proportional to a constant, in contrast to the case of direct imaging where the error scales with the separation.

In order to compute the Cramér-Rao bound, the initial density matrix (Eq. (4.5)) must be diagonalized in an orthonormal basis spanning the space of $\rho_1^{(2)}$ and its derivative. Hence, the resulting optimal measurement strategy will be in the same basis, and this is the intuition behind the proposal of spatial-mode demultiplexing (SPADE).

In optics when dealing with Gaussian states, the spatial modes can be interpreted as the energy eigenstates of the quantum mechanical harmonic oscillator, i.e., the Hermite-Gauss (HG) modes:

$$|\Phi_n(x_D)\rangle = \frac{1}{\sqrt{2^n\, n!}} \frac{1}{\sqrt[4]{2\pi\,\sigma^2}} \times \int_{-\infty}^{\infty} e^{-\frac{(x-x_D)^2}{4\sigma^2}} H_n\left(\frac{x-x_D}{\sqrt{2}\sigma}\right) |x\rangle \,\mathrm{d}x, \qquad (4.8)$$

where $H_n(x)$ are the Hermite polynomials, and x_D is the position around which the spatial modes are centered, or in case of performing the SPADE measurement, the detector's position.

To implement SPADE there are two main challenges, the first is to detect and distinguish the different HG modes and the second is to know exactly the position of the centroid. To solve the first issue, Tsang proposed an alternative measurement, binary SPADE (B-SPADE), in which only the zeroth mode ($n = 0$ in Eq. (4.8)) should be distinguished from the higher order modes ($n > 0$) and it can be implemented with single and multi-mode optical fibers, and it can resolve the two point sources separation no matter how close they are on the image plane so long as the detector is at the centroid position.

Moreover, even if the centroid is known sufficiently well, the detector still must be perfectly aligned with the measurement device for the spatial mode demultiplex, i.e., setting $x_D = x_c$.A proposal on how best to accomplish this using a finite number of observations was proposed by Grace *et al.* [133]. There the authors show how to combine direct imaging and SPADE techniques, in a two-stage procedure; the former uses part of the incoming radiation to adjust the exact position of the latter via a servo feedback mechanism in order to gradually reduce the *misalignment*, $\delta := x_c - x_D$, which is a priori not known. One therefore sacrifices a portion of the samples in order to estimate the centroid (its precision scales $\propto N^{-1/2}$) either directly, or by more resource efficient adaptive strategies [133].

Similarly to the estimation problem, in discriminating one-vs-two sources, the B-SPADE measurement achieves the quantum Chernoff bound [19] if the detector is aligned with the centre both hypothesis, i.e. $x_D = x_c$. In this work, I analyse the scenario where the detector is misaligned with the centre of the single source,

as well as with the centroid of the two source hypothesis, $x_D \neq x_c$.

In this part of the thesis I assume the measurement device is misaligned with the centroid of the distribution and determine analytically the theoretical limits imposed by such misalignment in both estimation and discrimination tasks. To do so I assume the detector is a mode demultiplexer and any postprocessing of the detected radiation is allowed. Specifically, these results show how the complete knowledge of the value of the misalignment allow to propose a linear-optical signal postprocessing, as well as its effects on estimation precision and on the minimal resolvable distance. To do so I make use of an approximation of the state of the incoming radiation known as the qubit model [134], which I now review.

4.2.1 The qubit model

The qubit model is an approximation of the point spread function (PSF) in presence of misalignment [134]. It can be understood as performing the projective measurement of Eq. (4.8) about some reference position $x_D \neq x_i$ for $i \in (0, R, L)$. Assuming that this misalignment is small, i.e., $x_D \approx x_i$, and Taylor expanding the probability amplitudes of each source, $\Psi(x - x_i)$, $i \in \{1, 2\}$, about x_D as follows:

$$\begin{aligned} |\Psi(x_i)\rangle &\approx \int_{-\infty}^{\infty} \mathrm{d}x\, \Psi(x - x_D)\, |x\rangle + (x_i - x_D) \int_{-\infty}^{\infty} \mathrm{d}x\, \frac{\mathrm{d}\Psi(x - x_i)}{\mathrm{d}x_i}\bigg|_{x_i = x_D} |x\rangle \\ &=: |0\rangle - (x_i - x_D)\sqrt{\mathcal{N}}|1\rangle, \end{aligned} \tag{4.9}$$

and identify a qubit subspace with $|0\rangle := |\Psi(x_D)\rangle$ and

$$|1\rangle := \frac{-1}{\sqrt{\mathcal{N}}} \int_{-\infty}^{\infty} \mathrm{d}x\, \frac{\mathrm{d}\Psi(x - x_i)}{\mathrm{d}x_i}\bigg|_{x_i = x_D} |x\rangle \tag{4.10}$$

an orthonormal basis. Here, $\mathcal{N}$ is an appropriate normalisation factor which for the Gaussian and Sinc PSFs reads

$$\mathcal{N}_{\mathrm{G}} = \frac{1}{4\sigma^2}, \qquad \mathcal{N}_{\mathrm{S}} = \frac{\pi^2}{3\sigma^2}, \tag{4.11}$$

respectively.

The state of the incoming radiation can now be described, to a very good approximation, by the following qubit density operators, for one and two sources, respectively:

$$\begin{aligned} \rho^{(1)} &\approx \frac{1}{1 + (\sigma\theta)^2\mathcal{N}} \begin{pmatrix} 1 & -\sigma\theta\sqrt{\mathcal{N}} \\ -\sigma\theta\sqrt{\mathcal{N}} & (\sigma\theta)^2\mathcal{N} \end{pmatrix} \\ \rho^{(2)} &\approx \frac{1}{1 + \sigma^2(\theta^2 + \eta^2)\mathcal{N}} \begin{pmatrix} 1 & -\sigma\theta\sqrt{\mathcal{N}} \\ -\sigma\theta\sqrt{\mathcal{N}} & \sigma^2(\theta^2 + \eta^2)\mathcal{N} \end{pmatrix}, \end{aligned} \tag{4.12}$$

where I now introduced dimensionless parameters for *misalignment* and *separation*:

$$\theta := \frac{\delta}{\sigma} = \frac{x_c - x_D}{\sigma} \qquad \text{and} \qquad \eta := \frac{d}{\sigma} = \frac{\epsilon}{2\sigma}, \tag{4.13}$$

respectively. The qubit model allows us to visualise the effects of misalignment on a given PSF in terms of the Bloch representation of qubit density matrices, i.e.,

$$\rho := \frac{\mathbb{1} + \mathbf{r}\cdot\boldsymbol{\sigma}}{2}, \tag{4.14}$$

where $\mathbf{r} \in \mathcal{R}_3$, has elements $\mathrm{r}_i = \mathrm{Tr}(\sigma_i\rho)$ and $\boldsymbol{\sigma} := (\sigma_1, \sigma_2, \sigma_3)^T$ is the vector of Pauli matrices σ_i. For the Gaussian and Sinc PSFs the corresponding Bloch vectors read

$$\begin{aligned}
\mathbf{r}_{\mathrm{G}}^{(1)} &= \frac{1}{1+\frac{\theta^2}{4}}\begin{pmatrix} -\theta \\ 0 \\ 1-\frac{\theta^2}{4}\end{pmatrix}, \ \mathbf{r}_{\mathrm{G}}^{(2)} = \frac{1}{1+\frac{\theta^2+\eta^2}{4}}\begin{pmatrix} -\theta \\ 0 \\ 1-\frac{\theta^2+\eta^2}{4}\end{pmatrix} \\
\mathbf{r}_{\mathrm{S}}^{(1)} &\approx \frac{1}{1+\frac{\theta^2}{3}}\begin{pmatrix} -\frac{2\theta}{\sqrt{3}} \\ 0 \\ 1-\frac{\theta^2}{3}\end{pmatrix}, \ \mathbf{r}_{\mathrm{S}}^{(2)} \approx \frac{1}{1+\frac{\theta^2+\eta^2}{3}}\begin{pmatrix} -\frac{2\theta}{\sqrt{3}} \\ 0 \\ 1-\frac{\theta^2+\eta^2}{3}\end{pmatrix},
\end{aligned} \tag{4.15}$$

respectively. Using the approximations

$$\begin{aligned}
\frac{1}{1+x^2} &\approx 1 - x^2 \\
1 - \frac{(\theta^2+\eta^2)}{2} &\approx (1-\frac{\theta^2}{2})(1-\frac{\eta^2}{2}) \approx \cos\theta\left(1-\frac{\eta^2}{2}\right),
\end{aligned} \tag{4.16}$$

and keeping terms up to second order, $\mathcal{O}(\theta^i\eta^j)$ with $i+j=2$, the Bloch vectors in Eq. (4.15) can be further approximated by

$$\begin{aligned}
\mathbf{r}_{\mathrm{G}}^{(1)} &\approx \begin{pmatrix} -\sin\theta \\ 0 \\ \cos\theta\end{pmatrix}, \quad \mathbf{r}_{\mathrm{G}}^{(2)} \approx \left(1-\frac{\eta^2}{2}\right)\begin{pmatrix} -\sin\theta \\ 0 \\ \cos\theta\end{pmatrix} \\
\mathbf{r}_{\mathrm{S}}^{(1)} &\approx \begin{pmatrix} -\sin\frac{2\theta}{\sqrt{3}} \\ 0 \\ \cos\frac{2\theta}{\sqrt{3}}\end{pmatrix}, \quad \mathbf{r}_{\mathrm{S}}^{(2)} \approx \left(1-\frac{\eta^2}{2}\right)\begin{pmatrix} -\sin\frac{2\theta}{\sqrt{3}} \\ 0 \\ \cos\frac{2\theta}{\sqrt{3}}\end{pmatrix}.
\end{aligned} \tag{4.17}$$

Consequently the misalignment, θ, can be understood as an infinitesimal rotation about the y-axis in the Bloch-sphere picture, whereas the separation, η, between the centres of the two incoherent point sources affects the purity of the state [134].

Here the aim is to use the qubit model to study the effects of misalignment, both in the estimation of the separation between two point sources, as well as in the task of discriminating between the single and two source hypotheses. I will begin first discriminating one-vs-two light sources.

4.2.2 Discrimination one-vs-two incoherent sources under misalignment

In this section I use the qubit model to find the optimal measurement strategy to discriminate between one-vs-two sources, for the case when the two sources have equal intensities.

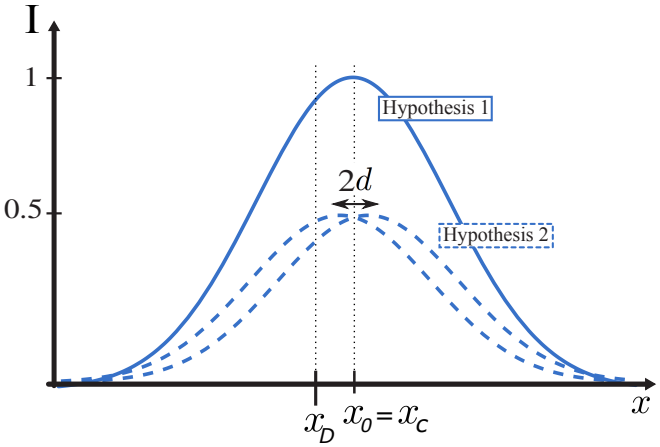

Figure 4.2: *Hypothesis testing scenario, one-vs-two sources hypothesis. One source with twice the power centered in x_0, or two sources very close together with separation $2d$ and centroid x_c. Discrimination task for a two sources centroid aligned with the one source center $x_c = x_0$, and a detector misaligned with this position $x_D \neq x_c = x_0$.*

I compare the optimal measurement given by the qubit model, with the results of Lu *et. al.* [19], where they analyze the behavior of the Chernoff exponent of B-SPADE, direct imaging and the Quantum Chernoff bound, in the asymptotic limit of infinite repetitions.

The optimal measurement strategy for distinguishing the two hypothesis according to the qubit model, is the Helstrom measurement. The density matrix in the qubit representation, using Eq. (4.17) is

$$\begin{aligned}\rho_{\mathrm{G}}^{(1)} &\approx \frac{1}{4}\begin{pmatrix} 2+2\cos\theta_0 & -2\sin\theta_0 \\ -2\sin\theta_0 & 2-2\cos\theta_0 \end{pmatrix} \\ \rho_{\mathrm{G}}^{(2)} &\approx \frac{1}{4}\begin{pmatrix} 2-(\eta^2-2)\cos\theta_c & (\eta^2-2)\sin\theta_c \\ (\eta^2-2)\sin\theta_c & 2+(\eta^2-2)\cos\theta_c \end{pmatrix},\end{aligned} \tag{4.18}$$

where $\theta_0 = \frac{x_0 - x_D}{\sigma}$ is the misalignment relative to the center of a single source, and $\theta_{\mathrm{c}} = \frac{x_c - x_D}{\sigma}$ is the misalignment relative to the centroid, x_c, of the two

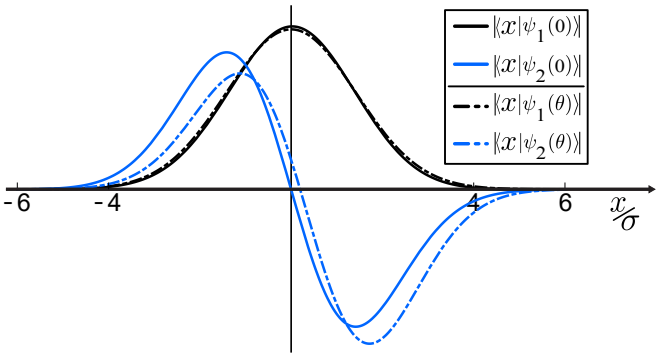

Figure 4.3: *Spatial representation of the ROTADE operators for aligned (solid line, $\theta = 0$) and misaligned (dot- dashed, $\theta = 0.4$) measurement. The plots are given for $\frac{d}{\sigma} = 0.25$. $|\psi_\alpha(\theta)\rangle$ is defined in Eq.* (4.21).

sources, and η is defined as in Eq. (4.13).

The Helstrom matrix (according to Eq. (2.42)) is therefore

$$\Gamma = \frac{1}{4}\begin{pmatrix} -\cos\theta_0 - \frac{1}{2}\cos\theta_c(\eta^2-2) & \sin\theta_0 + \frac{1}{2}\sin\theta_c(\eta^2-2) \\ \sin\theta_0 + \frac{1}{2}\sin\theta_c(\eta^2-2) & \cos\theta_0 + \frac{1}{2}\cos\theta_c(\eta^2-2) \end{pmatrix}, \tag{4.19}$$

In principle, the center of a single source need not coincide with the centroid of two sources, nor with the position of the demultiplexing measurement, $x_0 \neq x_c \neq x_D \quad (\theta_0 \neq \theta_c)$. Nonetheless, hereafter I shall restrict my analysis to the case where only the demultiplexing measurements are misaligned, hence I define:

$$\theta := \theta_0 = \theta_c. \tag{4.20}$$

In this regime, the eigenbasis of the Helstrom measurement is independent of separation and I shall refer to this measurement as the *rotated mode demultiplexer* (ROTADE), i.e. the detection scheme depicted schematically in Fig. 4.3 with the rotation $R(\delta)$ adequately adjusted to $\delta = \theta\sigma$.

$$\begin{aligned} |\psi_1(\theta)\rangle &= \sin\frac{\theta}{2}|0\rangle + \cos\frac{\theta}{2}|1\rangle \\ |\psi_2(\theta)\rangle &= -\cos\frac{\theta}{2}|0\rangle + \sin\frac{\theta}{2}|1\rangle, \end{aligned} \tag{4.21}$$

this measurement is a θ rotation on the zero-th and first modes of the harmonic oscillator.

For a detector aligned with the centroid position $\theta = 0$, ROTADE is only the projection onto the zeroth and first HG modes. I call this measurement

as SPADE01, in order to distinguish it from B-SPADE which projects only on the zeroth mode. I remark that all measurement strategies reach the quantum bound for zero misalignment. The main advantages of SPADE01 for aligned measurement device are: it is independent of the two-sources separation, the need to count photons only in the first two HG modes (photons coupling to higher modes correspond to no-clicks and are insignificant to the measurement statistics), and the unambiguous two-source discrimination whenever a photon is detected in the first HG mode.

The error probability can be obtained writing the measurement strategy projector in the spatial representation, and computing the overlap with the initial state $\rho^{(i)}$, this procedure is explained in the Appendix B.1.

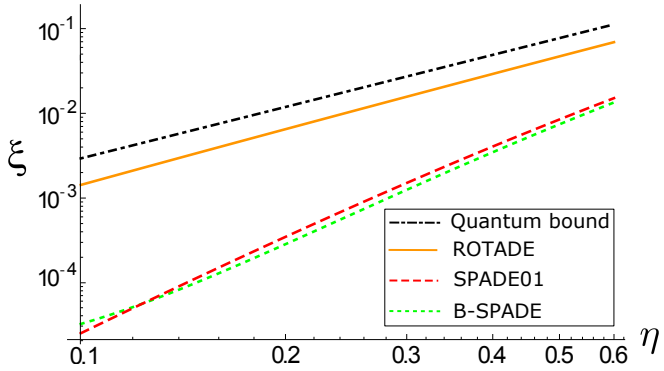

Figure 4.4: *Numerical optimisation of the Chernoff exponent under misalignment as a function of the separation in* $\log - \log$ *plot, for* $x_D = 0.4$ *and* $\sigma = 1$.

Table 4.1 shows how the error probability scales as a function of the misalignment for the first non-trivial order of the Taylor expansion around $\theta = 0$. Notice that for ROTADE, the $type - 1$ error, responsible for the unambiguous determination of the two-source hypothesis, is four orders of magnitude smaller compared to that of SPADE01 and B-SPADE. Hence in the single-shot scenario ROTADE significantly outperforms both these measurements.

The Chernoff exponent of the SPADE01 measurement under misalignment behaves similarly to that of B-SPADE, the asymptotic results of all measurement strategies under misalignment as function of separation are represented in Fig. 4.4. However, in contrast with the aligned scenario, for $\theta \neq 0$ the probability of detecting photons into higher HG modes is non-negligible, and corresponds to the no-click probability. This probability represents the intrinsic error of the qubit model and it increases with misalignment (for details see Appendix B.4).

Fig. 4.5 presents a numerical optimisation for the Chernoff exponent as a func-

Measurement	$p(f(y) = H^{(2)}\|H^{(1)})$	$p(f(y) = H^{(1)}\|H^{(2)})$
ROTADE	$\frac{\theta^6}{576\sigma^6}$	$\exp\left(-\frac{d^2}{4\sigma^2}\right)\left(1-\frac{d^2\theta^2}{16\sigma^4}\right)$
SPADE01	$\frac{\theta^2}{4\sigma^2}$	$\exp\left(-\frac{d^2}{4\sigma^2}\right)\left(1+\frac{(d^2-2\sigma^2)\theta^2}{8\sigma^4}\right)$
B-SPADE	$\frac{d^2\theta^2\operatorname{csch}\left(\frac{d^2}{4\sigma^2}\right)}{16\sigma^4}$	$\exp\left(-\frac{d^2}{4\sigma^2}\right)\left(1+\frac{(d^2-2\sigma^2)\theta^2}{8\sigma^4}\right)$

Table 4.1: *Taylor expansion to the first non-trivial order in θ for the type -1 (second column) and type -2 (third column) error probabilities for ROTADE, SPADE01 and B-SPADE.*

tion of the misalignment. For all $\theta > 0$ ROTADE outperforms both SPADE01 and B-SPADE, which is to be expected as ROTADE includes the knowledge on the amount of misalignment. Nonetheless, for *exactly* $\theta = 0$ all the corresponding Chernoff exponents coincide with the quantum bound, what manifests their discontinuity as $\theta \to 0_+$.

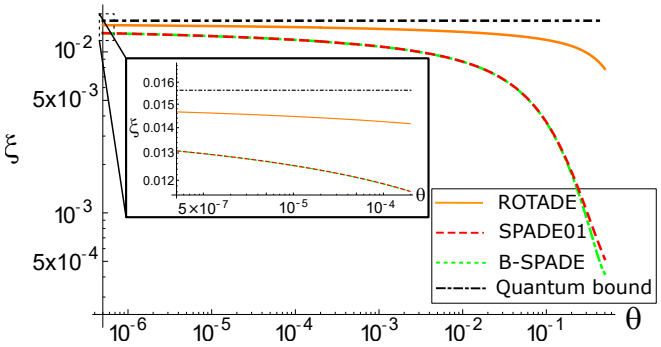

Figure 4.5: *Numerical determination of the Chernoff exponent as a function of the misalignment, for separation $\eta = 0.25$ between a pair of sources with $\sigma = 1$. The inset shows how the Chernoff exponent varies for the three relevant measurement strategies for $\theta \approx 0$.*

4.2.3 Separation estimation of two incoherent sources under misalignment

In this section I analyze the optimal measurement strategy to estimate the two sources separation, in the case they have equal intensities. The optimal measurement is equal to the Helstrom measurement derived for one-vs-two sources

discrimination, ROTADE.

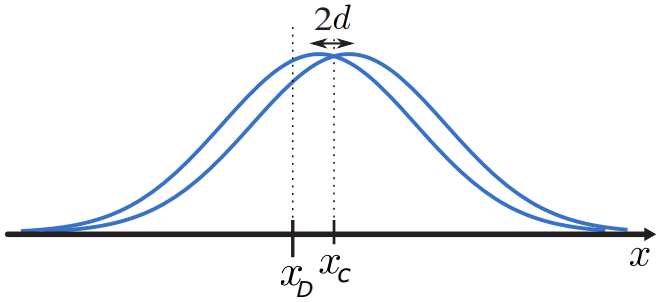

Figure 4.6: *Separation estimation* $2d$ *of two incoherent sources with equal intensities, with centroid* x_c*, misaligned with the detector device* x_D*.*

Assuming the separation between the incoherent sources to be small—as assured in the super-resolution regime—I use the qubit model in order to construct the optimal measurement for separation estimation. The optimal measurement for the Gaussian PSF is in the basis of the eigenvectors of $\rho_{\mathrm{G}}^{(2)}$ (Eq. (4.18)). These eigenvectors are the same as in the Helstrom measurement presented in Eq. (4.21), with eigenvalues

$$\begin{aligned}\mu_1(\eta) =& \frac{\eta^2}{4} \\ \mu_2(\eta) =& 1-\mu_1(\eta)\end{aligned} \tag{4.22}$$

Using Eq. (2.31) the corresponding SLD operators are, in the eigenbasis of ROTADE:

$$\mathcal{L}_\theta = \left(1-\frac{\eta^2}{2}\right)\sigma_x, \qquad \mathcal{L}_\eta = \begin{pmatrix} \frac{2}{\eta} & 0 \\ 0 & \frac{2\eta}{\eta^2-4} \end{pmatrix}. \tag{4.23}$$

Observe that $[\mathcal{L}_\theta, \mathcal{L}_\eta] \neq 0$, meaning that the optimal measurements for each of these parameters are incompatible. However, $\mathrm{Tr}\left(\rho_{\mathrm{G}}^{(2)}[\mathcal{L}_\theta, \mathcal{L}_\eta]\right) = 0$, which implies that there exists a possibly joint measurement on all N photons that saturates the quantum Cramér-Rao bound given by

$$\langle(\hat{\theta}-\theta, \hat{\eta}-\eta)^T(\hat{\theta}-\theta, \hat{\eta}-\eta)\rangle \geq \frac{1}{N}\begin{pmatrix} \frac{1}{1-\eta^2} & 0 \\ 0 & \frac{1}{1+\frac{\eta^2}{4}} \end{pmatrix}. \tag{4.24}$$

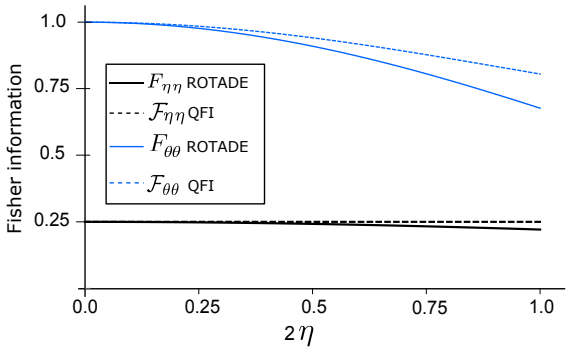

Figure 4.7: *Quantum Fisher information, $\frac{\mathcal{F}_\lambda}{N}$, attained in [2] (dashed lines) and classical Fisher information associated to the ROTADE measurement $\frac{F_\lambda}{N}$ (solid lines), for separation η (black) and misalignment θ (blue) parameters for perfect alignment $\theta = 0$, as a function of 2η. As the POVM Eq. (4.26) is derived based on the qubit model, it ceases to be optimal with increasing separation of the sources (here for $\eta \lesssim 0.1$).*

The eigenvectors of the SLD operators (Eq. (4.23)) are given by

$$|\theta_\pm\rangle = \frac{1}{\sqrt{2}}\left(\left(\sin\frac{\theta}{2} \pm \cos\frac{\theta}{2}\right)|0\rangle + \left(\sin\frac{\theta}{2} \mp \cos\frac{\theta}{2}\right)|1\rangle\right), \tag{4.25}$$

$$|\eta_\alpha\rangle = |\psi_\alpha(\theta)\rangle \quad \text{with} \quad \alpha \in \{1,2\}, \tag{4.26}$$

respectively. As $\mathcal{L}_\eta$ is a diagonal operator, the optimal measurement in Eq. (4.26) for estimating the re-scaled separation 2η between the two sources according to the qubit model is simply given by a projective measurement in the eigenbasis of Eq. (4.21).

In order to compare the quality of the ROTADE measurement, I use Eq. (4.9) to map the measurement operators into their position-based representation. The latter are shown in Fig. 4.3. One can then explicitly determine the probability distribution arising from these measurements and hence the corresponding Fisher information using Eq. (2.28). The results are shown in Fig. 4.7, where I compare the performance of ROTADE with the quantum Fisher information [2] for $\theta = 0$, i.e. without misalignment. Up to separations $\eta = \frac{d}{\sigma} \lesssim 0.5$ the Fisher information of ROTADE drops to $\approx 90\%$ of the optimal value. On the other hand, up to $\eta = \frac{d}{\sigma} \lesssim 0.1$ ROTADE maintains its optimality, emphasising that the qubit model approximates well the super-resolution problem in this regime. Hence, in the limit where the qubit model holds, counting photons only in the first two HG modes suffices to estimate the separation.

A simpler measurement that also achieves the quantum bound (Fig. 4.7) is

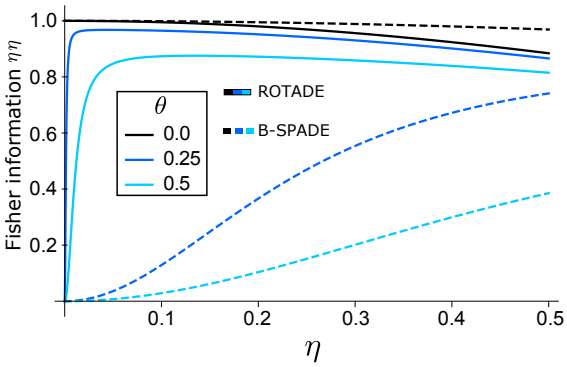

Figure 4.8: *B-SPADE Fisher information attained in [2] (dashed lines) and ROTADE Fisher information (solid lines) for separation estimation under misalignment, $\frac{F_{\eta\eta}}{N}$, as a function of the separation.*

B-SPADE [2]. This is a coarse grained version of SPADE where only photons in the fundamental HG mode of SPADE are counted, while lumping all other modes to produce a single photon-count outcome. As the probability of detecting the zeroth HG mode occurs regardless of the separation, d, B-SPADE is more experimentally friendly, but suffers in the same manner as SPADE from the misalignment problem. In Fig. 4.8 I compare the performance of ROTADE with B-SPADE in estimating the separation under a misalignment $\theta \leq 0.5$.

In order to capture the difference between the aforementioned measurements I compare the Taylor expansions of their corresponding Fisher information up to first non-trivial order, for small separation η. These are given by

$$\begin{aligned} F^{(\mathrm{R})}_{\boldsymbol{\eta\eta}}(\eta) &\approx \eta^2 C^{(R)}(\theta) \\ F^{(\mathrm{B})}_{\boldsymbol{\eta\eta}}(\eta) &\approx \eta^2 C^{(B)}(\theta), \end{aligned} \tag{4.27}$$

where $C^{(R)}(\theta)$, $C^{(B)}(\theta)$ are coefficients pertaining to the measurements themselves and depend only on the misalignment θ (they are independent of N and η). The behaviour of these coefficients governs the precise minimal resolvable distance for each measurement as I now explain.

The signal-to-noise-ratio $\eta/\Delta\eta$ can be expressed as

$$\eta\sqrt{N F^{(\#)}_{\boldsymbol{\eta\eta}}(\eta)} \geq 1, \tag{4.28}$$

where $\# \in (R, B)$. The minimal resolvable separation, $\eta^{(\#)}_{\mathrm{min}}(\theta)$, for each measurement is defined as that η in Eq. (4.28) for which equality holds. Using the

approximations of Eq. (4.27) one obtains

$$\eta_{\min}^{(\#)}(\theta) = \frac{1}{\sqrt[4]{NC^{(\#)}(\theta)}}. \tag{4.29}$$

Taylor expanding the functions $C^{(\#)}(\theta)^{-1}$ to first non-trivial order in θ one obtains

$$\begin{aligned} C^{(\mathrm{R})}(\theta)^{-1} &\approx \frac{\theta^6}{12^2} \\ C^{(\mathrm{B})}(\theta)^{-1} &\approx \theta^2. \end{aligned} \tag{4.30}$$

It follows that

$$\begin{aligned} \eta_{\min}^{(\mathrm{R})}(\theta) &\approx \frac{1}{\sqrt[4]{N}} \frac{\theta^{\frac{3}{2}}}{\sqrt{12}} \\ \eta_{\min}^{(\mathrm{B})}(\theta) &\approx \frac{\sqrt{\theta}}{\sqrt[4]{N}}, \end{aligned} \tag{4.31}$$

where $\eta_{\min}(\theta) \propto N^{-\frac{1}{4}}$ is a consequence of $F_{\boldsymbol{\eta\eta}} \propto \eta^2$ in Eq. (4.27). In contrast, observe that in the ideal case of no misalignment, for which $F_{\boldsymbol{\eta\eta}} \propto 1$, the minimal resolvable distance scales as $\eta_{\min}(0) \propto N^{-\frac{1}{2}}$.

The quadratic increase in the scaling of $\eta_{\min}$ for both ROTADE and B-SPADE due to misalignment mimicks closely the behaviour of cross-talk between the measurement modes addressed by Guessner *et al.* [135] in 2020. As our qubit approximation requires to monitor only the first two HG modes, and misalignment corresponds to a unitary rotation of the same two modes, it follows that this unitary rotation can be interpreted as the cross-talk matrix of [135]. As the cross-talk probability between the two modes is proportional to $\sin^2\theta \approx \theta^2$, $\eta_{\min}^{(B)}$ of Eq. (4.31) follows precisely the analytical model for uniform cross-talk of [135].

Our results show that super-resolution is impossible if the initial demultiplexing of the incoming radiation suffers any misalignment, even if the latter is known. Nevertheless, cross-modulation techniques between the two primary HG modes can help in significantly reducing the minimum resolvable distance. This procedure is presented in Fig. 4.9.

In Appendix B.2 I obtain the optimal measurement under misalignment for the Sinc PSF, as well as the minimum resolvable distance. Our results confirm the efficacy of the qubit model; for whatever PSF the first two modes are the most relevant ones in estimating the position of light sources with separation well below the diffraction limit.

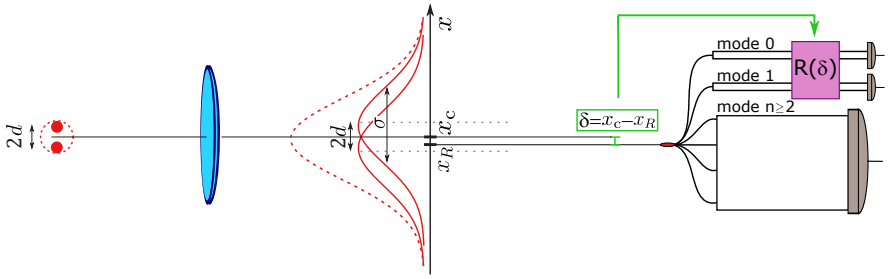

Figure 4.9: *Super-resolving the separation between incoherent sources under the misalignment of the demultiplexing apparatus. Two incoherent point-like sources of light are imaged with an optical system exhibiting a Gaussian point spread function of width σ in a way that their separation, $2d$, can be most accurately resolved. For this to be possible beyond the diffraction limit, a spatial mode demultiplexing technique is employed—which ideally allows the incoming light to be decomposed into orthogonal transverse modes, whose photon-occupation is subsequently measured. In this work, I study the ultimate limits on the resolution in the presence of misalignment of the imaging system, $\delta = x_{\rm c} - x_R \ll \sigma$, by applying appropriate linear optical post processing operations $R(\delta)$ is applied on the two dominant modes of the demultiplexing measurement.*

4.3 Collective measurements on mixed bosonic states

Even though superresolution had large advance both theoretically [14–25] as well experimentally [26–33] the current measurement strategies, e.g. SPADE [2] require exact knowledge of the centroid of the distribution. Any misalignment of the measurement device with respect to the centroid's position causes superresolution loss, although it is still better than performing direct imaging [34, 135]. If more parameters are to be inferred—such as separation, relative intensity, and centroid—it is known that no fixed measurement strategy, extracting information from *each* boson separately, can achieve the ultimate precision for all relevant parameters [18].

Here I propose an alternative, collective measurement strategy for estimating the separation between two incoherent point sources, with equal intensities or with known relative intensity without recourse to additional nuisance parameters. In this collective measurement strategy I analyze the symmetries under exchange of N bosonic systems [136, 137] possessing either finite or infinite dimensional degrees of freedom, and achieving linear scaling with sample size for

separation estimation between two sources of arbitrary brightness. For reasons that will become clear later, I shall refer to this measurement as the *spectrum measurement* [138].

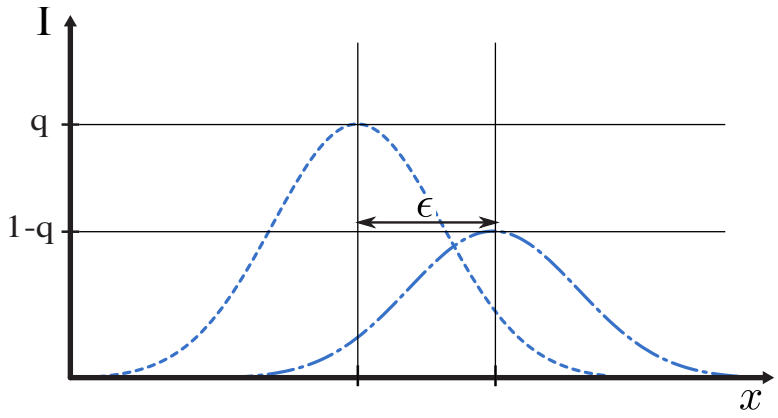

Figure 4.10: *Illustration of two sources with arbitrary intensities for separation estimation.*

In this section I first explain the collective measurement for estimating the separation in $N = 2$ copies of the two incoherent point sources based on the bunching and coincidence counts in the Hong-Ou-Mandel interference and I discuss how this measurement is equivalent to the SWAP test. Later I generalize this approach to the estimation in N copies of the two point sources state.

4.3.1 The SWAP test and the Hong-Ou-Mandel effect

In this section I describe the SWAP test whose measurement statistics provide an estimate of the overlap between two quantum states (Sec. 4.3.1) [120], as well as, the implementation of this measurement using the Hong-Ou-Mandel interference effect [119] and the application of this approach in super-resolution [30].

Let $|\Psi_1\rangle$, $|\Psi_2\rangle$ be two states and consider the task of estimating their overlap $|\langle\Psi_1|\Psi_2\rangle|$. One circuit that achieves this is shown in Fig. 4.11, where H is the Hadamard transformation

$$H|0\rangle = \frac{|0\rangle + |1\rangle}{\sqrt{2}} \qquad H|1\rangle = \frac{|0\rangle - |1\rangle}{\sqrt{2}} \tag{4.32}$$

and the unitary gate U corresponds to the controlled SWAP operator

$$U|\Psi_1\rangle|\Psi_2\rangle = |\Psi_2\rangle|\Psi_1\rangle. \tag{4.33}$$

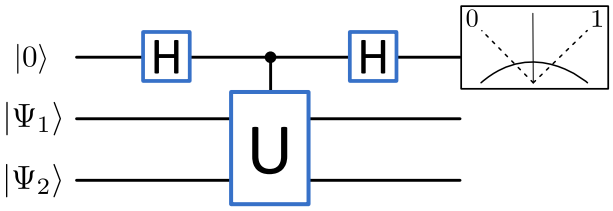

Figure 4.11: *Quantum circuit for the SWAP test used to estimate the overlap between states $|\Psi_1\rangle, |\Psi_2\rangle$. An ancillary system is used to provide the control for the controlled unitary gate U which implements the SWAP. Discarding the last two registers, a measurement in the computational basis of the ancilla has measurement statistics that directly depend on the overlap between the two states (see Eq. (4.35))*

.

The state of the circuit after the second Hadamard is given by

$$|\Omega\rangle = \frac{1}{\sqrt{2}}\left(|0\rangle \otimes \frac{|\Psi_1\rangle|\Psi_2\rangle + |\Psi_2\rangle|\Psi_1\rangle}{\sqrt{2}} + |1\rangle \otimes \frac{|\Psi_1\rangle|\Psi_2\rangle - |\Psi_2\rangle|\Psi_1\rangle}{\sqrt{2}}\right). \tag{4.34}$$

The SWAP test is performing a measurement on the symmetric and antisymmetric spaces of the bipartite state $|\Psi_1\rangle|\Psi_2\rangle$ such that the probabilities for each measurement outcome are given by

$$P_0 = \frac{1 + |\langle\Psi_1|\Psi_2\rangle|^2}{2} \qquad P_1 = \frac{1 - |\langle\Psi_1|\Psi_2\rangle|^2}{2}, \tag{4.35}$$

where P_0 is the probability of measuring state $|0\rangle$ after the circuit, and P_1 is the probability of detecting $|1\rangle$ after the circuit.

Hence, by repeating this measurement on several copies of the states $|\Psi_1\rangle$, $|\Psi_2\rangle$, one can extract an estimate of their overlap from the statistical distribution over the measurement outcomes.

Figure 4.12: *Image depicting the photons path in entering a 50:50 beam splitter simultaneously, as in the Houng-Ou-Mandel interference experiment.*

The SWAP test has been used as a measure of how much two states differ [139], the more similar the states, the larger is the symmetric probability or bunching in the beam splitter, and the more different two states are, the larger the antisymmetric probability or anti-bunching probability.

In a more fundamental approach, the SWAP test quantifies the overlap or interference between quantum states [140, 141], in the simple example of a product state $\rho = \rho_1 \otimes \rho_2 = |\Psi_1\rangle\langle\Psi_1| \otimes |\Psi_2\rangle\langle\Psi_2|$, the SWAP test of ρ is

$$\alpha = \mathrm{Tr}\left[U\rho_1 \otimes \rho_2\right] = \mathrm{Tr}\left[\rho_1.\rho_2\right] = |\left\langle\Psi_1|\Psi_2\right\rangle|^2, \tag{4.36}$$

this can be implemented in a circuit similar to Fig. 4.11 with input ρ_1 and ρ_2, giving the symmetric and antisymmetric probabilities as a function of the overlap

$$P_S = \frac{1+\alpha}{2} \qquad P_A = \frac{1-\alpha}{2}. \tag{4.37}$$

Applying the SWAP test in two copies of the two photon state defined in Eq. (4.5), i.e. $\rho_1 = \rho_2 = \rho_1^{(2)}$ gives the following overlap

$$\begin{aligned} \alpha = \mathrm{Tr}\left[U\rho_1^{(2)} \otimes \rho_1^{(2)}\right] = \mathrm{Tr}\left[\left(\rho_1^{(2)}\right)^2\right] &= 1 - 2q(1-q)\left(1 - |\left\langle\Psi_L|\Psi_R\right\rangle|^2\right), \\ \alpha\Big|_{q=\frac{1}{2}} &= \frac{1}{2}\left(1 + |\left\langle\Psi_L|\Psi_R\right\rangle|^2\right) \end{aligned} \tag{4.38}$$

The SWAP test was implemented for superresolution exploiting the Hong-Ou-Mandel effect [30]. There, the state of Eq. (4.5) is simulated in a single photon using the polarization degree of freedom with $q = 1/2$. Two such photons are sent through a perfectly balanced 50-50 beam splitter and are subsequently subjected to spatially resolving detectors at the output. The bunching and coincidence counts—which correspond to measuring the total angular momentum of the polarization degree of freedom of the two photons respectively—allow for superresolution of the separation ϵ, whereas the position of the photons in the detector allows for precise estimation of the centroid.

In the next section I discuss a generalization of the SWAP test to process N particles collectively. Such measurement strategies are known to outperform the SWAP test in overlap estimation [121, 122]. I now introduce this measurement, which relies on the concept of Schur-Weyl duality [142].

4.3.2 Spectrum Measurements

Consider then, the case of N bosons each prepared in rank-d state $\rho \in \mathcal{B}(\mathcal{H})$ [143], given by

$$\rho = \sum_{k=1}^{d} \lambda_k \, |\lambda_k\rangle\langle\lambda_k|. \tag{4.39}$$

where λ_k are the eigenvalues and $|\lambda_k\rangle$ the eigenvectors.

Without loss of generality the spectrum of ρ in non-increasing order so that $\boldsymbol{\lambda} \in [0,1]^d,\ \lambda_k \geq \lambda_{k+1}$. In this scenario, $d = 2$ but we can assume the general case of $d \geq 2$. Observe that $\rho^{\otimes N}$ is invariant under any permutation, $\sigma \in S_N$, of the N bosons, i.e., $[\rho^{\otimes N}, T_\sigma] = 0,\ \forall\, \sigma \in S_N$ where $T : S_N \to \mathbb{U}(\mathcal{H}^{\otimes N})$ is a homomorphism of the permutation group to a set of unitary operators on $\mathcal{H}^{\otimes N}$.

It follows that

$$\begin{aligned} \rho^{\otimes N} &= \frac{1}{N!} \sum_{\sigma \in S_N} T_\sigma\, \rho^{\otimes N}\, T_\sigma^\dagger \\ &:= \mathcal{G}_{S_N}[\rho^{\otimes N}], \end{aligned} \tag{4.40}$$

where I have defined the completely positive, trace-preserving map $\mathcal{G}_{S_N} : \mathcal{B}(\mathcal{H}^{\otimes N}) \to \mathcal{B}(\mathcal{H}^{\otimes N})$. Eq. (4.40) tells us that including permutation symmetry, the state of our N photons obtains a special form determined fully by the representation T of S_N.

Specifically, the Hilbert space associated to the relevant degrees of freedom of the N bosons, $\mathcal{H}^{\otimes N}$, carries two natural representations; that of S_N introduced above, and that of the special unitary group, $U^{\otimes N} : \mathrm{SU}(d) \to \mathbb{U}(\mathcal{H}^{\otimes N})$. Observe that the two representations commute, which is crucial, since then by Schur-Weyl duality [142] and Schur's lemmas [144], there exists a particular choice of orthonormal basis in which $\mathcal{H}^{\otimes N}$ assumes the block diagonal form

$$\mathcal{H}^{\otimes N} \cong \bigoplus_Y \mathcal{U}_Y \otimes \mathcal{P}_Y. \tag{4.41}$$

The set Y are known as *Young frames*; an arrangement of N boxes into at most d rows with the restriction that the number of boxes in any row cannot exceed those above it (see Fig. 4.13),

$$Y := \left\{ (Y_1, \ldots, Y_d) \;\middle|\; Y_1 \geq Y_2 \geq Y_3 \geq \ldots \geq Y_d,\ \sum_{k=1}^{d} Y_k = N \right\}. \tag{4.42}$$

The subspaces $\mathcal{U}_Y$, $\mathcal{P}_Y$ carry the irreducible representations $U^{(Y)} : \mathrm{SU}(d) \to \mathbb{U}(\mathcal{U}_Y)$ and $T^{(Y)} : S_N \to \mathbb{U}(\mathcal{P}_Y)$ of the special unitary and permutation groups respectively. The fact that both irreducible representations are labelled by the same Young frame is a consequence of the commutativity of the two representations. Particularly, $U^{\otimes N}$ and T decompose as

$$\begin{aligned} U_g^{\otimes N} &\cong \bigoplus_Y U_g^{(Y)} \otimes \mathbb{1}, \quad \forall\, g \in \mathrm{SU}(d) \\ T_\sigma &\cong \bigoplus_Y \mathbb{1} \otimes T_\sigma^{(Y)}, \quad \forall\, \sigma \in S_N. \end{aligned} \tag{4.43}$$

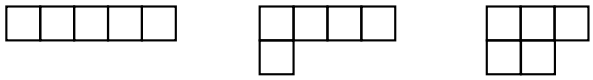

Y=(5,0) Y=(4,1) Y=(3,2)

$\hat{\lambda} = \begin{pmatrix} 1 \\ 0 \end{pmatrix}$ $\hat{\lambda} = \begin{pmatrix} 0.8 \\ 0.2 \end{pmatrix}$ $\hat{\lambda} = \begin{pmatrix} 0.6 \\ 0.4 \end{pmatrix}$

Figure 4.13: *The Young frames of partitioning* 5 *into at most two parts. The vectors* $\hat{\boldsymbol{\lambda}} \in (0,1)_2$; $\hat{\boldsymbol{\lambda}} = \frac{Y}{N}$ *are the corresponding estimates of the eigenvalues of* $\rho \in \mathcal{B}(\mathcal{H}_3)$.

In this basis decomposition, the state in Eq. (4.40) takes the particularly simple form (see Supplemental document)

$$\rho^{\otimes N} = \bigoplus_{Y} p(Y)\, \omega^{(Y)} \otimes \frac{\mathbb{1}}{|\mathcal{P}_Y|}, \tag{4.44}$$

where $|\mathcal{P}_Y|$ denotes the dimension of space $\mathcal{P}_Y$, $\omega^{(Y)} \in \mathcal{B}(\mathcal{U}_Y)$ and $p(Y) = \mathrm{Tr}(E_Y \rho^{\otimes N})$, where $\{E_Y\}$ are given by

$$E_Y = \sum_{M=1}^{|\mathcal{U}_Y|} \sum_{\alpha=1}^{|\mathcal{P}_Y|} |Y, M, \alpha\rangle\langle Y, M, \alpha|, \tag{4.45}$$

with $|Y, M, \alpha\rangle \in \mathcal{U}_Y \otimes \mathcal{P}_Y$ an orthonormal basis.

Define the set

$$\Sigma_N := \left\{ \frac{Y}{N} \in [0,1]^d \;\middle|\; Y_1 \geq Y_2 \geq \ldots \geq Y_d \geq 0, \; \frac{1}{N} \sum_{k=1}^{d} Y_k = 1 \right\}, \tag{4.46}$$

and observe that $\frac{Y}{N}$ are multinomial distributions with $\lambda_k = Y_k/N$, $k \in (1, \ldots, d)$. More abstractly, they are measures on $[0,1]^d$. For example the set of possible measures for $N = 5$, $d = 2$ are shown in Fig. 4.13. As N increases the set Σ_N becomes denser and denser and in the limit $N \to \infty$ the set $\Sigma := \lim_{N\to\infty} \Sigma_N$ becomes the full set of measures on $[0,1]^d$.

Now, consider a subset $\Delta \subseteq \Sigma_N$. The probability that the spectrum of ρ belongs in this subset is given by

$$p_N(\boldsymbol{\lambda} \in \Delta) = \mathrm{tr}\left(E_N(\Delta) \rho^{\otimes N}\right) \tag{4.47}$$

Keyl and Werner [138] proved that

$$\lim_{N\to\infty} \sum_{Y} f\left(\frac{Y}{N}\right) \operatorname{tr}\left(E_N(Y)\rho^{\otimes N}\right) = f(\boldsymbol{\lambda}), \tag{4.48}$$

for any continuous function $f : \Sigma_N \to \mathbb{R}$. Thus, in the limit of large N, the integral over the set of measures Σ_N is dominated by a single spectrum, that of ρ. Specifically, the probability that the absolute error $\frac{Y}{N} - \boldsymbol{\lambda}$ is greater than some $\delta > 0$ is given by the Chernoff-Hoeffding bound

$$p_N\left(\left|\frac{Y}{N} - \boldsymbol{\lambda}\right| > \delta\right) \leq e^{-ND\left(\frac{Y}{N}||\boldsymbol{\lambda}\right)}, \tag{4.49}$$

and in the limit of large N the probability of making an error in estimating the true spectrum $\boldsymbol{\lambda}$ using the estimator $\frac{Y}{N}$ and the statistics of the POVM of Eq. (4.45) decays exponentially with the relative entropy between the two spectra.

For $d = 2$, corresponding to bosons with a polarization degree of freedom, the integer partitions are in one-to-one correspondence with the total angular momentum of N spin-1/2 systems

$$J(Y) = \frac{N}{2} - n_2, \tag{4.50}$$

and the corresponding measurement operators are given by

$$E_J = \sum_{M=-J}^{J} \sum_{\alpha=1}^{|\mathcal{P}_Y|} |J, M, \alpha\rangle\langle J, M, \alpha|, \tag{4.51}$$

with M the quantum number associated with the projection of angular momentum along some reference $\hat{z}$-direction. In our case this direction can be chosen to be the projection in the spatial modes that diagonalize the density matrix of Eq. (4.5).

This measurement has been used extensively in quantum information theory [121, 122, 145–147], it is often referred to as the weak Schur sampling measurement. The relevant transformation is the Schur transform—the unitary transformation that maps the uncoupled product basis to the total angular momentum basis.

In the next section I study the performance of the spectrum measurement in terms of its resolving power.

4.3.3 Precision estimation using the spectrum measurement

The state ρ of Eq. (4.5) is of rank-2 with eigenvalues given by

$$\lambda_k = \frac{1+(-1)^k r}{2}, \tag{4.52}$$

where $r = \sqrt{1-4q(1-q)(1-|\langle\Psi_L|\Psi_R\rangle|^2)}$ is the state's purity. Defining the eigenbasis of ρ as our z-axis, the conditional state and probability distribution $\omega^{(J)}$, $p(J)$ in Eq. (4.44) for a given total angular momentum value are given by [148]

$$\begin{aligned} p(J) =& \left(\frac{1-r^2}{4}\right)^{\frac{N}{2}} \binom{N}{\frac{N}{2}-J} \frac{2J+1}{\frac{N}{2}+J+1} Z_J \\ Z_J =& \sum_{M=-J}^{J} R^J = \frac{R^{J+1}-R^{-J}}{R-1} \\ R =& \frac{1+r}{1-r} \\ \omega^{(J)} =& \frac{1}{Z_J} \sum_{k=-J}^{J} R^k |J,k\rangle\langle J,k|. \end{aligned} \tag{4.53}$$

With this in hand we can compute the Fisher information, $F(p(J))$, for estimating the separation of two incoherent bosonic sources with known relative intensity, using the spectrum measurement. As $\mathcal{F}(\rho^{\otimes N}) = N\mathcal{F}(\rho)$, I compare the Fisher information *per boson* of this measurement to the QFI finding

$$\lim_{N\to\infty} \frac{F(p(J))}{N} = 4q(1-q)\frac{1}{4} = W\mathcal{F}(\rho), \tag{4.54}$$

where $W = 4q(1-q)$.

In Fig. 4.14 I plot the Fisher information of the spectrum measurement as a function of the separation, ϵ, between the two sources. For $q = 1/2$ the Fisher information per boson for separation estimation approaches the QFI for all values of ϵ, demonstrating the super resolving power of the spectrum measurement. Notice that for $N = 2$ the spectrum measurement is equivalent to the SWAP test and I recover the Fisher information of [30]. One observes how the addition of just one more boson increases the Fisher information from $\left(\frac{1}{8}+\frac{5}{128}\epsilon^2\right)$ to $\left(\frac{1}{6}-\frac{\epsilon^2}{24}\right)$.

4.3.4 Collective measurement implementation

To optimally estimate two incoherent point sources is a measure of their overlap in the desired degree of freedom. As discussed in the last section, this is a mea-

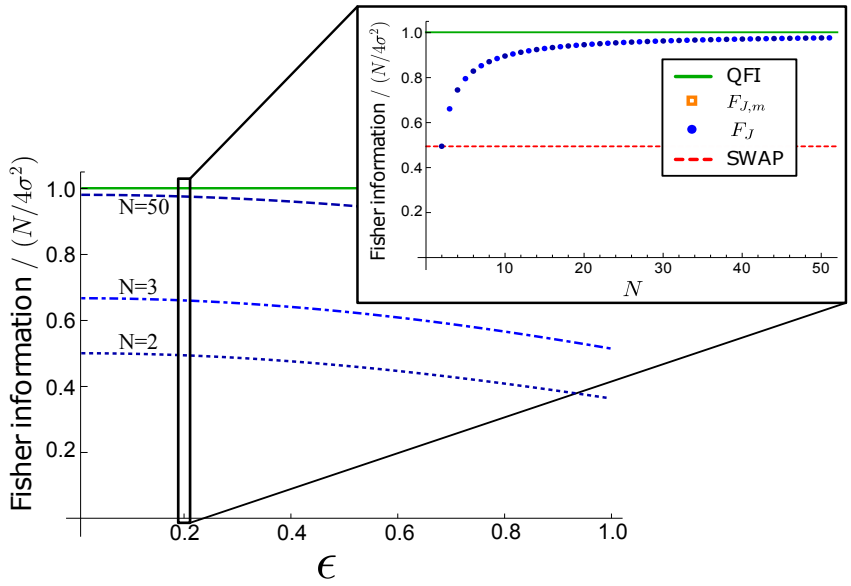

Figure 4.14: *Fisher Information as a function of the separation ϵ, of the spectrum measurement strategy for different number of bosons. I analyse the results for equal relative intensities $q = 0.5$. The blue results are the FI of ϵ for different number of bosons. The solid line is the QFI. The inset shows the scaling of the FI as a function of the number of copies for $\epsilon = 0.2$.*

sure of the symmetry under exchange of particles or the N bosons total angular momentum. This measurement is very important due to its non-destructive characteristic, i.e. it does not require particle absorption, allowing post-processing of the bosonic radiation, this is a key feature in estimating multiple parameters. The most efficient method to process N bosons are using quantum memories [149] and multi-core fiber optical fibers (or integrated circuits) [150, 151].

The general state $\rho^{\otimes N}$ does not live in the bosonic symmetric subspace. It describes the semi-classical state of N bosons multiplexed in different modes (spatial, temporal, polarization or frequency). Depending on which mode the state is multiplexed, different quantum memories are optimal for the task. For example, spatial temporal and polarization modes can be stored faithfully using electron spins [124, 152–157] or atomic ensembles [125–127, 158], whereas frequency modes can be mapped into NV centers [159] or trapped ions [160, 161].

From the existing techniques, super-resolution has been measured in the time/frequency degrees of freedom, using non-collective measurements. The atomic ensemble of Rydberg atoms placed in a gradient magnetic field can achieve

spectral/temporal multiplexing, allowing for projective measurements in superpositions of the spectral modes [158].

To estimate the separation between two photons in the spatial degree of freedom the cold atoms memories are the most promising technique, as this type of quantum memories is able to store the photons with its respective spatial modes. The spatial modes can be multiplexed in ensembles of atoms sequentially separated. After the storage, a collective measurements of the total J^2 angular momentum on all photons stored must be implemented [162]. With the challenges in storage-retrieval times probably up to four photons can be store with the current technology.

Alternatively, this collective measurement could be implemented with multi-port beam splitters, optical devices capable of measuring the photons distinguishability. In this setting, each copy of state ρ is input simultaneously in the multi-port beam splitter, based on the probability outputs of the device, the two sources separation is estimated based on the photons distinguishability. The simplest example of a multi-port beam splitter is a tritter [163–165], it consists of a three mode interference, it has been implemented with different optical setups [166, 167]. Other types of multi-port beam splitters rely on the fabrication of specially designed multi-core fibers, in which the choice of cladding controls the number of spatial modes allowed. In experimental setup, N separated fibers are bended together in a middle point, in which the interference of the spatial modes occurs. Then the photons are detected in N separated outputs. As these devices are extensions of the Hong-Ou-Mandel effect for more than two photons, the combinations of detectors clicking measures the photons distinguishability probability, therefore the two sources separation. The multi-port beam-splitters were implemented in [150, 151].

In parallel with this work, I have been working on multiparameter estimation using angular momentum measurements. More specifically, to estimate both the relative intensity, as well as the separation of the two incoherent point sources. The preliminary results indicate a post-measurement procedure is required to estimate relative intensity, projecting into superpositions of the spatial modes as in [168]. This measurement strategy corresponds to a collective measure of the total angular momentum J^2 and along a direction $\hat{n}$ of the angular momentum $J_{\hat{n}}$.

Note: In the results presented in [51] I describe the collective measurement of the total angular momentum J^2, as optimal for simultaneously estimation of both the separation and relative intensity, although, as the non-diagonal elements of the multiparameter Fisher matrix for this measurement are non-zero, this measurement is only optimal for estimating the separation for fixed relative intensity.

Chapter 5

A comparative study of estimation methods in quantum state tomography

In quantum state tomography, the prepared quantum state is reconstructed based on the measurement experimental outcomes. The error in the tomography depends not only on the experimental features, but also on the state estimation method, this error is called confidence region. I this chapter I compare different methods for computing the confidence regions for Least squares estimator.

Within the current technologies quantum entangled states can be successfully prepared [35–37], as a consequence, it is necessary to build a reliable procedure for state tomography[38, 39], state estimation based on the measurement outcomes of an experimental setting. There are different methods to compute confidence regions [3, 40–44]. These depend on the number of state prepare-and-measure rounds and on the chosen measurement strategies. They differ in the loss functions mean errors, on the asymptotic probabilities, and on the estimators low rank behaviour. Hence, truthful error bars, based not only on the experimental uncertainty, but also on the state estimations methods. The error in tomography procedures is called confidence region.

There are different methods for state estimation, for example, the Maximum Likelihood estimator [60, 169]. The error in this method is available only for mixed states [170], more specifically in the regime where local asymptotic normality holds. I will focus on comparing the confidence regions for the Least squares estimator.

As shown in Sec. 2.2 it is possible to extract the frequency of a measurement outcome from the data sampled, which yields the corresponding probability in the limit the experiment is repeated many times. If the quantum state is known this probability results from Born rule as $p_i = \mathrm{Tr}[E_i\rho]$, for each measurement operator E_i. One way to estimate the quantum state is by minimizing the difference between the frequency of a measurement outcome and its corresponding probability distribution. For example, using the Least squares minimization [171]

$$\hat{\rho} = \underset{\rho\in\mathcal{H}_d}{\mathrm{argmin}} \sum_{i=1}^{m} \left(f_i - \mathrm{Tr}(E_i\rho)\right)^2 . \tag{5.1}$$

where f_i is the frequency of outcome i, E_i is the POVM measurement and ρ is the state over which the minimization will occur, under the conditions for a physical state, i.e. positive semi-definiteness $\rho \geq 0$ and $\mathrm{Tr}[\rho] = 1$.

Eq. (5.1) has a explicit solution based on properties of the Born rule. It is an injective linear map $\mathcal{T} : \mathcal{H}_d \to \mathcal{R}^m$, such that $[\mathcal{T}(\rho)]_i = \mathrm{Tr}[E_i\rho]$, then the estimator is [40]

$$\hat{\rho} = \left(\mathcal{T}^\dagger\mathcal{T}\right)^{-1}\left(\mathcal{T}^\dagger(\boldsymbol{f})\right), \tag{5.2}$$

this is called the Least squares estimator, and $\boldsymbol{f}$ is the vector of frequencies of measurement outcomes, defined in Eq. (2.14).

This shows the estimator depends directly on the measurements performed. I will focus on the most common measurement implemented in an experimental

The sequence of independent and identically prepared quantum states approaches a normal (gaussian) distribution

setup; the Pauli basis measurement. In this strategy each qubit is measured locally in the Pauli basis.

$$\sigma_x = \begin{pmatrix} 0 & 1 \\ 1 & 0 \end{pmatrix} \qquad \sigma_y = \begin{pmatrix} 0 & -i \\ i & 0 \end{pmatrix} \qquad \sigma_z = \begin{pmatrix} 1 & 0 \\ 0 & -1 \end{pmatrix} \tag{5.3}$$

For a single qubit, there is a cartesian view of the measurement process using the Bloch sphere, in which the Pauli basis measurements are projection operators on the Bloch sphere axis.

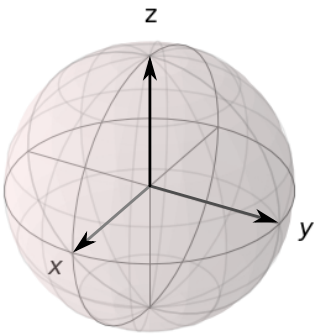

Figure 5.1: *Bloch representation of Pauli measurements for a single qubit.*

The tomography scheme is general for k qubits, the Pauli basis measurement strategy, corresponds to projections in tensor products of the Pauli matrices, such that there are 3^k combinations of measurement operators. Each measurement setting is the tensor product of k pauli matrices $\boldsymbol{s} \in \{\sigma_x, \sigma_y, \sigma_z\}^k$ with 2^k outcomes $\boldsymbol{o} \in \{\pm 1\}^k$, and it can be written as the measurement operator$\boldsymbol{W}_k = |w_{\boldsymbol{o}}^{\boldsymbol{s}}\rangle\langle w_{\boldsymbol{o}}^{\boldsymbol{s}}|$.

5.1 Confidence Region

A confidence region is the region in the state's space in which the quantum state can be found with high probability. Before discussing the different methods to compute this region I first define the quantum state in the Bloch representation. For one qubit, this vector is a tri-dimensional vector in the Bloch sphere, whereas, for k qubits it is a vector of $d^2 - 1$ components with $d = 2^k$, and the density matrix is

$$\rho = \frac{1}{d}\left(\mathbb{1} + \sqrt{\frac{d(d-1)}{2}}\boldsymbol{r} \cdot \boldsymbol{W}_k'\right) \tag{5.4}$$

where $\boldsymbol{r}$ belongs to the Euclidean metric of $\mathbb{R}^{d^2-1}$ representing the state in the Hilbert-Schmidt metric $\mathcal{S}(\mathcal{H}_d)$. Here I denote $\boldsymbol{W}'_k$ as the observables of the quantum state, which for multiple qubits must include also the identity $\boldsymbol{s'} = \{\mathbb{1}, \sigma_x, \sigma_y, \sigma_z\}^k$, here I assume any projection with $\boldsymbol{W}'_k$ can be obtained tracing out elements of projections with $\boldsymbol{W}_k$. Similarly, each measurement strategy E_i is a function of a $\{d^2-1\}$ dimensional vector $\boldsymbol{\eta_i}$ as

$$E_i = \frac{1}{m_i}\left(\mathbb{1} + \sqrt{\frac{d(d-1)}{2}}\boldsymbol{\eta_i}\cdot\boldsymbol{W'}\right), \tag{5.5}$$

where m_i is the weight of each outcome, in case all measurements have equal weights $m_i = m = 2^k.3^k$.

There are different methods to compute the confidence regions, the optimal figure of merit for confidence regions comparison is still under investigation. Here I choose two of the the most relevant methods for building confidence regions.

5.1.1 Polytope regions

In the method of Wang *et. al.* [3], each measurement strategy defines a half-plane and the enclosed region inside the intersection between all the half planes defines the confidence region. The region is based on the POVM element E_i and on the measured frequency $f_i = \frac{n_i}{N}$ of the corresponding outcome, the intersection of all half-spaces, for all the measurement POVM elements, then defines the confidence region.

$$\Gamma_i(n_i) = \left\{\sigma \in \mathcal{S}(\mathcal{H}_d) : \mathrm{tr}\left(E_i\sigma\right) \leq \frac{n_i}{N} + \epsilon_N\left(n_i, \frac{\delta}{m}\right)\right\}, \tag{5.6}$$

where m is the total number of measurements and $1-\delta$ is the desired confidence. $\Gamma_i(n_i)$ sets the polytope plane, and the confidence region is $\Gamma(\boldsymbol{n}) = \bigcap\Gamma_i(n_i)$.

Here $\epsilon_N\left(n_i, \frac{\delta}{m}\right)$ is the positive root solution of the relative entropy equation $D(x||y) = x\log(x/y) + (1-x)\log[(1-x)/(1-y)]$ with parameters

$$D\left(\frac{n_i}{N}\middle|\middle|\frac{n_i}{N} + \epsilon_N\right) = -\frac{1}{N}\log\left[\frac{\delta}{m}\right]. \tag{5.7}$$

Taylor expanding Eq. 5.7 for $\epsilon_N \approx 0$ gives the following expression for the positive root

$$\epsilon_N \simeq \sqrt{2\log\left[\frac{\delta}{m}\right]\frac{(n_i - N)n_i}{N^3}} \tag{5.8}$$

For example in the measurement strategy chosen for comparison the half-spaces form a polygon. In the single qubit scenario, the confidence region is a cube in the Bloch sphere.

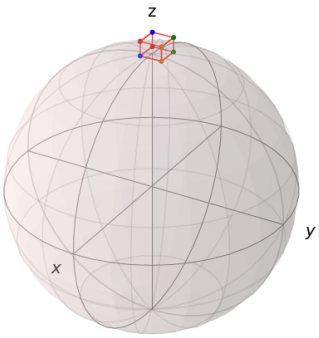

Figure 5.2: *Bloch representation one qubit estimation in z direction with polytope confidence region of [3] performing Pauli basis measurement.*

In this work, the authors relate this method of computing confidence regions with the Clopper-Pearson confidence intervals, a method for calculating binomial confidence intervals[1] based on the cumulative probability of the binomial distribution. This comparison ensures this region is in the chosen confidence level, as this confidence intervals never result in an overestimation of the confidence level.

5.1.2 Least squares confidence region

In the work of M Guţă et. al. [40], the authors derived the error bound in estimating a state using the least squares estimator and projected least squares estimator[2]. The bound states the probability of finding an estimate within a region is not larger than δ ($\delta = 1 - \text{confidence}$). This sets a length in the trace norm of the difference between the estimated state and the true state. For the Least squares estimate this bound is

$$\Pr\left[\left\|\hat{\rho}_{LS} - \rho\right\|_{\infty} \geq \tau\right] \leq d e^{-\frac{-3N\tau^2}{8d^{1.6}}} \qquad \tau \in [0,1]\,, \tag{5.9}$$

where $\|\cdot\|_{\infty}$ it is the operator norm which corresponds to the largest eigenvalue, $d = 2^k$ and N total number of measurements, as in the last subsection. The desired confidence $1 - \delta$ is imposed by solving for τ the r.h.s. of Eq. (5.9) as $d e^{-\frac{-3N\tau^2}{8d^{1.6}}} = \delta$.

1. is a confidence interval for the probability of success [80] based on the outcomes of a series of success–failure experiments

2. I will restrict my analysis to the Least squares estimate, as the projected Least squares estimator requires a number of copies of the initial state larger than the scope of this thesis

This method relies on minimizing the least squares function, as in the example of Eq. 5.1, defining the measurement strategies as local Pauli basis measurements. The solution to Eq. 5.2 has a closed form expression [40]

$$\hat{\rho}_{LS} = \frac{1}{3^k} \sum_{\boldsymbol{s},\boldsymbol{o}} \boldsymbol{f}_{\boldsymbol{s},\boldsymbol{o}} \bigotimes_{i=1}^{k} (3\boldsymbol{W}_k - \mathbb{1}) \,. \tag{5.10}$$

where the frequency $\boldsymbol{f}_{s_i,o_j}$ of a measurement setting s_i and output o_j, $\frac{n_{s_i,o_j}}{N}$.

In this method with Pauli basis measurement, the confidence region is an ellipsoid, with principal axis related to the norm $\|\hat{\rho}_{LS} - \rho\|_\infty$. For one qubit this corresponds to an ellipsoid around the least squares point estimate in the bloch sphere.

5.2 A comparative study

In this section I propose a comparison method for the confidence regions described. This methods is general for confidence regions comparison, and it was implemented by means of numerical simulations.

5.2.1 Non-intersecting regions

In this method I estimate two states $\hat{\rho}_1$ and $\hat{\rho}_2$ and find the confidence region of each of them, $\mathcal{C}_{\hat{\rho}_1}$ and $\mathcal{C}_{\hat{\rho}_2}$. For small data size N the confidence region for each state can be as large as the state space and the probability of finding an arbitrary state $\hat{\rho}_f$ in the intersection $\mathcal{C}_{\hat{\rho}_1} \bigcap \mathcal{C}_{\hat{\rho}_2}$ is always 1. However, increasing the data size sampling N, reduces the size of the confidence region, such that this probability slowly decays to zero, I will define such probability as κ

$$\kappa_N = \Pr\left[\hat{\rho}_f \in \bigcap_{i=1}^{2} \mathcal{C}_{\hat{\rho}_i}\right] . \tag{5.11}$$

The state $\hat{\rho}_f$ results of a convex optimization, using semi-definite programming. The probability κ is the the frequency $\hat{\rho}_f$ is found in the intersecting regions, after large number of repetitions the two-states estimation for a fixed data size N.

Here I add a scheme after a simulation of this procedure for the method of polytope regions. It is the estimation of two one-qubit state, $\rho_1 = |z\rangle\langle z|$ and $\rho_2 = \mathbb{1}$.

In comparing confidence regions, it is very important not to overestimate the region for a desired confidence. This is the basis of the intersecting regions

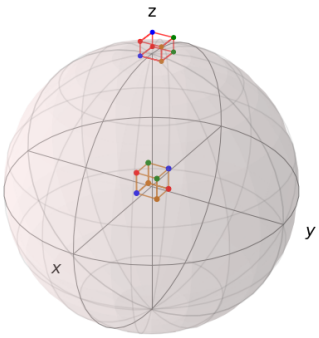

Figure 5.3: *Bloch representation two one-qubit state estimation* $\rho_1 = |z\rangle\langle z|$ *and* $\rho_2 = \mathbb{1}$*. For* $N = 10^4$ *and confidence* 0.99*, the regions do not intersect.*

method. After repeating the simulations with different states; I observe the following behaviour for a single qubit. The polytope regions method gives a tighter region, as the regions stop intersecting for a smaller value. Whereas for two or more qubits the Least squares confidence region is tighter, an example of this result is presented in Fig 5.4.

In this section I have presented a novel method to compare confidence regions, which showed different methods are optimal depending on the number of qubits. For a single-qubit tomography procedure, the confidence region must be computed using the polytope method, whereas, for two or more qubits the confidence region must be computed using the Least-squares confidence region method.

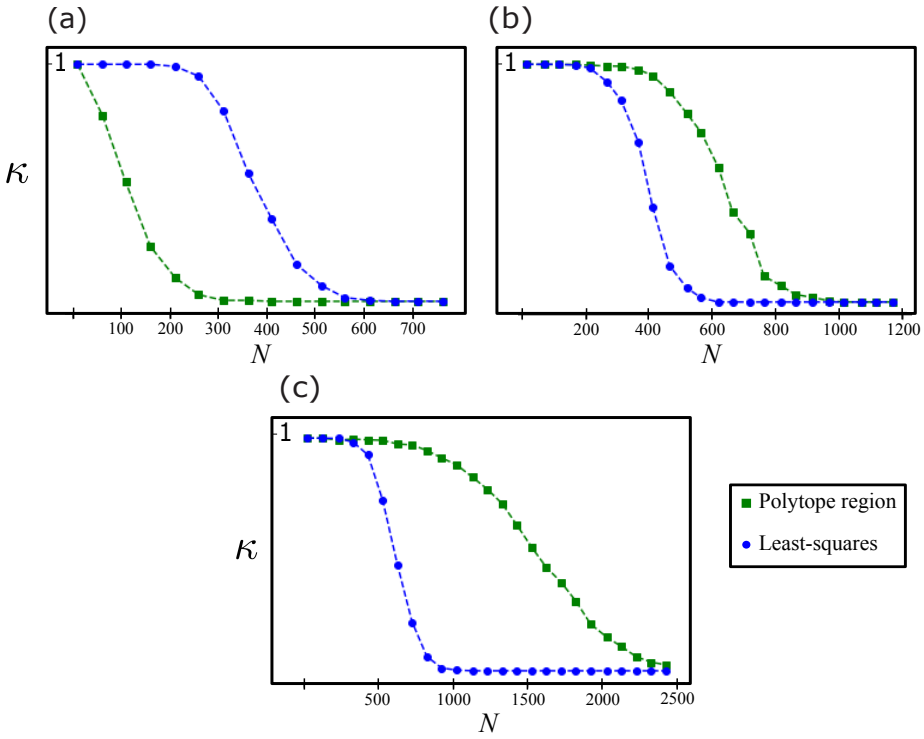

Figure 5.4: *a) Polytope intersection for single-qubit states* $\rho_1 = |z\rangle\langle z|$ *and* $\rho_2 = \mathbb{1}$ *with confidence* 0.9. *b) Polytope intersection for two-qubit states, Bell state* $\rho_1 = |\Phi^+\rangle\langle\Phi^+|$ *and* $\rho_2 = \mathbb{1}$ *with confidence* 0.9. *c) b) Polytope intersection for three-qubit states* $\rho_1 = \mathrm{GHZ}$ *and* $\rho_2 = \mathbb{1}$ *with confidence* 0.9.

Chapter 6

Conclusions and Outlook

In this thesis I approach fundamental limits in optics, showing how quantum mechanics is a useful resource to find measurement strategies capable of transpassing the classical limits in resolution and interference. In Chap. 3 and 4 I discuss how to apply the theoretical results to design more precise experiments. In Chap. 5 I discuss fundamental definition for the error in quantum state tomography.

In this section I discuss how some of the results in this thesis will be useful in future projects.

On interference experiments, in Chap. 3 I discussed a measurement strategy capable of measuring nonclassical paths in the double-slit experiment. Moreover, to study the behaviour of nonclassical paths in different setups would provide a unified framework for this results. For example analyzing the nonclassical paths in the Mach-Zehnder interferometer, as this two setups have similar properties [172–174] this results could provide a more complete description of the nonclassical paths.

In Chap. 4 of this thesis, I discuss measurements capable of resolving the separation of two incoherent sources bellow the Raylegh criteria. I analyse the spatial mode demultiplexing (SPADE) measurements and its dependence on the exact knowledge of the centroid of the distribution. I propose the ROTADE measurement, which depend only on the zeroth and first demultiplexing modes, and I show how to mitigate misalignment in demultiplexing measurements. In addition, I exploit the symmetry of the two-sources quantum state to estimate their separation using collective measurements strategies of the total angular momentum. The natural follow-up of the last project, is currently a work in progress of solving the general problem in which the two source relative intensity is not know beforehand. As the results in the literature show, it is not possible to find a measurement strategy capable of simultaneously estimating the two

sources separation and intensity, this indicates the spectrum measurement due to its collective and non-destructive properties, followed by a post-measurement strategy would suit for estimation of both parameters. Moreover, an outlook of this project is to analyse if the limit of asymptotic number of copies of the initial two photons state behaves as coherent states.

In the last topic of this thesis, I discussed how to derive the error in quantum state tomography called the confidence regions. The method used showed different methods are optimal depending on the number of qubits. As a follow-up of this results a comparison of the quantile of the distribution could give a different figure of merit for confidence regions comparison.

Appendix A

Appendix Measuring nonclassical paths with atoms in the double slit experiment

A.1 Nonclassical paths wave function

In this appendix we define the constants used in Eq.(3.8-3.10):

$$\Gamma_c = -\frac{im\beta}{\pi^{1/4}\sqrt{-im\sigma_0 + \frac{t\hbar}{\sigma_0}}} \cdot \times \frac{1}{\sqrt{\frac{-im^2\beta^2\sigma_0^2 + m(t\beta^2 + (\beta^2+\sigma_0^2)\tau)\hbar + it\tau\hbar^2}{m\sigma_0^2 + it\hbar}}} \tag{A.1}$$

$$c_0 = -\frac{m(d^2 m\sigma_0^2 + id^2(t+\tau)\hbar)}{8m^2\beta^2\sigma_0^2 + 8im(t\beta^2 + (\beta^2+\sigma_0^2)\tau)\hbar - 8t\tau\hbar^2} \tag{A.2}$$

$$c_1 = \frac{m(4dm\sigma_0^2 + 4idt\hbar)}{8m^2\beta^2\sigma_0^2 + 8im(t\beta^2 + (\beta^2+\sigma_0^2)\tau)\hbar - 8t\tau\hbar^2} \tag{A.3}$$

$$c_2 = -\frac{m(4m(\beta^2+\sigma_0^2) + 4it\hbar)}{8m^2\beta^2\sigma_0^2 + 8im(t\beta^2 + (\beta^2+\sigma_0^2)\tau)\hbar - 8t\tau\hbar^2} \tag{A.4}$$

$$\Gamma_{nc} = -\frac{m^{3/2}\beta^2\left(-\frac{1}{\pi}\right)^{1/4}}{\sqrt{-im\sigma_0+\frac{t\hbar}{\sigma_0}}}\frac{1}{\sqrt{\frac{-im^2\beta^2\sigma_0^2+m(t\beta^2+\epsilon(\beta^2+\sigma_0^2))\hbar+it\epsilon\hbar^2}{m\sigma_0^2+it\hbar}}}. \tag{A.5}$$
$$\times\frac{1}{\sqrt{\frac{-im^3\beta^4\sigma_0^2+m^2\beta^2(t\beta^2+\beta^2(\epsilon+\tau)+\sigma_0^2(\epsilon+2\tau))\hbar+im(\epsilon(\beta^2+\sigma_0^2)\tau+t\beta^2(\epsilon+2\tau))\hbar^2-t\epsilon\tau\hbar^3}{m^2\beta^2\sigma_0^2+im(t\beta^2+\epsilon(\beta^2+\sigma_0^2))\hbar-t\epsilon\hbar^2}}}$$

$$c_0' = -\frac{m(2d^2m^2\beta^2\sigma_0^2+id^2m(2t\beta^2+2\beta^2(\epsilon+\tau)+\sigma_0^2(\epsilon+4\tau))\hbar-d^2(\epsilon\tau+t(\epsilon+4\tau))\hbar^2)}{8(m^3\beta^4\sigma_0^2+im^2\beta^2(t\beta^2+\beta^2(\epsilon+\tau)+\ \sigma_0^2(\epsilon+2\tau))\hbar-m(\epsilon(\beta^2+\sigma_0^2)\tau+t\beta^2(\epsilon+2\tau))\hbar^2-it\epsilon\tau\hbar^3)} \tag{A.6}$$

$$c_1' = -\frac{m(4idm\epsilon(\beta^2+\sigma_0^2)\hbar-4dt\epsilon\hbar^2)}{8(m^3\beta^4\sigma_0^2+im^2\beta^2(t\beta^2+\beta^2(\epsilon+\tau)+\ \sigma_0^2(\epsilon+2\tau))\hbar-m(\epsilon(\beta^2+\sigma_0^2)\tau+t\beta^2(\epsilon+2\tau))\hbar^2-it\epsilon\tau\hbar^3)} \tag{A.7}$$

$$c_2' = -\frac{m(4m^2\beta^2(\beta^2+2\sigma_0^2)+4im(2t\beta^2+\epsilon(\beta^2+\sigma_0^2))\hbar-4t\epsilon\hbar^2)}{8(m^3\beta^4\sigma_0^2+im^2\beta^2(t\beta^2+\beta^2(\epsilon+\tau)+\sigma_0^2(\epsilon+2\tau))\hbar-m(\epsilon(\beta^2+\sigma_0^2)\tau+t\beta^2(\epsilon+2\tau))\hbar^2-it\epsilon\tau\hbar^3)} \tag{A.8}$$

The parameter constants used are
$m = 1.44.10^{-25}$kg, $d = 5\mu$m, $\sigma_0 = \beta = 0.3\mu$m,
$t = \tau = 5$ms, and $\epsilon = 2.9$ms.

A.2 Probability distribution including intra-cavity photodetection

The time evolution of the density matrix [state in Eq. (3.19)], setup with cavities in both slits including the beam splitter and intracavity photodetectors P^+ and P^-, where the photodetection occurs at individual time intervals, such that the density matrix is calculated solving:

$$\rho(t) = e^{-\Gamma N t}\rho(0)e^{-\Gamma N t} + 2\Gamma \sum_{s=-,+} \int_0^t dt' e^{-\Gamma N(t-t')} a_s e^{-\Gamma N t'} \rho(0) e^{-\Gamma N t'} a_s^\dagger e^{-\Gamma N(t-t')} +$$

$$+(2\Gamma)^2 \sum_{s,s'=-,+} \int_0^t dt' \int_0^{t'} dt'' e^{-\Gamma N(t-t')} a_s e^{-\Gamma N(t'-t'')} a_{s'} e^{-\Gamma N t''} \rho(0) e^{-\Gamma N t''} a_{s'}^\dagger e^{-\Gamma N(t'-t'')} a_s^\dagger e^{-\Gamma N(t-t')} +$$

$$+(2\Gamma)^3 \sum_{s,s',s''=-,+} \int_0^t dt' \int_0^{t'} dt'' \int_0^{t''} dt''' e^{-\Gamma N(t-t')} a_s e^{-\Gamma N(t'-t'')} a_{s'} e^{-\Gamma N(t''-t''')} a_{s''} e^{-\Gamma N(t''')} \rho(0) e^{-\Gamma N t'''} a_{s''}^\dagger e^{-\Gamma N(t''-t''')} a_{s'}^\dagger e^{-\Gamma N(t'-t'')} a_s^\dagger e^{-\Gamma N(t-t')}$$

where N is the number of photons operator and Γ is the cavity width. Equation (A.2) is obtained under the assumption photodetection is a stochastic jump process [175–177]. The first term corresponds to the probability of zero photon absorption, the second term corresponds to the probability of a single photon absorption, the third is the two photon absorption and the last is three photon absorption.

In the limit of long interaction time, $\Gamma t \to \infty$, both $\frac{1}{6}\left(e^{2\Gamma t}-1\right)^3$ and $\frac{1}{2}\left(e^{2\Gamma t}-1\right)^2$ tend to 1.

Number of photons	Photodetector	Atom - ground state ($\times \frac{1}{N_2} e^{-6\Gamma t}$)	Atom - excited state ($\times \frac{1}{N_2} e^{-4\Gamma t}$)
0	———	$\left(\|\psi_c^+\|^2 + \|\psi_c^-\|^2\right)$	$\left(\|\psi_{nc}^+\|^2 + \|\psi_{nc}^-\|^2\right)$
1	$+$	$\left(e^{2\Gamma t}-1\right)\left(\frac{3}{2}\|\psi_c^+\|^2 + \frac{1}{2}\|\psi_c^-\|^2\right)$	$\left(e^{2\Gamma t}-1\right)\left(\|\psi_{nc}^+\|^2 + \|\psi_{nc}^-\|^2\right)$
	$-$	$\left(e^{2\Gamma t}-1\right)\left(\frac{1}{2}\|\psi_c^+\|^2 + \frac{3}{2}\|\psi_c^-\|^2\right)$	$\left(e^{2\Gamma t}-1\right)\left(\|\psi_{nc}^+\|^2 + \|\psi_{nc}^-\|^2\right)$
2	$++$	$\frac{1}{2}\left(e^{2\Gamma t}-1\right)^2\left(\frac{5}{2}\|\psi_c^+\|^2 + \frac{1}{2}\|\psi_c^-\|^2\right)$	$\frac{1}{2}\left(e^{2\Gamma t}-1\right)^2\left(\|\psi_{nc}^+\|^2\right)$
	$--$	$\frac{1}{2}\left(e^{2\Gamma t}-1\right)^2\left(\frac{1}{2}\|\psi_c^+\|^2 + \frac{9}{2}\|\psi_c^-\|^2\right)$	$\frac{1}{2}\left(e^{2\Gamma t}-1\right)^2\left(\|\psi_{nc}^+\|^2\right)$
	$+-$ or $-+$	$\frac{1}{2}\left(e^{2\Gamma t}-1\right)^2\left(\frac{1}{2}\|\psi_c^+\|^2 + \frac{1}{2}\|\psi_c^-\|^2\right)$	$\frac{1}{2}\left(e^{2\Gamma t}-1\right)^2\left(\|\psi_{nc}^-\|^2\right)$
3	$+++$	$\frac{1}{6}\left(e^{2\Gamma t}-1\right)^3\left(\frac{9}{2}\|\psi_c^+\|^2\right)$	———
	$---$	$\frac{1}{6}\left(e^{2\Gamma t}-1\right)^3\left(\frac{9}{2}\|\psi_c^-\|^2\right)$	
	$+--$ or $-+-$ or $--+$	$\frac{1}{6}\left(e^{2\Gamma t}-1\right)^3\left(\frac{1}{2}\|\psi_c^+\|^2\right)$	
	$++-$ or $-++$ or $+-+$	$\frac{1}{6}\left(e^{2\Gamma t}-1\right)^3\left(\frac{1}{2}\|\psi_c^-\|^2\right)$	

Table A.1: *Probability distribution at each single photodetection, the order of $+$ and $-$ signs correspond to the temporal order of the photodetection.*

Appendix B

Appendix Discrimination and estimation of incoherent sources

B.1 Error probability - Hypothesis Testing

In this section I explain some details of the discrimination scenario of one-vs-two sources. The first step is to write ROTADE measurement vectors (Eq. 4.21) in the spatial representation as

$$
\begin{aligned}
E_1(x,y) = \langle x|\Psi_1(\theta)\rangle\langle\Psi_1(\theta)|y\rangle = &\left(\sin\frac{\theta}{2}\Psi(x-x_D) + \cos\frac{\theta}{2}\left(\frac{-\dot{\Psi}(x-x_i)}{\sqrt{\mathcal{N}}}\bigg|_{x_i=x_D}\right)\right)\cdot \\
&\left(\sin\frac{\theta}{2}\Psi(y-x_D) + \cos\frac{\theta}{2}\left(\frac{-\dot{\Psi}(x-x_i)}{\sqrt{\mathcal{N}}}\bigg|_{x_i=x_D}\right)\right) \\
E_2(x,y) = \langle x|\Psi_2(\theta)\rangle\langle\Psi_2(\theta)|y\rangle = &\left(-\cos\frac{\theta}{2}\Psi(x-x_D) + \sin\frac{\theta}{2}\left(\frac{-\dot{\Psi}(x-x_i)}{\sqrt{\mathcal{N}}}\bigg|_{x_i=x_D}\right)\right)\cdot \\
&\left(-\cos\frac{\theta}{2}\Psi(y-x_D) + \sin\frac{\theta}{2}\left(\frac{-\dot{\Psi}(x-x_i)}{\sqrt{\mathcal{N}}}\bigg|_{x_i=x_D}\right)\right)
\end{aligned}
\tag{B.1}
$$

where $\dot{\Psi}(x-x_i) = \frac{\partial\Psi(x-x_i)}{\partial x_i}$, $E_1(x,y)$ is the spatial representation of the negative projector of the Helstrom measurement $|\Psi_1(\theta)\rangle\langle\Psi_1(\theta)|$, and $E_2(x,y)$ is the spatial representation of the positive projector of the Helstrom measurement $|\Psi_2(\theta)\rangle\langle\Psi_2(\theta)|$.

The density matrix projected in the spatial representation is

$$\begin{aligned}\rho^{(1)}(x,y) =& \langle x|\rho^{(1)}|y\rangle = \Psi(x-x_0)\Psi(y-x_0)\\ \rho^{(2)}(x,y) =& \langle x|\rho^{(2)}|y\rangle = \frac{1}{2}\Psi(x-x_L)\Psi(y-x_L) + \frac{1}{2}\Psi(x-x_R)\Psi(y-x_R)\end{aligned} \quad \text{(B.2)}$$

And error probability is therefore the integral of x and y in the interval $[-\infty,\infty]$

$$p(f(y) = H^{(j)}|H^{(i)}) = \int dy \int dx E_j(x,y)\rho^i(x,y) \quad \text{(B.3)}$$

with $j \neq i$.

To obtain the Chernoff exponent (Eq. 2.44) requires a numerical minimisation of the s exponent, explicitly dependent on the parameter θ.

B.2 Estimating the separation between Sinc-Bessel modes under misalignment

In this appendix section, we present the results of estimating the separation between two incoherent point sources imaged by a system with a rectangular aperture. The PSF of such a system is given by the Sinc function (see Eq. (2.3)).

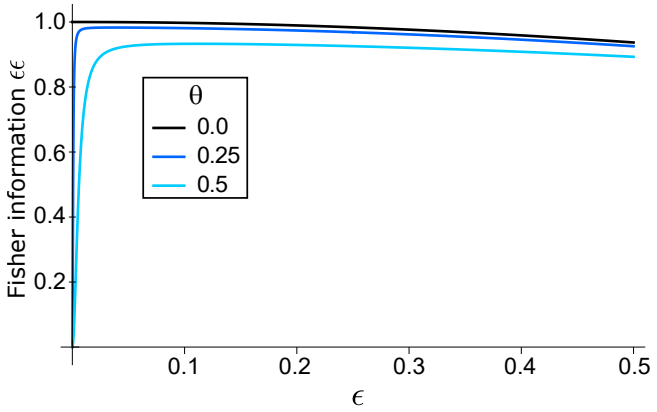

Figure B.1: Rectangular aperture: $\frac{\mathcal{F}_{\epsilon\epsilon}}{n}$ *for the equivalent to ROTADE measurement, as a function of separation for a rectangular aperture with* $\sigma = 1$ *for different misalignments.*

Repeating the calculation in Section 4.2.3 the eigenvalues and corresponding eigenvectors of $\rho_{\mathrm{S}}^{(2)}$ are:

$$\begin{aligned} \mu_1(\epsilon) &= \frac{\epsilon^2}{3}, \quad |\psi_1(\theta)\rangle = \sin\frac{\theta}{\sqrt{3}}|0\rangle + \cos\frac{\theta}{\sqrt{3}}|1\rangle \\ \mu_2(\epsilon) &= 1 - \mu_1(\epsilon), \quad |\psi_2(\theta)\rangle = -\cos\frac{\theta}{\sqrt{3}}|0\rangle + \sin\frac{\theta}{\sqrt{3}}|1\rangle, \end{aligned} \tag{B.4}$$

and using Eq. (2.31) the corresponding SLD operators are, in the eigenbasis of $\{|\psi_1(\theta)\rangle, |\psi_2(\theta)\rangle\}$ are given by

$$\begin{aligned} \mathcal{L}_\theta &= \left(\frac{6-4\epsilon^2}{3\sqrt{3}}\right)\sigma_x \\ \mathcal{L}_\epsilon &= \frac{2}{\epsilon}\begin{pmatrix} 1 & 0 \\ 0 & \frac{\epsilon^2}{\epsilon^2-3} \end{pmatrix}. \end{aligned} \tag{B.5}$$

The eigenvectors of the SLD operators can now easily be computed to be:

$$|\theta_{\pm}\rangle = \frac{1}{\sqrt{2}}\left(\left(\sec\frac{2\theta}{\sqrt{3}} \pm \tan\frac{2\theta}{\sqrt{3}}\right)\sqrt{1 \mp \sin\frac{2\theta}{\sqrt{3}}})|0\rangle + \right.$$
$$\left. + \sqrt{1 \mp \sin\frac{2\theta}{\sqrt{3}}})|1\rangle\right) \tag{B.6}$$
$$|\epsilon_{\alpha}\rangle = |\psi_{\alpha}(\theta)\rangle, \tag{B.7}$$

The optimal measurement to detect the separation for known misalignment is analogous to ROTADE with angle $\frac{\theta}{\sqrt{3}}$.

In the case of no misalignment the optimal measurement is given by the first two Sinc-Bessel modes [178]. In the presence of misalignment the optimal measurements furnished by the qubit model are unitarily related to the same two Sinc-Bessel modes. The Fisher information for various values of misalignment for the Sinc PSF are shown in Figure B.1. Similar to Sec. 4.2.3 we can analyse the minimal resolvable distance under misalignment to estimate the separation of Sinc PSF $\epsilon_{\min}^{(R_{\text{Sinc}})}(\theta) \approx \frac{\theta^{3/2}}{\sqrt[4]{n}\sqrt{5\sqrt{3^3}}}$, this is an improvement in contrast with the minimal resolvable distance of SPADE01 $\epsilon_{\min}^{(01_{\text{Sinc}})}(\theta) \approx \frac{\sqrt[4]{3}\sqrt{\theta}}{\sqrt{2}}$.

B.3 Discrimination of Sinc-Bessel modes

In this appendix, we present the results of discriminating one from two incoherent point sources imaged by a system with a rectangular aperture. The PSF of such a system is given by the Sinc function (see Eq. (2.3)). We compare the measurement strategies of ROTADE and SPADE01 with the quantum Chernoff bound in function of the misalignment, as presented in Figure B.2 and the separation, in Figure B.3.

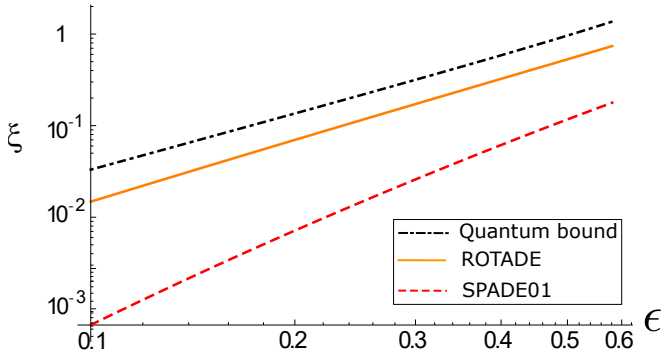

Figure B.2: *Chernoff exponent for Sinc PSF in function of the separation, with misalignment 0.25,* $\sigma = 1$.

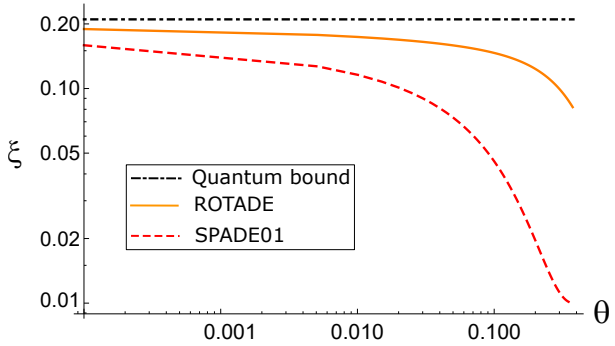

Figure B.3: *Chernoff exponent for Sinc PSF in function of the misalignment, for fixed separation 0.25,* $\sigma = 1$.

Similarly to the results in the main text, we verify in the limit asymptotic limit, ROTADE performs better than SPADE01.

B.4 Performance of ROTADE in discrimination

Here we analyse the performance of ROTADE for the task of discriminating one and two light sources. As ROTADE involves only thee two-dimensional subspace spanned by the zeroth and first HG modes, an intrinsic error probability arises when the incoming radiation couples into higher HG modes. This probability is useful for defining the regime of validity of the qubit model.

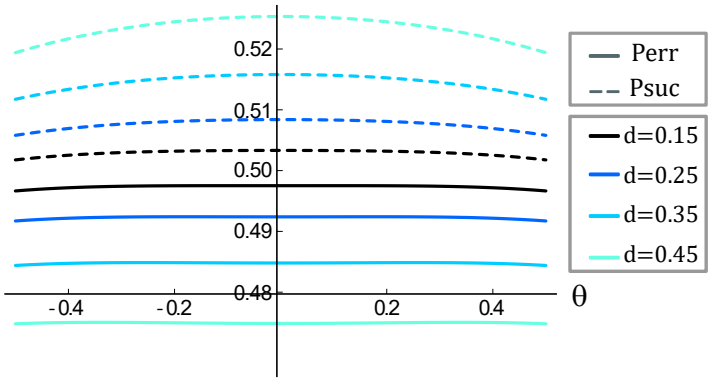

Figure B.4: *Error (solid) and success (dashed) probability in function of the reference position, using ROTADE for distinguishing between one and two sources, for different separations between the two sources.*

For example Figure B.4 presents the error and success probabilities in the regime where the centre of each distribution are aligned $\theta = 0$. We observe that ROTADE has constant value (less than 4% variation), e.g., at $\theta = 0$ the error probability has value $P_{\text{err}} = \frac{1}{2}(P_{\text{err1}} + P_{\text{err2}}) = \frac{1}{2}\left(0 + e^{\frac{-d^2}{4\sigma^2}}\right)$, and the success probability $P_{\text{suc}} = \frac{1}{2}(P_{\text{suc1}} + P_{\text{suc2}}) = \frac{1}{2}\left(1 + \frac{d^2}{4\sigma^2}e^{\frac{-d^2}{4\sigma^2}}\right)$. As d increases, the likelihood that photons couple to higher HG modes increases and hence the error (success) probability move further away from the priors, 0.5. This is a consequence of the intrinsic error of the qubit model.

The intrinsic error is the distance between the sum of the error and success probabilities from unity. It dictates until which separation and reference position the qubit model—and consequently ROTADE—are adequate. For $|\theta| < \frac{1}{2}$, or when the separation between the sources is comparable to σ, $\epsilon < \frac{1}{2}$, this error is negligible. This features are presented in Figure B.5 and B.6, respectively.

In Figure B.5 we present the intrinsic error in function of the misalignment θ. For a range of misalignments, $|\theta| < \frac{1}{2}$, ROTADE has negligible intrinsic error.

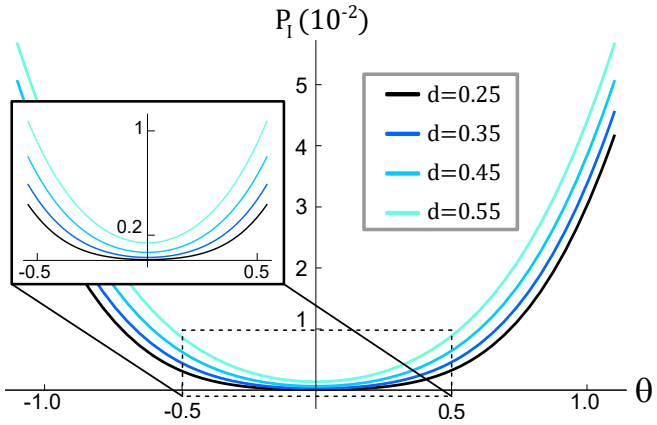

Figure B.5: *Intrinsic error of the qubit model ($\mathrm{P_I}$) in function of the misalignment θ, for different separations d between the sources.*

Figure B.6 shows the intrinsic error in function of the two source separation ϵ, for misaligned source distributions, i.e., the centroid of the two sources is different from the center of one source ($x_\mathrm{c} \neq x_0$). We observe, that the qubit model is adequate when placing the measurement in between the distribution centroids $x_\mathrm{c} \leq x_R \leq x_0$ (in between red and orange lines) and the intrinsic error of the model is minimum when $\theta_0 = \theta_\mathrm{c}$, i.e., when the centres of the two distributions coincide. Notice that when the centroids of the two distributions do not coincide the ROTADE measurement will, in general, depend on the separation of the two-source hypothesis.

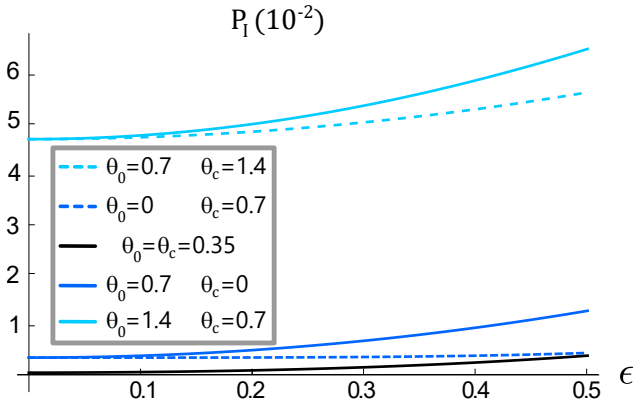

Figure B.6: *Intrinsic error of the qubit model ($\mathrm{P_I}$) in function of the separation ϵ, for different values of the misalignment for the case where the center of one source is not equal with the two-source centroid ($\theta_\mathrm{c} \neq \theta_0$).*

Acknowledgements

Like most things in life, a PhD thesis is not something you do alone. During the last years, every person around me had an influence, and I am grateful for all the interactions as they somehow contributed to this book. The scientific community around me was fundamental in reflecting and understanding my investigation, whereas the moments for coffee or rest consciously or unconsciously contributed to my personal and intellectual growth. As I cannot name everyone I would like to thank, I will name a few people without whom this thesis could not possibly have been done.

Firstly I want to thank my supervisor Maciek, for the full support in my decisions, always showing trust in my capacities. The balance between support and freedom is a special quality in the scientific community. In the same line, I would like to thank my co-supervisor Michalis, for the patience and dedication at all times. I would also like to thank James and Janek for their mentoring during their time as my advisers.

During these years my family and friends were a constant motivation. I am grateful to my parents, brother, sisters and nephews for the love and support during all times and for the scientific inspiration of my uncle LHA. I will always remember the 4' coffees at ICFO with Samyo, Hara, Patrick, Vindhyia, Sascha and Nazie. Also the exciting discussions with Valentin, Gabriel and Dani. I would not have done this without Gorka, and the emotional support Luis Lemus. I will always remember the music sessions and poetry sharing with my friends from UAB, Matias and Maria and the epic adventures with Joeri, Jonathan and Toni. I am grateful to my housemates and Guille for the patience and affection during the thesis writing. To my friends from Brasil, thank you for the motivation, Jaque, Lara, Bela, Gabriel, Dani and Malena.

I am grateful to ICFO administration and academic affairs for a smooth experience with administrative affairs.

Finally, I acknowledge the all the funding bodies that supported financially during my graduate research (details in publications [34, 50]).

Bibliography

[1] J. Q. Quach, "Which-way double-slit experiments and born-rule violation," *Phys. Rev. A*, vol. 95, p. 042129, Apr 2017. — p.10, 35, 37, 47.

[2] M. Tsang, R. Nair, and X.-M. Lu, "Quantum theory of superresolution for two incoherent optical point sources," *Phys. Rev. X*, vol. 6, p. 031033, Aug 2016. — p.11, 13, 57, 58, 59, 68, 69, 71.

[3] J. Wang, V. B. Scholz, and R. Renner, "Confidence polytopes in quantum state tomography," *Phys. Rev. Lett.*, vol. 122, p. 190401, May 2019. — p.12, 14, 82, 84, 85.

[4] L. R. F.R.S., "Xxxi. investigations in optics, with special reference to the spectroscope," *The London, Edinburgh, and Dublin Philosophical Magazine and Journal of Science*, vol. 8, no. 49, pp. 261–274, 1879. — p.13, 18, 56, 59.

[5] M. Planck, "Ueber das gesetz der energieverteilung im normalspectrum," *Annalen der Physik*, vol. 309, no. 3, pp. 553–563, 1901. — p.13.

[6] C. Cohen-Tannoudji, B. Diu, and F. Laloe, *Quantum Mechanics*. Wiley-VCH, 1977. — p.13, 22, 36.

[7] P. A. M. P. A. M. Dirac, *The collected works of P.A.M. Dirac, 1924-1948*. Cambridge ;: Cambridge University Press, 1995. — p.13.

[8] R. P. Feynman, R. B. Leighton, and M. Sands, *The Feynman Lectures on Physics, Quantum Behavior*. California Institute of Technology, 1963 and 2006 and 2010. — p.13, 36.

[9] C. Helstrom, "Resolution of point sources of light as analyzed by quantum detection theory," *IEEE Transactions on Information Theory*, vol. 19, no. 4, pp. 389–398, 1973. — p.13, 56, 57.

[10] V. P. Belavkin, "Generalized uncertainty relations and efficient measurements in quantum systems," *Theoretical and Mathematical Physics*, vol. 26, no. 3, pp. 213–222, 1976. — p.13.

[11] H. Yuen and M. Lax, "Multiple parameter quantum estimation and measurement of nonselfadjoint observables," *IRE Professional Group on Information Theory*, vol. 19, pp. 740–750, 1973. — p.13.

[12] M. A. Nielsen and I. L. Chuang, *Quantum Computation and Quantum Information: 10th Anniversary Edition*. Cambridge University Press, 2010. — p.13.

[13] S. M. Kay, *Fundamentals of Statistical Signal Processing Estimation Theory*. PRENTICE HALL, PROCESSING SERIES, 1998. — p.13, 25.

[14] R. Nair and M. Tsang, "Interferometric superlocalization of two incoherent optical point sources," *Opt. Express*, vol. 24, pp. 3684–3701, Feb 2016. — p.14, 71.

[15] C. Lupo and S. Pirandola, "Ultimate precision bound of quantum and subwavelength imaging," *Phys. Rev. Lett.*, vol. 117, p. 190802, Nov 2016. — p.14, 71.

[16] M. Tsang, "Subdiffraction incoherent optical imaging via spatial-mode demultiplexing," *New Journal of Physics*, vol. 19, no. 2, p. 023054, 2017. — p.14, 71.

[17] J. Řehaček, Z. Hradil, B. Stoklasa, M. Paúr, J. Grover, A. Krzic, and L. L. Sánchez-Soto, "Multiparameter quantum metrology of incoherent point sources: towards realistic superresolution," *Phys. Rev. A*, vol. 96, no. 6, p. 062107, 2017. — p.14, 71.

[18] J. Řeháček, Z. Hradil, D. Koutnỳ, J. Grover, A. Krzic, and L. L. Sánchez-Soto, "Optimal measurements for quantum spatial superresolution," *Phys. Rev. A*, vol. 98, no. 1, p. 012103, 2018. — p.14, 71.

[19] X.-M. Lu, H. Krovi, R. Nair, S. Guha, and J. H. Shapiro, "Quantum-optimal detection of one-versus-two incoherent optical sources with arbitrary separation," *npj Quantum Information*, vol. 4, no. 1, p. 64, 2018. — p.14, 58, 60, 63, 71.

[20] C. Napoli, S. Piano, R. Leach, G. Adesso, and T. Tufarelli, "Towards superresolution surface metrology: Quantum estimation of angular and axial separations," *Physical Review Letters*, vol. 122, may 2019. — p.14, 71.

[21] S. Prasad and Z. Yu, "Quantum-limited superlocalization and superresolution of a source pair in three dimensions," *Phys. Rev. A*, vol. 99, p. 022116, Feb 2019. — p.14, 71.

[22] M. Tsang, "Resolving starlight: a quantum perspective," *Contemporary Physics*, vol. 60, no. 4, pp. 279–298, 2019. — p.14, 59, 71.

[23] C. Lupo, Z. Huang, and P. Kok, "Quantum limits to incoherent imaging are achieved by linear interferometry," *Phys. Rev. Lett.*, vol. 124, p. 080503, Feb 2020. — p.14, 71.

[24] C. Datta, M. Jarzyna, Y. L. Len, K. Łukanowski, J. Kołodyński, and K. Banaszek, "Sub-rayleigh resolution of two incoherent sources by array homodyning," *Phys. Rev. A*, vol. 102, p. 063526, Dec 2020. — p.14, 71.

[25] Y. L. Len, "Multiparameter estimation for qubit states with collective measurements: a case study," *New Journal of Physics*, vol. 24, p. 033037, mar 2022. — p.14, 71.

[26] F. Yang, A. Tashchilina, E. S. Moiseev, C. Simon, and A. I. Lvovsky, "Far-field linear optical superresolution via heterodyne detection in a higher-order local oscillator mode," *Optica*, vol. 3, no. 10, pp. 1148–1152, 2016. — p.14, 71.

[27] M. Paúr, B. Stoklasa, Z. Hradil, L. L. Sánchez-Soto, and J. Rehacek, "Achieving the ultimate optical resolution," *Optica*, vol. 3, pp. 1144–1147,

Oct 2016. — p.14, 71.

[28] W.-K. Tham, H. Ferretti, and A. M. Steinberg, "Beating rayleigh's curse by imaging using phase information," *Physical review letters*, vol. 118, no. 7, p. 070801, 2017. — p.14, 71.

[29] J. Hassett, T. Malhorta, M. Alonso, R. Boyd, S. H. Rafsanjani, and A. Vamivakas, "Sub-rayleigh limit localization with a spatial mode analyzer," in *Frontiers in Optics*, pp. JW4A–124, Optical Society of America, 2018. — p.14, 71.

[30] M. Parniak, S. Borówka, K. Boroszko, W. Wasilewski, K. Banaszek, and R. Demkowicz-Dobrzański, "Beating the rayleigh limit using two-photon interference," *Phys. Rev. Lett.*, vol. 121, p. 250503, Dec 2018. — p.14, 57, 71, 72, 74, 78.

[31] Y. Zhou, J. Yang, J. D. Hassett, S. M. H. Rafsanjani, M. Mirhosseini, A. N. Vamivakas, A. N. Jordan, Z. Shi, and R. W. Boyd, "Quantum-limited estimation of the axial separation of two incoherent point sources," *Optica*, vol. 6, no. 5, pp. 534–541, 2019. — p.14, 71.

[32] B. Brecht, V. Ansari, J. Gil-Lopez, J. Donohue, J. Řeháček, Z. Hradil, L. Sánchez-Soto, and C. Silberhorn, "Experimental demonstration of multiparameter estimation at the ultimate quantum limit," in *Quantum 2.0*, pp. QW6A–17, Optical Society of America, 2020. — p.14, 71.

[33] A. Z. Goldberg, L. L. Sánchez-Soto, and H. Ferretti, "Intrinsic sensitivity limits for multiparameter quantum metrology," *Phys. Rev. Lett.*, vol. 127, p. 110501, Sep 2021. — p.14, 71.

[34] J. O. de Almeida, J. Kołodyński, C. Hirche, M. Lewenstein, and M. Skotiniotis, "Discrimination and estimation of incoherent sources under misalignment," *Phys. Rev. A*, vol. 103, p. 022406, Feb 2021. — p.14, 15, 71.

[35] H. Häffner, W. Hänsel, C. F. Roos, J. Benhelm, D. Chek-al kar, M. Chwalla, T. Körber, U. D. Rapol, M. Riebe, P. O. Schmidt, C. Becher, O. Gühne, W. Dür, and R. Blatt, "Scalable multiparticle entanglement of trapped ions," *Nature*, vol. 438, no. 7068, pp. 643–646, 2005. — p.14, 82.

[36] W.-B. Gao, C.-Y. Lu, X.-C. Yao, P. Xu, O. Gühne, A. Goebel, Y.-A. Chen, C.-Z. Peng, Z.-B. Chen, and J.-W. Pan, "Experimental demonstration of a hyper-entangled ten-qubit schrödinger cat state," *Nature Physics*, vol. 6, no. 5, pp. 331–335, 2010. — p.14, 82.

[37] T. Monz, P. Schindler, J. T. Barreiro, M. Chwalla, D. Nigg, W. A. Coish, M. Harlander, W. Hänsel, M. Hennrich, and R. Blatt, "14-qubit entanglement: Creation and coherence," *Phys. Rev. Lett.*, vol. 106, p. 130506, Mar 2011. — p.14, 82.

[38] C. Schwemmer, G. Tóth, A. Niggebaum, T. Moroder, D. Gross, O. Gühne,

and H. Weinfurter, "Experimental comparison of efficient tomography schemes for a six-qubit state," *Phys. Rev. Lett.*, vol. 113, p. 040503, Jul 2014. — p.14, 82.

[39] Y. S. Teo, B.-G. Englert, J. Řeháček, Z. Hradil, and D. Mogilevtsev, "Verification of state and entanglement with incomplete tomography," *New Journal of Physics*, vol. 14, p. 105020, oct 2012. — p.14, 82.

[40] M. Guţă, J. Kahn, R. Kueng, and J. A. Tropp, "Fast state tomography with optimal error bounds," *Journal of Physics A: Mathematical and Theoretical*, vol. 53, p. 204001, apr 2020. — p.14, 82, 85, 86.

[41] A. Acharya, T. Kypraios, and M. Guţă, "A comparative study of estimation methods in quantum tomography," *Journal of Physics A: Mathematical and Theoretical*, vol. 52, p. 234001, may 2019. — p.14, 82.

[42] N. Yu, "Sample efficient tomography via pauli measurements," 2020. — p.14, 82.

[43] R. Blume-Kohout, "Robust error bars for quantum tomography," 2012. — p.14, 82.

[44] J. Shang, H. K. Ng, A. Sehrawat, X. Li, and B.-G. Englert, "Optimal error regions for quantum state estimation," *New Journal of Physics*, vol. 15, p. 123026, dec 2013. — p.14, 82.

[45] T. Young, "I. the bakerian lecture. experiments and calculations relative to physical optics," *Philosophical transactions of the Royal Society of London*, no. 94, pp. 1–16, 1804. — p.14.

[46] H. Yabuki, "Feynman path integrals in the young double-slit experiment," *International Journal of Theoretical Physics*, vol. 25, pp. 159–174, Feb 1986. — p.14, 18, 21, 36, 38, 39.

[47] U. Sinha, C. Couteau, T. Jennewein, R. Laflamme, and G. Weihs, "Ruling out multi-order interference in quantum mechanics," *Science*, vol. 329, no. 5990, pp. 418–421, 2010. — p.14, 37, 51.

[48] T. Kauten, R. Keil, T. Kaufmann, B. Pressl, Č. Brukner, and G. Weihs, "Obtaining tight bounds on higher-order interferences with a 5-path interferometer," *New Journal of Physics*, vol. 19, p. 033017, mar 2017. — p.14.

[49] P. Namdar, P. K. Jenke, I. A. Calafell, A. Trenti, M. Radonjić, B. Dakić, P. Walther, and L. A. Rozema, "Experimental higher-order interference in a nonlinear triple slit," 2021. — p.14.

[50] J. O. de Almeida, M. Lewenstein, and J. Q. Quach, "Significant nonclassical paths with atoms and cavities in the double-slit experiment," *Phys. Rev. A*, vol. 102, p. 042225, Oct 2020. — p.14, 15, 37.

[51] J. O. de Almeida, M. Lewenstein, and M. Skotiniotis, "Collective superresolving measurements for mixed bosonic states," 2021. — p.15, 80.

[52] G. R. Fowles, *Introduction to modern optics*. Courier Corporation, 1989.

— p.17, 18.

[53] R. P. Feynman and A. R. Hibbs, *Quantum Mechanics and Path Integrals, 3rd ed.* McGraw-Hill, 1965. — p.18, 36.

[54] A. H. R.P. Feynman, *Quantum Mechanics and Path Integrals.* 3rd ed., McGraw-Hill, New York, 1965. — p.21.

[55] C. J. Davisson and L. H. Germer, "Reflection of electrons by a crystal of nickel," *Proceedings of the National Academy of Sciences*, vol. 14, no. 4, pp. 317–322, 1928. — p.21.

[56] C. Jönsson, "Elektroneninterferenzen an mehreren künstlich hergestellten feinspalten," *Zeitschrift für Physik*, vol. 161, no. 4, pp. 454 – 474, 1961. — p.21, 36.

[57] A. Zeilinger, "Experiment and the foundations of quantum physics," *Rev. Mod. Phys.*, vol. 71, pp. S288–S297, Mar 1999. — p.21, 36.

[58] S. Eibenberger, S. Gerlich, M. Arndt, M. Mayor, and J. Tüxen, "Matter–wave interference of particles selected from a molecular library with masses exceeding 10000 amu," *Phys. Chem. Chem. Phys.*, vol. 15, pp. 14696–14700, 2013. — p.21.

[59] De Broglie, Louis, "Recherches sur la théorie des quanta," *Ann. Phys.*, vol. 10, no. 3, pp. 22–128, 1925. — p.21.

[60] Z. Hradil, "Quantum-state estimation," *Phys. Rev. A*, vol. 55, pp. R1561–R1564, Mar 1997. — p.24, 82.

[61] T. Sugiyama, P. S. Turner, and M. Murao, "Error probability analysis in quantum tomography: A tool for evaluating experiments," *Phys. Rev. A*, vol. 83, p. 012105, Jan 2011. — p.24.

[62] U. Leonhardt, H. Paul, and G. M. D'Ariano, "Tomographic reconstruction of the density matrix via pattern functions," *Phys. Rev. A*, vol. 52, pp. 4899–4907, Dec 1995. — p.24.

[63] M. Christandl and R. Renner, "Reliable quantum state tomography," *Phys. Rev. Lett.*, vol. 109, p. 120403, Sep 2012. — p.24.

[64] E. Lehmann and G. Casella, *Theory of Point Estimation.* Springer, 1998. — p.26.

[65] E. Pitman, *Some Basic Theory for Statistical Inference.* CRC Press, 1979. — p.26.

[66] R. A. Fisher and E. J. Russell, "On the mathematical foundations of theoretical statistics," *Philosophical Transactions of the Royal Society of London. Series A, Containing Papers of a Mathematical or Physical Character*, vol. 222, no. 594-604, pp. 309–368, 1922. — p.27.

[67] H. Cramér, *Mathematical Methods of Statistics (PMS-9).* Princeton University Press, 2016. — p.28.

[68] C. R. Rao, *Information and the Accuracy Attainable in the Estimation of*

Statistical Parameters. New York, NY: Springer New York, 1992. — p.28.

[69] S. L. Braunstein and C. M. Caves, "Statistical distance and the geometry of quantum states," *Phys. Rev. Lett.*, vol. 72, pp. 3439–3443, May 1994. — p.28, 29, 57, 59.

[70] O. E. Barndorff-Nielsen and R. D. Gill, "Fisher information in quantum statistics," *Journal of Physics A: Mathematical and General*, vol. 33, pp. 4481–4490, jun 2000. — p.29.

[71] M. G. A. Paris, "Quantum estimation for quantum technology," *International Journal of Quantum Information*, vol. 07, no. supp01, pp. 125–137, 2009. — p.29.

[72] S. Ragy, M. Jarzyna, and R. Demkowicz-Dobrzański, "Compatibility in multiparameter quantum metrology," *Phys. Rev. A*, vol. 94, p. 052108, Nov 2016. — p.30, 57, 59.

[73] E. L. Lehmann, *Testing statistical hypotheses*. New York, Wiley, 1959. — p.30.

[74] D. Middleton, *An Introduction to Statistical Communication Theory*. McGraw-Hill, 1960. — p.30.

[75] C. W. Helstrom, *Statistical theory of signal detection*. Pergamon Oxford, 1968. — p.30.

[76] V. Trees, *Detection, Estimation, and modulation theory*. Wiley, New York, 1968. — p.30.

[77] C. W. Helstrom, *Quantum Detection and Estimation Theory*. Academic Press, 1976. — p.30, 31, 32, 57.

[78] T. M. Cover and J. A. Thomas, *Elements of Information Theory (Wiley Series in Telecommunications and Signal Processing)*. USA: Wiley-Interscience, 2006. — p.30.

[79] A. S. Holevo, "On asymptotically optimal hypotheses testing in quantum statistics," *Teoriya Veroyatnostei i ee Primeneniya*, vol. 23, no. 2, pp. 429–432, 1978. — p.31.

[80] H. Chernoff, "A Measure of Asymptotic Efficiency for Tests of a Hypothesis Based on the sum of Observations," *The Annals of Mathematical Statistics*, vol. 23, no. 4, pp. 493 – 507, 1952. — p.31, 85.

[81] M. Nussbaum and A. Szkoła, "The chernoff lower bound for symmetric quantum hypothesis testing," *The Annals of Statistics*, vol. 37, no. 2, pp. 1040–1057, 2009. — p.33.

[82] R. Shankar, "Simple problems in one dimension," in *Principles of Quantum Mechanics*, pp. 175–178, Springer, 1994. — p.36.

[83] A. Zeilinger, R. Gähler, C. G. Shull, W. Treimer, and W. Mampe, "Single- and double-slit diffraction of neutrons," *Rev. Mod. Phys.*, vol. 60, pp. 1067–1073, Oct 1988. — p.36.

[84] D. M. Greenberger and A. Yasin, "Simultaneous wave and particle knowledge in a neutron interferometer," *Physics Letters A*, vol. 128, no. 8, pp. 391–394, 1988. — p.36.

[85] G. Rengaraj, U. Prathwiraj, S. N. Sahoo, R. Somashekhar, and U. Sinha, "Measuring the deviation from the superposition principle in interference experiments," *New Journal of Physics*, vol. 20, no. 6, p. 063049, 2018. — p.36, 51.

[86] A. Taflove and S. Hagness, *Computational Electrodynamics: The Finite-Difference Time-Domain Method*. Artech House, Boston, 2005. — p.36.

[87] H. De Raedt, K. Michielsen, and K. Hess, "Analysis of multipath interference in three-slit experiments," *Phys. Rev. A*, vol. 85, p. 012101, Jan 2012. — p.36, 51.

[88] A. Sinha, A. H. Vijay, and U. Sinha, "On the superposition principle in interference experiments," *Scientific Reports*, vol. 5, p. 10304, Oct 2015. — p.36, 51.

[89] W. K. Wootters and W. H. Zurek, "Complementarity in the double-slit experiment: Quantum nonseparability and a quantitative statement of bohr's principle," *Phys. Rev. D*, vol. 19, pp. 473–484, Jan 1979. — p.36.

[90] M. O. Scully, B.-G. Englert, and H. Walther, "Quantum optical tests of complementarity," *Nature*, vol. 351, pp. 111–116, 1991. — p.36.

[91] M. O. Scully and K. Drühl, "Quantum eraser: A proposed photon correlation experiment concerning observation and "delayed choice" in quantum mechanics," *Phys. Rev. A*, vol. 25, pp. 2208–2213, Apr 1982. — p.37.

[92] J. Wheeler, *Quantum Theory and Measurement*. Princeton University Press, 1983. — p.37.

[93] T. J. Herzog, P. G. Kwiat, H. Weinfurter, and A. Zeilinger, "Complementarity and the quantum eraser," *Phys. Rev. Lett.*, vol. 75, pp. 3034–3037, Oct 1995. — p.37.

[94] Y.-H. Kim, R. Yu, S. P. Kulik, Y. Shih, and M. O. Scully, "Delayed "choice" quantum eraser," *Phys. Rev. Lett.*, vol. 84, pp. 1–5, Jan 2000. — p.37.

[95] V. Jacques, E. Wu, F. Grosshans, F. Treussart, P. Grangier, A. Aspect, and J.-F. Roch, "Experimental realization of wheeler's delayed-choice gedanken experiment," *Science*, vol. 315, no. 5814, pp. 966–968, 2007. — p.37.

[96] S. P. Walborn, M. O. T. Cunha, S. Pádua, and C. H. Monken, "Double-slit quantum eraser," *Phys. Rev. A*, vol. 65, p. 033818, Feb 2002. — p.37.

[97] J. de Oliveira, G. de Souza, L. Cabral, I. da Paz, and M. Sampaio, "Exotic looped trajectories via quantum marking," *Annals of Physics*, vol. 387, pp. 222 – 238, 2017. — p.37, 39.

[98] M. Born, "Zur quantenmechanik der stoßvorgänge," *Zeitschrift für Physik*, vol. 37, no. 12, pp. 863–867, 1926. — p.37.

[99] R. D. Sorkin, "Quantum mechanics as a quantum measure theory," *Mod. Phys. Lett.*, vol. A9, pp. 3119–3128, 1994. — p.37, 51.

[100] O. S. Magaña Loaiza, I. De Leon, M. Mirhosseini, R. Fickler, A. Safari, U. Mick, B. McIntyre, P. Banzer, B. Rodenburg, G. Leuchs, and R. W. Boyd, "Exotic looped trajectories of photons in three-slit interference," *Nature Communications*, vol. 7, p. 13987, 2016. — p.37.

[101] R. Sawant, J. Samuel, A. Sinha, S. Sinha, and U. Sinha, "Nonclassical paths in quantum interference experiments," *Phys. Rev. Lett.*, vol. 113, p. 120406, Sep 2014. — p.37, 38, 40, 51, 52.

[102] J. W. Goodman, *Introduction to Fourier Optics*. THE McGRAW-HILL COMPANIES, INC., 1996,1968. — p.38.

[103] I. G. da Paz, C. H. S. Vieira, R. Ducharme, L. A. Cabral, H. Alexander, and M. D. R. Sampaio, "Gouy phase in nonclassical paths in a triple-slit interference experiment," *Phys. Rev. A*, vol. 93, p. 033621, Mar 2016. — p.39.

[104] C. H. S. Vieira, H. A. S. Costa, G. de Souza, M. Sampaio, and I. G. da Paz, "Fringe visibility of exotic trajectories for matter waves in a double-slit experiment," *Modern Physics Letters A*, vol. 34, no. 28, p. 1950233, 2019. — p.39.

[105] J. Krause, M. O. Scully, and H. Walther, "State reduction and —n¿ - state preparation in a high - q micromaser," *Phys. Rev. A*, vol. 36, pp. 4547–4550, Nov 1987. — p.41.

[106] M. Srinivas and E. Davies, "Photon counting probabilities in quantum optics," *Optica Acta: International Journal of Optics*, vol. 28, no. 7, pp. 981–996, 1981. — p.45.

[107] P. Zoller, M. Marte, and D. F. Walls, "Quantum jumps in atomic systems," *Phys. Rev. A*, vol. 35, pp. 198–207, Jan 1987. — p.45.

[108] M.-O. Pleinert, A. Rueda, E. Lutz, and J. von Zanthier, "Testing higher-order quantum interference with many-particle states," *Phys. Rev. Lett.*, vol. 126, p. 190401, May 2021. — p.51.

[109] B.-S. K. Skagerstam, "On the three-slit experiment and quantum mechanics," *Journal of Physics Communications*, vol. 2, p. 125014, dec 2018. — p.51.

[110] R. P. Feynman, R. B. Leighton, and M. Sands, *The Feynman Lectures on Physics, Diffraction*. California Institute of Technology, 1963 and 2006 and 2010. — p.56.

[111] A. J. den Dekker and A. van den Bos, "Resolution: a survey," *J. Opt. Soc. Am. A*, vol. 14, pp. 547–557, Mar 1997. — p.56.

[112] C. W. Helstrom, "Resolvability of objects from the standpoint of statistical parameter estimation∗," *J. Opt. Soc. Am.*, vol. 60, pp. 659–666, May 1970.

— p.56.

[113] C. W. Helstrom, "Detection and resolution of incoherent objects by a background-limited optical system∗," *J. Opt. Soc. Am.*, vol. 59, pp. 164–175, Feb 1969. — p.56.

[114] C. W. Helstrom, "Quantum detection and estimation theory," *Journal of Statistical Physics*, vol. 1, no. 2, pp. 231–252, 1969. — p.56.

[115] S. W. Hell and J. Wichmann, "Breaking the diffraction resolution limit by stimulated emission: stimulated-emission-depletion fluorescence microscopy," *Opt. Lett.*, vol. 19, pp. 780–782, Jun 1994. — p.56.

[116] E. Betzig, G. H. Patterson, R. Sougrat, O. W. Lindwasser, S. Olenych, J. S. Bonifacino, M. W. Davidson, J. Lippincott-Schwartz, and H. F. Hess, "Imaging intracellular fluorescent proteins at nanometer resolution," *Science*, vol. 313, no. 5793, pp. 1642–1645, 2006. — p.57.

[117] S. W. Hell, "Far-field optical nanoscopy," *Science*, vol. 316, no. 5828, pp. 1153–1158, 2007. — p.57.

[118] W. E. Moerner, "New directions in single-molecule imaging and analysis," *Proceedings of the National Academy of Sciences*, vol. 104, no. 31, pp. 12596–12602, 2007. — p.57.

[119] C. K. Hong, Z. Y. Ou, and L. Mandel, "Measurement of subpicosecond time intervals between two photons by interference," *Phys. Rev. Lett.*, vol. 59, pp. 2044–2046, Nov 1987. — p.57, 72.

[120] J. C. Garcia-Escartin and P. Chamorro-Posada, "swap test and hong-ou-mandel effect are equivalent," *Phys. Rev. A*, vol. 87, p. 052330, May 2013. — p.57, 72.

[121] C. Bădescu, R. O'Donnell, and J. Wright, "Quantum state certification," in *Proceedings of the 51st Annual ACM SIGACT Symposium on Theory of Computing*, pp. 503–514, 2019. — p.57, 74, 77.

[122] M. Fanizza, M. Rosati, M. Skotiniotis, J. Calsamiglia, and V. Giovannetti, "Beyond the swap test: Optimal estimation of quantum state overlap," *Phys. Rev. Lett.*, vol. 124, p. 060503, Feb 2020. — p.57, 74, 77.

[123] A. I. Lvovsky, B. C. Sanders, and W. Tittel, "Optical quantum memory," *Nature Photonics*, vol. 3, pp. 706–714, dec 2009. — p.57.

[124] M. Kroutvar, Y. Ducommun, D. Heiss, M. Bichler, D. Schuh, G. Abstreiter, and J. J. Finley, "Optically programmable electron spin memory using semiconductor quantum dots," *Nature*, vol. 432, pp. 81–84, nov 2004. — p.57, 79.

[125] B. Julsgaard, J. Sherson, J. I. Cirac, J. Fiurášek, and E. S. Polzik, "Experimental demonstration of quantum memory for light," *Nature*, vol. 432, pp. 482–486, nov 2004. — p.57, 79.

[126] M. Fleischhauer and M. D. Lukin, "Quantum memory for photons: Dark-

state polaritons," *Phys. Rev. A*, vol. 65, p. 022314, Jan 2002. — p.57, 79.

[127] T. Chanelière, D. Matsukevich, S. Jenkins, S.-Y. Lan, T. Kennedy, and A. Kuzmich, "Storage and retrieval of single photons transmitted between remote quantum memories," *Nature*, vol. 438, no. 7069, pp. 833–836, 2005. — p.57, 79.

[128] H. Krovi, S. Guha, and J. H. Shapiro, "Attaining the quantum limit of passive imaging," *arXiv preprint arXiv:1609.00684*, 2016. — p.57.

[129] A. Labeyrie, S. G. Lipson, and P. Nisenson, *An Introduction to Optical Stellar Interferometry*. Cambridge University Press, 2006. — p.58.

[130] M. Tsang, "Quantum nonlocality in weak-thermal-light interferometry," *Phys. Rev. Lett.*, vol. 107, p. 270402, Dec 2011. — p.58.

[131] H. Yuen and J. H. Shapiro, "Optical communication with two-photon coherent states–part i: Quantum-state propagation and quantum-noise," *IEEE Trans. Inf. Theory*, vol. 24, no. 6, pp. 657–668, 1978. — p.59.

[132] L. Rayleigh, "Xvii. on the resolving-power of telescopes," *Lond.Edinb.Dubl.Phil.Mag.*, vol. 10, no. 60, pp. 116–119, 1880. — p.59.

[133] M. R. Grace, Z. Dutton, A. Ashok, and S. Guha, "Approaching quantum-limited imaging resolution without prior knowledge of the object location," *J. Opt. Soc. Am. A*, vol. 37, pp. 1288–1299, Aug 2020. — p.60.

[134] A. Chrostowski, R. Demkowicz-Dobrzański, M. Jarzyna, and K. Banaszek, "On super-resolution imaging as a multiparameter estimation problem," *Int. J. Quantum Inf.*, vol. 15, no. 08, p. 1740005, 2017. — p.61, 62.

[135] M. Gessner, C. Fabre, and N. Treps, "Superresolution limits from measurement crosstalk," *Phys. Rev. Lett.*, vol. 125, p. 100501, Aug 2020. — p.70, 71.

[136] R. B. A. Adamson, P. S. Turner, M. W. Mitchell, and A. M. Steinberg, "Detecting hidden differences via permutation symmetries," *Phys. Rev. A*, vol. 78, p. 033832, Sep 2008. — p.71.

[137] R. B. A. Adamson, L. K. Shalm, M. W. Mitchell, and A. M. Steinberg, "Multiparticle state tomography: Hidden differences," *Phys. Rev. Lett.*, vol. 98, p. 043601, Jan 2007. — p.71.

[138] M. Keyl and R. F. Werner, "Estimating the spectrum of a density operator," *Phys. Rev. A*, vol. 64, p. 052311, Oct 2001. — p.72, 77.

[139] H. Buhrman, R. Cleve, J. Watrous, and R. de Wolf, "Quantum fingerprinting," *Phys. Rev. Lett.*, vol. 87, p. 167902, Sep 2001. — p.74.

[140] A. K. Ekert, C. M. Alves, D. K. L. Oi, M. Horodecki, P. Horodecki, and L. C. Kwek, "Direct estimations of linear and nonlinear functionals of a quantum state," *Phys. Rev. Lett.*, vol. 88, p. 217901, May 2002. — p.74.

[141] E. Sjöqvist, A. K. Pati, A. Ekert, J. S. Anandan, M. Ericsson, D. K. L. Oi, and V. Vedral, "Geometric phases for mixed states in interferometry," *Phys. Rev. Lett.*, vol. 85, pp. 2845–2849, Oct 2000. — p.74.

[142] H. Weyl, *The classical groups: Their invariants and representations*. Mathematics, Princeton Univ Pr, 2nd ed., 1946. — p.74, 75.

[143] H. G. Dales, P. Aeina, J. Eschmeier, K. Laursen, and G. A. Willis, *Introduction to Banach Algebras, Operators and Harmonic Analysis*. Cambridge University Press, 2003. — p.74.

[144] R. A. Horn and C. R. Johnson, *Matrix analysis*. Cambridge, New York: Cambridge University Press, 2nd ed ed., 2012. — p.75.

[145] A. M. Childs, A. W. Harrow, and P. Wocjan, "Weak fourier-schur sampling, the hidden subgroup problem, and the quantum collision problem," in *Annual Symposium on Theoretical Aspects of Computer Science*, pp. 598–609, Springer, 2007. — p.77.

[146] R. O'Donnell and J. Wright, "Quantum spectrum testing," in *Proceedings of the forty-seventh annual ACM symposium on Theory of computing*, pp. 529–538, 2015. — p.77.

[147] R. Alicki, S. Rudnicki, and S. Sadowski, "Symmetry properties of product states for the system of N n -level atoms," *Journal of Mathematical Physics*, vol. 29, pp. 1158–1162, May 1988. — p.77.

[148] B. Gendra, E. Ronco-Bonvehi, J. Calsamiglia, R. Muñoz-Tapia, and E. Bagan, "Beating noise with abstention in state estimation," *New Journal of Physics*, vol. 14, p. 105015, oct 2012. — p.78.

[149] K. Heshami, D. G. England, P. C. Humphreys, P. J. Bustard, V. M. Acosta, J. Nunn, and B. J. Sussman, "Quantum memories: emerging applications and recent advances," *Journal of Modern Optics*, vol. 63, no. 20, pp. 2005–2028, 2016. PMID: 27695198. — p.79.

[150] L. Gan, R. Wang, D. Liu, L. Duan, S. Liu, S. Fu, B. Li, Z. Feng, H. Wei, W. Tong, *et al.*, "Spatial-division multiplexed mach–zehnder interferometers in heterogeneous multicore fiber for multiparameter measurement," *IEEE Photonics Journal*, vol. 8, no. 1, pp. 1–8, 2016. — p.79, 80.

[151] J. Cariñe, G. Cañas, P. Skrzypczyk, I. Šupić, N. Guerrero, T. Garcia, L. Pereira, M. A. S. Prosser, G. B. Xavier, A. Delgado, S. P. Walborn, D. Cavalcanti, and G. Lima, "Multi-core fiber integrated multi-port beam splitters for quantum information processing," *Optica*, vol. 7, pp. 542–550, May 2020. — p.79, 80.

[152] C. Simon, H. de Riedmatten, M. Afzelius, N. Sangouard, H. Zbinden, and N. Gisin, "Quantum repeaters with photon pair sources and multimode memories," *Phys. Rev. Lett.*, vol. 98, p. 190503, May 2007. — p.79.

[153] N. Sangouard, C. Simon, H. de Riedmatten, and N. Gisin, "Quantum re-

peaters based on atomic ensembles and linear optics," *Rev. Mod. Phys.*, vol. 83, pp. 33–80, Mar 2011. — p.79.

[154] N. Sinclair, E. Saglamyurek, H. Mallahzadeh, J. A. Slater, M. George, R. Ricken, M. P. Hedges, D. Oblak, C. Simon, W. Sohler, and W. Tittel, "Spectral multiplexing for scalable quantum photonics using an atomic frequency comb quantum memory and feed-forward control," *Phys. Rev. Lett.*, vol. 113, p. 053603, Jul 2014. — p.79.

[155] T.-S. Yang, Z.-Q. Zhou, Y.-L. Hua, X. Liu, Z.-F. Li, P.-Y. Li, Y. Ma, C. Liu, P.-J. Liang, X. Li, *et al.*, "Multiplexed storage and real-time manipulation based on a multiple degree-of-freedom quantum memory," *Nature communications*, vol. 9, no. 1, pp. 1–8, 2018. — p.79.

[156] D. Lago-Rivera, S. Grandi, J. V. Rakonjac, A. Seri, and H. de Riedmatten, "Telecom-heralded entanglement between multimode solid-state quantum memories," *Nature*, vol. 594, no. 7861, pp. 37–40, 2021. — p.79.

[157] J. Bland-Hawthorn, M. J. Sellars, and J. G. Bartholomew, "Quantum memories and the double-slit experiment: implications for astronomical interferometry," *J. Opt. Soc. Am. B*, vol. 38, pp. A86–A98, Jul 2021. — p.79.

[158] M. Mazelanik, A. Leszczyński, and M. Parniak, "Optical-domain spectral super-resolution via a quantum-memory-based time-frequency processor," *Nature Communications*, vol. 13, no. 1, p. 691, 2022. — p.79, 80.

[159] P. C. Maurer, G. Kucsko, C. Latta, L. Jiang, N. Y. Yao, S. D. Bennett, F. Pastawski, D. Hunger, N. Chisholm, M. Markham, *et al.*, "Room-temperature quantum bit memory exceeding one second," *Science*, vol. 336, no. 6086, pp. 1283–1286, 2012. — p.79.

[160] D. Kielpinski, V. Meyer, M. A. Rowe, C. A. Sackett, W. M. Itano, C. Monroe, and D. J. Wineland, "A decoherence-free quantum memory using trapped ions," *Science*, vol. 291, no. 5506, pp. 1013–1015, 2001. — p.79.

[161] M. J. Biercuk, H. Uys, A. P. VanDevender, N. Shiga, W. M. Itano, and J. J. Bollinger, "Optimized dynamical decoupling in a model quantum memory," *Nature*, vol. 458, no. 7241, pp. 996–1000, 2009. — p.79.

[162] K. Hammerer, A. S. Sørensen, and E. S. Polzik, "Quantum interface between light and atomic ensembles," *Rev. Mod. Phys.*, vol. 82, pp. 1041–1093, Apr 2010. — p.80.

[163] S. Mährlein, J. Von Zanthier, and G. S. Agarwal, "Complete three photon hong-ou-mandel interference at a three port device," *Optics express*, vol. 23, no. 12, pp. 15833–15847, 2015. — p.80.

[164] S. Stanisic and P. S. Turner, "Discriminating distinguishability," *Physical Review A*, vol. 98, no. 4, p. 043839, 2018. — p.80.

[165] J. Wu, H. de Guise, and B. C. Sanders, "Coincidence landscapes for polarized bosons," *Physical Review A*, vol. 98, no. 1, p. 013817, 2018. — p.80.

[166] H.-H. Lu, J. M. Lukens, N. A. Peters, O. D. Odele, D. E. Leaird, A. M. Weiner, and P. Lougovski, "Electro-optic frequency beam splitters and tritters for high-fidelity photonic quantum information processing," *Phys. Rev. Lett.*, vol. 120, p. 030502, Jan 2018. — p.80.

[167] N. Spagnolo, C. Vitelli, L. Aparo, P. Mataloni, F. Sciarrino, A. Crespi, R. Ramponi, and R. Osellame, "Three-photon bosonic coalescence in an integrated tritter," *Nature Communications*, vol. 4, no. 1, p. 1606, 2013. — p.80.

[168] V. Ansari, B. Brecht, J. Gil-Lopez, J. M. Donohue, J. Řeháček, Z. c. v. Hradil, L. L. Sánchez-Soto, and C. Silberhorn, "Achieving the ultimate quantum timing resolution," *PRX Quantum*, vol. 2, p. 010301, Jan 2021. — p.80.

[169] J. Řehaček, Z. Hradil, and M. Ježek, "Iterative algorithm for reconstruction of entangled states," *Phys. Rev. A*, vol. 63, p. 040303, Mar 2001. — p.82.

[170] R. Blume-Kohout, "Optimal, reliable estimation of quantum states," *New Journal of Physics*, vol. 12, p. 043034, apr 2010. — p.82.

[171] S. V. D. Geer, "A new approach to least-squares estimation, with applications," *The Annals of Statistics*, vol. 15, no. 2, pp. 587–602, 1987. — p.82.

[172] F. Qi, Z. Wang, W. Xu, X.-W. Chen, and Z.-Y. Li, "Towards simultaneous observation of path and interference of a single photon in a modified mach-zehnder interferometer," *Photon. Res.*, vol. 8, pp. 622–629, Apr 2020. — p.89.

[173] M. Davidović, A. S. Sanz, M. Božić, and D. Arsenović, "Coherence loss and revivals in atomic interferometry: a quantum-recoil analysis," *Journal of Physics A: Mathematical and Theoretical*, vol. 45, p. 165303, apr 2012. — p.89.

[174] Y. Ji, Y. Chung, D. Sprinzak, M. Heiblum, D. Mahalu, and H. Shtrikman, "An electronic mach–zehnder interferometer," *Nature*, vol. 422, no. 6930, pp. 415–418, 2003. — p.89.

[175] E. B. Davies, *Quantum Theory of Open Systems.* Academic Press, 1976. — p.93.

[176] K. Jacobs, *Stochastic Process for Physicists - Understanding noisy systems.* University Press, 2010. — p.93.

[177] H. M. Wiseman and G. J. Milburn, *Quantum Measurement and Control.* Cambridge University Press, 2009. — p.93.

[178] R. Kerviche, S. Guha, and A. Ashok, "Fundamental limit of resolving two point sources limited by an arbitrary point spread function," in *2017 IEEE International Symposium on Information Theory (ISIT)*, pp. 441–445, IEEE, 2017. — p.98.